8-6-2021

Degradation modeling and degradation-aware control of power electronic systems

Moinul Shahidul Haque
msh.msuec@msstate.edu

Degradation modeling and degradation-aware control of power electronic systems

By

Moinul Shahidul Haque

Approved by:

Seungdeog Choi (Major Professor)
Masoud Karimi-Ghartemani
Yong Fu
Chanyeop Park
Jenny Q. Du (Graduate Coordinator)
Jason M. Keith (Dean, Bagley College of Engineering)

A Dissertation
Submitted to the Faculty of
Mississippi State University
in Partial Fulfillment of the Requirements
for the Degree of Doctor of Philosophy
in Electrical and Computer Engineering
in the Department of Electrical and Computer Engineering

Mississippi State, Mississippi

August 2021

Name: Moinul Shahidul Haque

Date of Degree: August 6, 2021

Institution: Mississippi State University

Major Field: Electrical and Computer Engineering

Select Appropriate Title: Seungdeog Choi

Title of Study: Degradation modeling and degradation-aware control of power electronic systems

Pages in Study: 120

Candidate for Degree of Doctor of Philosophy

The power electronics market is valued at $23.25 billion in 2019 and is projected to reach $ 36.64 billion by 2027. Power electronic systems (PES) have been extensively used in a wide range of critical applications, including automotive, renewable energy, industrial variable-frequency drive, etc. Thus, the PESs' reliability and robustness are immensely important for the smooth operation of mission-critical applications. Power semiconductor switches are one of the most vulnerable components in the PES. The vulnerability of these switches impacts the reliability and robustness of the PES. Thus, switch-health monitoring and prognosis are critical for avoiding unexpected shutdowns and preventing catastrophic failures. The importance of the prognosis study increases dramatically with the growing popularity of the next-generation power semiconductor switches, wide bandgap switches. These switches show immense promise in the high-power high-frequency operations due to their higher breakdown voltage and lower switch loss. But their wide adaptation is limited by the inadequate reliability study. A thorough prognosis study comprising switch degradation modeling, remaining useful life (RUL) estimation, and degradation-aware controller development, is important to enhance the PESs' robustness, especially with wide bandgap switches. In this dissertation, three studies are conducted to achieve these objectives- 1)

Insulated Gate Bipolar Transistor (IGBT) degradation modeling and RUL estimation, 2) cascode Gallium Nitride (GaN) Field-Effect Transistor (FET) degradation modeling and RUL estimation, and 3) Degradation-aware controller design for a PES, solid-state transformer (SST). The first two studies have addressed the significant variation in RUL estimation and proposed degradation identification methods for IGBT and cascode GaN FET. In the third study, a system-level integration of the switch degradation model is implemented in the SST. The insight into the switch's degradation pattern from the first two studies is integrated into developing a degradation-aware controller for the SST. State-of-the-art controllers do not consider the switch degradation that results in premature system failure. The proposed low-complexity degradation-aware and adaptive SST controller ensures optimal degradation-aware power transfer and robust operation over the lifetime.

DEDICATION

To my family and extended family

ACKNOWLEDGEMENTS

I would like to extend appreciation and gratitude to those who supported me with technical knowledge, guidance, and motivation to accomplish my graduate study's goal.

First, I would like to thank my advisor, Dr. Seungdeog Choi, for his guidance and support during my graduate studies. His continuous inspiration and high work ethics motivate me to achieve my Ph.D. goal.

I would also like to thank my committee members Dr. Karimi, Dr. Fu, and Dr. Park, for their suggestions and motivation.

Special thanks to my colleagues from the Advanced Energy Conversion Lab (AECL), The University of Akron, especially Dr. AKM Arafat, Dr. Md. Zakirul Islam, and Dr. Mostak Mohammad, for their suggestions, brainstorming sessions, and inspiration. Also, I would like to thank my colleagues from Power Electronics and Energy System Laboratory (PEESL) at Mississippi State University, especially Mr. Ashik Amin, for his suggestions and support.

My sincere thanks to Dr. Malik Elbuluk and Dr. Robert Veillette from the University of Akron for guiding and inspiring me to explore different aspects of power electronics and control to comprehend their intricacies. I would also like to Dr. Saeed Anwar for his suggestions regarding different hardware issues.

The final recognition goes to my family, especially to my mother, Mrs. Bilkis Begum, wife, Rawshan Ara, and son, Umair Moinul Ahmad, for their love, encouragement, and patience.

Lastly, my father, who departed this world seventeen years ago, is a constant source of inspiration for me. It would not have possible without his sacrifice and love.

TABLE OF CONTENTS

LIST OF TABLES

LIST OF FIGURES

CHAPTER I

INTRODUCTION

1.1 Research motivation

The power electronic systems (PES) play a pivotal role in the automotive, aircraft, and ship-based traction applications [1]. Also, they are widely used in variable-frequency high-power industrial applications, medium-power medium-frequency applications, low-power, low-voltage consumer devices, accessories, and control applications [2]. In the 21st century, electric vehicles (EVs) and hybrid electric vehicles (HEV) have re-emerged and redefine the range of PES-based applications [3]-[4]. The PES has been an integral part of the motor drive and charging stations of the EV and HEV ecosystem for a higher degree of controllability, reliable service, and compact installation [5]. Electric ship (ES), more electric aircraft (MEA), smart grid, solid-state transformer (SST), and many other applications are integrating PES to increase efficiency, achieve compactness and reduce carbon emissions. Advanced communication technology and the PES are combined for efficient power transfer and resilient systems in the smart-grid application. Currently, the PES market is estimated at $23.35 billion in 2019 and estimated to have a $36.64 billion market size in 2027 [5]. Thus, the PES is evolving with the technology, redefining the traditional applications, and continuously being adopted in the new applications.

Power semiconductor switches are the core of the PES. The failure of these switches compromises the reliability of the PES. According to the industry survey, semiconductor failure accounts for 21% of the total PES failures [6]. Thus, the reliability of the power semiconductor

switches is essential for the overall robustness and resilience of the PES. Almost 42% of the medium- and high voltage PES use Insulated Gate Bipolar Transistor (IGBT) [8]. They experience fatal short-circuit failure (SCF) and aging-related open-circuit failure (OCF). SCF in the IGBTs are sudden, event-oriented, fatal to the PES, and provide little reaction-time [9]. Thus, the PES utilizes hardware-level protections such as circuit-breaker, fuse, etc., to isolate the SCF. Unlike SCF, the extremely slow accumulated degradation over time causes OCF in the PES. It is possible to monitor the degradation in real-time, predict their remaining useful lifetime (RUL), and avoid catastrophic failure using model-based data-driven prognosis methods [11]. However, the PES design and control do not include switch-health information to prevent the OCF. Thus, IGBT's degradation modeling and accurate RUL estimation are essential to extend the operating lifetime, ensure robustness, and avoid catastrophic PES failure.

The cascode GaN FET is a wide-bandgap power semiconductor switch that shows immense promise in high-power high-frequency applications. This switch has a higher breakdown voltage, low on-state resistance, high switching frequency [13]. It is estimated to have a $0.5 million market in 2018 and is projected to have a $300 million market in almost 2027 [14]. The primary failure mechanisms, such as piezo-electric failure, contact degradation, charge-trapping, and wire-bond degradation failure, are slow, accumulated over time, and cause OCF. Thus, the OCF in the cascode GaN FET is avoidable by accurate degradation modeling and lifetime estimation. Although the cascode GaN FETs show great promises, the PES industry is not confident about their production level reliability and robustness. Thus, the robust reliability study will increase its credibility in mission-critical applications.

System-level reliability and robustness are also essential for the PES. Although design-redundancy increases the PES robustness, it is not desirable considering cost- and space

constraints. Switch degradation mapping provides useful insight into switch life under degraded conditions. Intelligently integrating this switch-health information into the controller provides a low-cost and advanced option to ensure PESs' reliability and robustness. This degradation-aware controller will continuously monitor the switch-health, intelligently derate the PES to extend their lifetime, and shut down the PES smoothly when a fault occurs.

1.2 Research objective

Based on the research motivation, the objectives of this Ph.D. study are as follows:

Objective 1: Degradation modeling and RUL estimation of IGBT by addressing the following problems:

a. Fault-precursor-based degradation stage identification, and
b. Significant RUL estimation variance under harsh noise.

Objective 2: Degradation modeling and RUL estimation of cascode GaN FET by addressing the following problems:

a. Significant RUL estimation variance under severe noise,
b. Sample degeneracy and sample impoverishment, and
c. Low capability to trace the dynamic change in the fault-precursor.

Objective 3: Real-time degradation-aware controller design for the SST by:

a. Development of a behavioral switch-loss model for the cascode GaN FET, and
b. Degradation-aware optimal performance of the SST over its operating life.

CHAPTER II

MODERN APPLICATIONS AND STATUS OF RESEARCH IN RELIABILITY OF POWER ELECTRONIC SYSTEMS

2.1 Power electronic systems in everyday life

1.1.1 Types of power electronic systems

The PES enable highly efficient energy conversion in a wide range of applications such as automotive, renewable energy, adjustable-speed drives, high-voltage direct-current (HVDC), and aero-space [1]-[2]. The PESs are broadly categorized as follows:

1) DC-DC converters are used for DC voltage conversion and isolation.
2) Inverters are used for DC to AC voltage conversion and frequency conversion.
3) Rectifiers are used for AC to DC conversion.
4) Cyclo-converters are used for voltage and frequency conversion in AC-AC applications.

These converters are used standalone or in cascade, depending on the applications.

1.1.2 General architecture of power electronic systems

The general architecture of a PES is shown in Figure 2.1. The typical PES has - 1) the power-conversion stage and 2) the control stage. The power-conversion stage has an electrical power input, a power-conversion block, and an electrical power output. The power-conversion block generally comprises the power semiconductor switches and passive components such as resistors, capacitors, and inductors. These switches operate at frequencies ranging from a few hertz

(Hz) to hundreds of kilohertz, depending on the applications. The passive components are used as energy storage and filter for energy conversion. High-frequency (HF) transformers are also used in the power stage for galvanic isolation. These switches are controlled to store and extract energy from these passive components and HF transformers.

The control stage senses and processes the signals such as voltage, current, and temperature from the power stage and generates gate-driving signals for the switches to achieve desired performance. Moreover, this stage provides over-voltage, over-current, and over-temperature protection for the PES. The PES use micro-controllers, digital signal processors, or field-programmable gate arrays in the control stage.

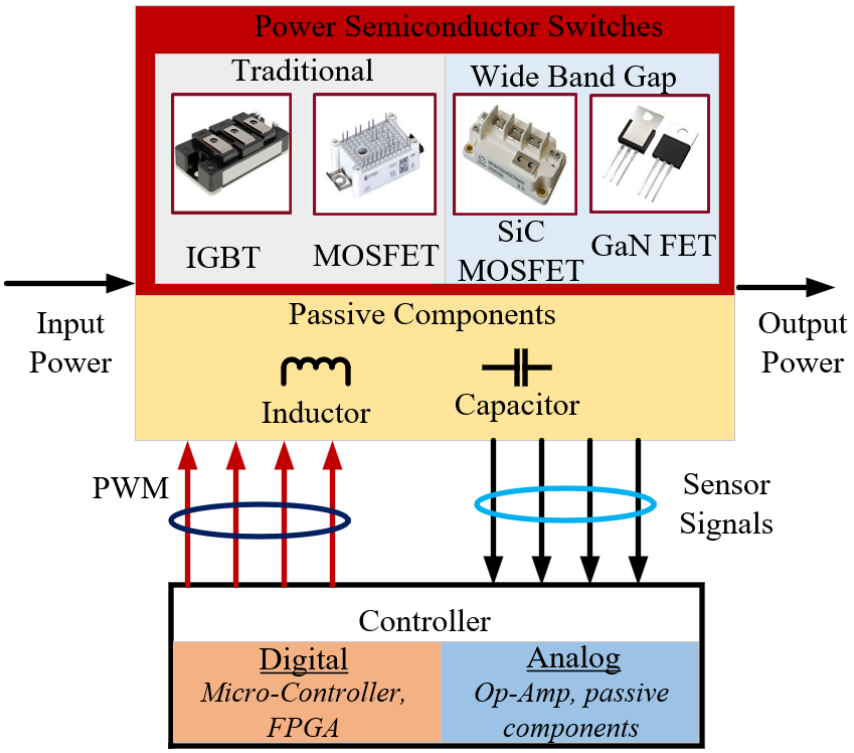

Figure 2.1 Typical power electronic systems architecture.

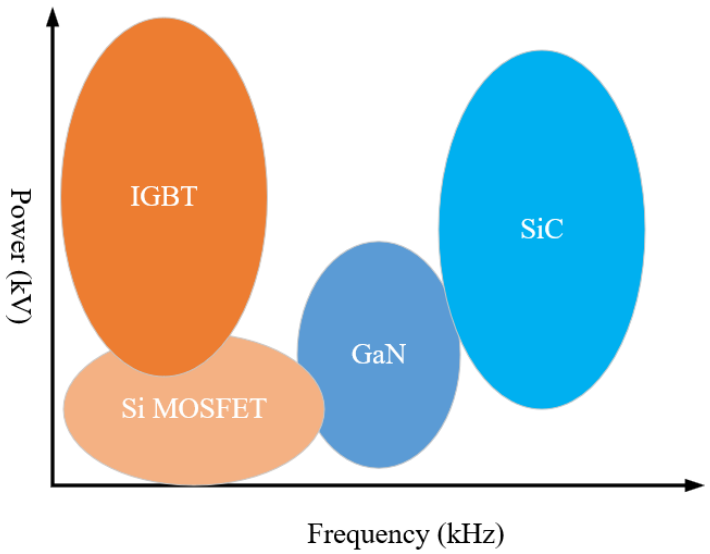

Figure 2.2 Switching frequency and power range of IGBT, Si MOSFET, GaN FET, and SiC MOSFET.

1.1.3 Types of power semiconductor switches

Power semiconductor switches are categorized as- 1) Silicon (Si) based traditional power semiconductor switches such as IGBT, MOSFET, Thyristor, TRIAC, Diode, and 2) wide bandgap (WBG) based Silicon Carbide (SiC) MOSFET and GaN FET. The power handling capability and operating frequency of these switches are shown in Figure 2.2. Thyristor and TRIAC are used in highly high-power, low-frequency (<1 kHz) applications. IGBT and Si MOSFET are the most popular switches in the medium frequency ranges. IGBT is used in high-power applications when the operating frequency is less than 10 kHz. Although Si-MOSFETs can operate around 100 kHz, their power handling capability reduces extremely (<1 kVA) at these frequencies [3]-[4]. The material properties of Si limit these switches' power handling capability and operating frequency. Thus, it is not possible to achieve high power at high frequency using these switches. Modern power electronic applications demand high power at high frequency to have a compact size that Si-based switches cannot meet. The WBG semiconductor switches are suitable for these high-

power high-frequency applications for their higher bandgap, high-temperature capability, and breakdown electric fields compared to Si, as shown in Table 2.1. The sizes of the passive components in the WBG based PES are reduced as these switches operate at a higher frequency.

Moreover, they have lower switching and conduction losses compared to the Si-based switches. Thus, the WBG-based PESs are compact and need a simpler thermal management system. Although these switches show immense potential, they are not widely accepted in the industry for their lack of operational history and product-life reliability.

Table 2.1 Comparison of physical properties of Si, SiC, and GaN [5]

Property	**Si**	**SiC**	**GaN**
Bandgap, E_g(eV)	1.12	3.3	3.4
Dielectric Constant, ε_r	11.80	9.7	9.5
Saturation drift velocity, (10^7 V/cm)	1.00	2.2	2.5
Thermal Conductivity, k(W/cmK)	1.50	5.00	1.3
Melting Point (^{o}C)	1420	2830	2500
Breakdown Electric Field, E_C (MV/cm)	0.25	3.00	3.5

1.1.4 Modern applications of power electronic systems

Traditionally, PESs are mainly used in high-power industrial applications and medium power medium frequency applications. Moreover, they are also used in low-power consumer devices and low voltage applications in the automotive, aircraft, and ships. In the 21st century, EVs and HEVS have redefined the range of PES-based applications [6]-[8]. The PES have been an integral part of the motor drive that provides traction power to the EV and HEV. EV charging

stations also replace traditional transformers with the PES for reliable service and compact installation [9]. The PES in a typical EV eco-system is shown in Figure 2.3. Electric ships (ES), more electric aircraft (MEA), smart grid, solid-state transformers, and many other applications incorporate the PES to have better efficiency, achieve compactness and reduce carbon emissions. Advanced communication technology and the PES are combined for efficient power transfer and improved system resilience in the smart-grid application. The PES is evolving along with the advancing technology, redefining the traditional applications, and continuously being adopted in new applications. However, the product-life reliability of the PES in these modern applications is the concern as a failure in the PES may cause catastrophic failure and result in loss of human life.

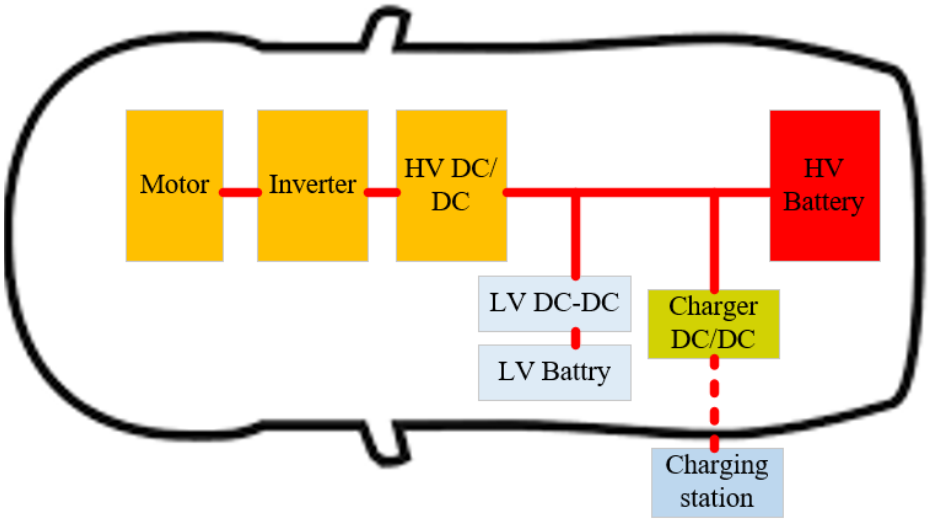

Figure 2.3 The power electronic systems in an electric vehicle.

1.1.5 Importance of operating time reliability of power electronic systems

The PESs' acceptability in an application depends on cost, efficiency, power density, reliability, and manufacturability [10]. Maximum efficiency and power density are desired as they ensure compact size, simpler thermal management, and reduced operating cost. Component cost is the most critical factor in consumer and industrial applications. However, safety is a higher priority than the cost in mission-critical applications such as automotive, aircraft, and ships where PES malfunction and failure may cause loss of life. Integrated reliability in manufacturing, design, and operation levels is essential for the safe operation of the PES. Reliability in the manufacturing process focuses on the operating time stress withstand capability of the components [11], and design-phase reliability emphasizes keeping the component stress within the rated condition. The PES has varying expected lifetime based on the application, as shown in Table 2.2. Thus, it is crucial to design the PES using components manufactured for the intended application and product life cycle. However, there are manufacturing-related defects present in the switches, and the PES experience over-rated conditions. Moreover, the cyclic thermal stresses during operation cause component-aging, lead to component and system failure. Although sincere care has been taken in manufacturing- and design-level reliability, sudden PES failure results in catastrophic consequences.

Table 2.2 The expected lifetime of power electronic systems in different applications [12].

Application	Expected lifetime
Automotive	15 years
Aircraft	24 years
Renewable energy	20-30 years
Industrial motor drive	5-20 years

The industry-wide survey found that power semiconductor switches are the most vulnerable component in a PES after the DC-link capacitors, as shown in Figure 2.4. Thus, reliability during the operating time has become an important research area in the modern PES.

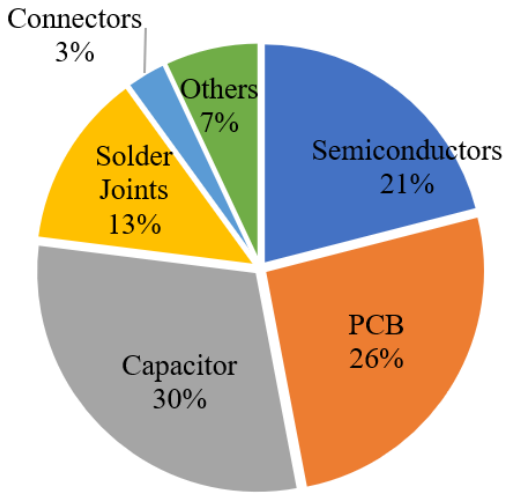

Figure 2.4 Component failure percentage in a power electronic system [13].

1.1.6 Recent trend in reliability study of power semiconductor switches

Power semiconductor switches experience stressors such as steady-state mean temperature, temperature cycling, humidity, dust, vibration, electromagnetic interference (EMI), etc. Among these stressors, high junction temperature and its variation cause 65% of the power semiconductor switches' failures, as shown in Figure 2.5. This temperature stress initiates degradation mechanisms such as wire-bond lift-off, solder fatigue, cracks in the solder joint, etc., and results in a switch failure. A significant number of researches have been conducted on the condition monitoring techniques for the power semiconductor switches to identify degradation and prevent catastrophic system failure.

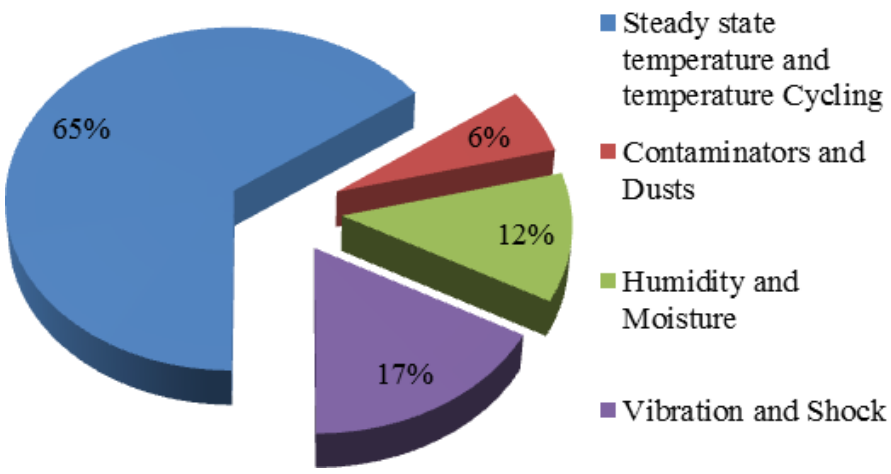

Figure 2.5 Stress sources for power semiconductor switch failures [14].

The condition monitoring techniques are broadly categorized in three categories: 1) direct method, 2) physics-of-failure (PoF) method, and 3) data-driven method. As the direct methods are offline, costly, and invasive, it is impossible to use these methods for real-time degradation monitoring. These methods use X-ray, scanning acoustic microscopy analysis, and scanning electronic microscopy (SEM) analysis to identify the switches' cracks and degradation [15]. PoF methods analytically model the switches' degradation under the presence of different stressors [16]-[18]. The degradation process is uncertain and random. These PoF methods cannot address the dynamic condition changes in the system.

Moreover, these methods do not consider manufacturing imperfections and also require precise switch structure and manufacturing information that is not publicly available in general. Although these methods provide insight into the switches' general degradation mechanism, they have limited degradation detection and RUL estimation capabilities during the operation. The switch-health experiences accelerated degradation at the end of its life. Thus, it is more practical

to estimate the switch's accurate RUL based on online health status for unexpected switch-failure prevention.

Data-driven methods use historical and real-time data to estimate the switch-health [19]-[21]. As these methods require little knowledge of the internal switch structure, it is possible to use these methods non-invasively and results in a lower variance in RUL estimation. These methods identify the fault precursors and trace these fault precursor trajectories to model the degradation progression. These models are adjusted in real-time to reflect the switch-health status. Although electrical parameters show significant sensitivity to the switch degradation [22]-[27], all these signals are not online measurable. Thus, identifying the appropriate parameters is extremely important for the precise and accurate health monitoring and prognosis study. However, several studies have been conducted on the fault precursor identification of IGBT and Si MOSFET. A few research have been conducted for the fault precursor identification of the cascode GaN FET. Moreover, this degradation information is not extensively used in the controller design of the switches. It will be critical for system-level reliability to integrate degradation information in the PES controller.

CHAPTER III

AUXILIARY PARTICLE FILTERING BASED ESTIMATION OF REMAINING USEFUL LIFE OF IGBT

The content of this chapter is based on M. S. Haque, S. Choi, and J. Baek, "Auxiliary Particle Filtering-Based Estimation of Remaining Useful Life of IGBT," in *IEEE Transactions on Industrial Electronics*, vol. 65, no. 3, pp. 2693-2703, March 2018.

3.1 Introduction

The prognosis study of IGBT has been drawing interest in recent years to improve power electronics systems' reliability to prevent unexpected failure. 42% of the power electronics system switches are IGBTs [14], [17], the second most vulnerable component motor-drive systems. According to the industry survey [18], the ratio of failure cost to the system cost for IGBT is around 80%. As the health condition of IGBT might degrade to failure within a very short time (~10 μs), scheduling the maintenance after the fault is not a feasible solution. Accurate RUL prediction is necessary to prevent system shutdown due to IGBT failures [19]. Estimating accurate RUL helps to schedule optimized maintenance for repairing and timely replacing faulty or degraded switches. Several studies have been conducted to identify the degradation mechanism and perform an accurate RUL estimation. The major degradation mechanism of IGBT is the die attachment degradation that results in wire-bond lift-off (WBLO) [20]-[21] and solder-fatigue [22]. The degradation can be observed using direct methods such as X-ray, Scanning Acoustics Microscopy (SAM) analysis. But these methods are offline, costly, and

destructive [23], [24]. Analytical methods have been widely developed based on the physics of failure mechanisms [15], [16], [18], [20]. However, analytical methods cannot address dynamic condition changes in the system and random noise, which results in a large variation in RUL estimation.

The data-driven method has been developed by analyzing trajectories of fault precursors. This method requires little knowledge of internal IGBT structure and can be applied online, cost-effectively, and non-destructive [24]-[25]. Moreover, this method shows the ability to adjust the degradation model according to varying operating conditions. Electrical parameters have shown a significant change in characteristics resulting from WBLO and solder fatigue [29], [31],[32]. Collector-emitter on-voltage ($V_{CE,ON}$), collector current (I_C), gate-emitter voltage (V_{GE}), gate-emitter threshold voltage ($V_{GE,TH}$), thermal resistance, electrical resistance, switch turn-on (T_{on}), and turn-off (T_{off}) time are identified as fault precursors for wire-bond related faults. These signals show sensitivity to the IGBT degradation [29]-[38]. In [39], the degradation monitoring method is proposed by monitoring case temperature (T_C) of IGBT modules in power converters. This method requires two thermal sensors for each IGBT at the interface between the baseplate and cold plate. The trajectory estimation and projection of these fault precursors are susceptible to large estimation variance because of measurement noise [27], [34].

To improve the accuracy in predicting the trajectories from highly noisy data, advanced nonlinear filters, including Kalman Filter (KF), Extended Kalman Filter (EKF), and Particle Filters (PF), have been extensively studied [39]-[44]. In [39], KF is used for the *RUL* estimation of IGBT. KF method shows better performance with a linear system and Gaussian noise. KF method shows a large variation in *RUL* estimation attributable to the high non-linearity of the IGBT degradation process. EKF is used to address the nonlinear system in [40]. First, EKF

performs linear approximation of nonlinear systems using the first two terms of the Taylor series and then applies the KF method for estimation. This method provides acceptable performance under limited non-linearity. EKF method results in a large variation in estimation when the system is highly nonlinear, or noise is non-Gaussian. But the system noise is not always Gaussian. PF method provides better estimation accuracy when either system is nonlinear or noise is non-Gaussian. In [41], Sequential Importance Resampling (SIR) PF method has been utilized for simulating trajectories of $V_{CE,ON}$. SIR PF can address the degeneracy problem in SIS PF [45]. However, SIR PF shows a 21% variance in *RUL* estimation. This variance is attributable to the loss of particle diversity, known as sample impoverishment. This problem arises because of resampling at each step, resulting in all particles originating from a common particle. This sample impoverishment results in a large variation in estimation. This variation is due to a reduction in diversity in particle sampling [46]-[47].

Auxiliary particle filtering (APF) introduces the particles' index as an additional variable for resampling, reducing sample impoverishment while increasing the samples' diversity [46]-[47]. Regularized particle filtering (RPF) and Rao Blackwell particle filtering (RBPF) also show similar capabilities. However, RPF requires an additional process for regularized resampling. It shows a greater root mean squared error (RMSE) than APF. RBPF method is more effective when the system's dimension is greater than 2. This method operates by segmenting the system into linear sub-systems [47]-[50]. Nature-inspired evolutionary optimization techniques such as Cuckoo Search (CS) techniques have been applied for reducing particle degeneracy and retaining diversity in samples [51]. In [52], CS PF has been used in bearing tracking problems where the number of particles is 500. In [53], the improved CS PF technique has been used for video tracking. This method shows better performance than generic particle filter and Particle Swarm

Optimization PF with more computation time. APF method is used for tracing and predicting *RUL* of IGBT with satisfactory precision and computation time.

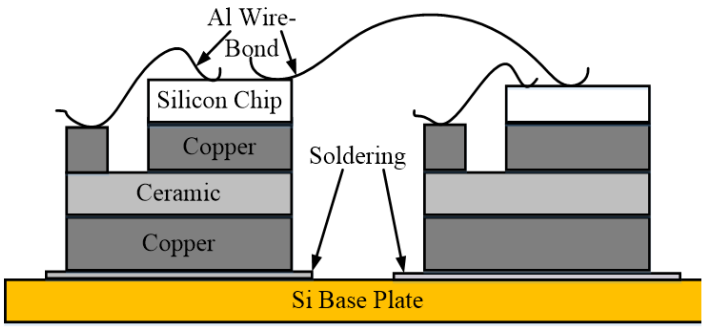

Figure 3.1 Cross-section of IGBT.

In this dissertation, Auxiliary Particle Filtering (APF) is proposed to further improve RUL estimation accuracy compared to the existing *RUL* estimation methods. This method will show better estimation capability than SIS PF and SIR PF due to its ability to diversity preservation in samples. This proposed method will also utilize the simple slope-based method to identify the region when degradation is evident and apply the APF method to reduce computation time. This chapter is logically organized as follows: Section 3.2 addresses the suitable fault precursors for WBLO and solder- fatigue. The fundamentals of the PF filter are discussed in Section 3.3. The proposed APF-based *RUL* estimation is described in Section 1.2. Section 3.4 provides experimental test results, which are followed by the conclusion in Section 3.5.

3.2 IGBT fault precursors

1.1.7 Stress on IGBT

Due to its capability to operate in high power density regions with high efficiency, IGBT has been widely used in power electronics applications [17], [20]. A cross-section of an IGBT is shown in Figure 3.1. IGBT is built by stacking different layers of copper and ceramic on the silicon (Si) base plate. SiO_2 soldering has been applied to hold stacks together. Silicon chips of different IGBT units are interconnected using Aluminum (Al) wire [17],[19]. WBLO, die-solder degradation, gate-oxide degradation, and package delamination mechanism cause open phase faults. The root cause of these fault mechanisms is thermal stresses during operation. Almost 65% of IGBT faults are caused by high steady-state temperature and temperature cycling [18].

The IGBT module materials such as copper, ceramic, and silicon have different coefficients of thermal expansions (CTE). IGBT is exposed to temperature cycling during operation, which results in mechanical stresses at die-joint and interconnections. These mechanical stresses eventually result in WBLO and solder fatigue [29]. Interconnection failure between Si die of different IGBTs is mainly due to WBLO [20]-[25]. Solder fatigue results from CTE mismatch and related physical stresses between different materials where cracks and voids are formed in solder adhesive between different stacks. WBLO and solder fatigue become dominant when IGBT operates under high frequency where heat generated during on-state cannot be removed during off-state. As a result, the steady-state temperature of a module increases. The temperature near the nominal characteristic temperature is more destructive than a similar variation in lower temperature [34].

1.1.8 Fault precursors of IGBT

The $V_{CE,ON}$, I_C, V_{GE}, $V_{GE,TH}$, $T_{on,}$ and T_{off} are identified as fault precursors of IGBT along with junction temperature (T_J) [10]-[14],[17]-[18]. Although T_J is the most influential parameter for degradation, direct T_J measurement is invasive and thus, impractical. Several studies have been conducted for the non-invasive estimation of T_J [1], [17]-[24]. T_J's estimation using temperature-sensitive electrical parameters (TSEP) has been preferred as it is non-invasive and requires no additional hardware. But TSEP performance deteriorates when the switching frequency of IGBT increases. Case temperature is also used as a fault precursor. This method requires two sensors per IGBT [25] which is costly in implementation. $V_{CE,ON}$ shows more sensitivity to degradation

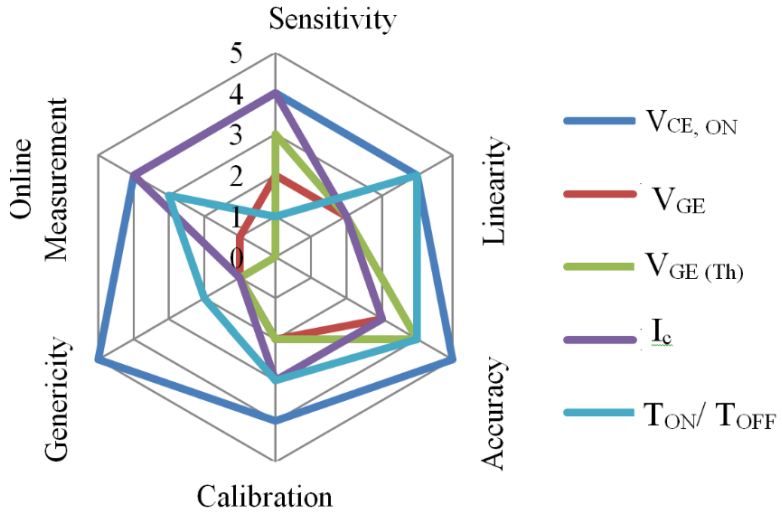

Figure 3.2 Performance comparisons of the fault precursors of IGBT.

compared to I_C, $V_{GE,}$ and $V_{GE,TH}$. $V_{CE,ON}$ changes significantly with aging while $V_{GE,TH,}$ and I_C change insignificantly [19]-[21]. Moreover, $V_{CE,ON}$ shows better online measurement capability and accuracy than other parameters. $V_{CE,ON}$ increases regularly after it reaches 3% of the initial

value. Before that, $V_{CE,ON}$ increases irregularly and slowly. IGBT is considered faulty when $V_{CE,ON}$ increases 20% of its initial value [1,15, 20]. $V_{GE,TH}$ is an effective fault precursor for gate oxide failure. The t_{on} and t_{off} are used as the fault precursor in the short circuit failure of IGBT [17-18]. However, these parameters show insignificant sensitivity to WBLO and solder fatigue. The performance of different precursors is shown in Figure 3.2. It is evident from Figure 3.2 that $V_{CE,ON}$ is the most appropriate fault precursor for investigating WBLO and solder fatigue due to its sensitivity, accuracy, and online measurement capability. However, $V_{CE,ON}$ is subject to harsh industrial noise, which results in a great amount of uncertainty in *RUL* estimation. This proposed method precisely addresses how to minimize the estimation variance.

3.3 Particle filtering

1.1.9 Fundamental of RUL estimation

Fundamental of the *RUL* estimation process using particle filtering methods in this proposed method is briefly depicted in Figure 3.3 with example. In Figure 3.3, cyan color shows the actual degradation trajectory of IGBT. At time *n-1*, the band of trajectories can be simulated using previous data and data-driven models. The blue line shows the band of trajectories. At time *n*, the data-driven model is updated when new data is available. Then, trajectories can be simulated using this updated model. These updated trajectories shown in maroon color show lower variance than the previous band of trajectories. The Bayesian tracking continuously updates estimation when the measurement is available to reduce RUL estimation variance. To further improve Bayesian tracking accuracy, APF can be applied, explained in detail in the following sections.

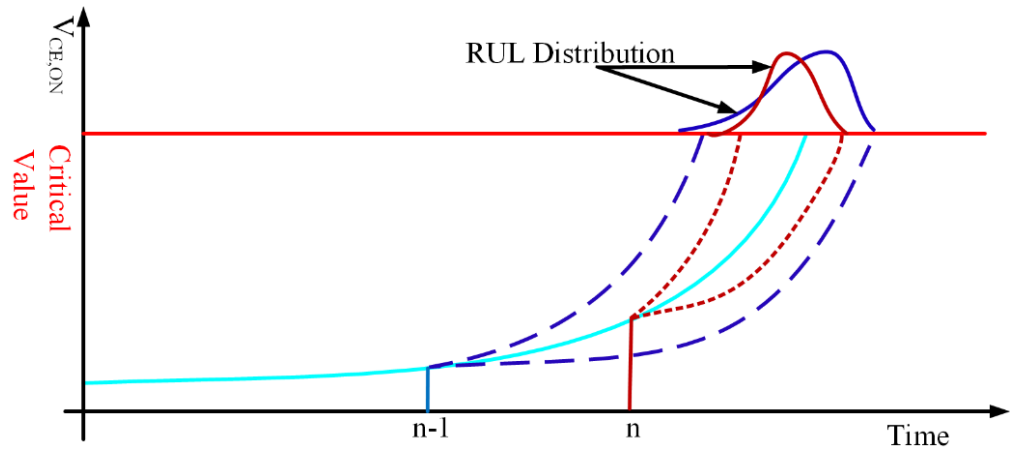

Figure 3.3 Prediction trajectories of the $V_{CE,ON}$.

1.1.10 Fundamentals of bayesian tracking

The trajectory of $V_{CE,ON}$ can be estimated using the Bayesian tracking system as follows:

$$V_{CE,ON,pre,n} = f\left(V_{CE,ON,pre,n-1}\right) + v_{n-1} \tag{3.1}$$

$$V_{CE,ON,act,n} = h\left(V_{CE,ON,pre,n}\right) + m_n \tag{3.2}$$

(3.1) and (3.2) are state transition model and measurement model, respectively, where $V_{CE,ON,act,n}$ is measured $V_{CE,ON}$ at time n, $V_{CE,ON,pre,n}$ is predicted $V_{CE,ON}$ at time n, v is process noise, m is measurement noise, and n is an integer. These models are formulated from time-series data using Auto-Regressive (AR) method [47]. These models are updated when a new measurement is available.

The estimation of $V_{CE,ON,pre,n}$ based on $V_{CE,ON,pre,n-1}$ and $V_{CE,ON,act,n-1}$ is a stochastic estimation problem due to presence of noise and is expressed as $p(V_{CE,ON,pre,n}|V_{CE,ON,act,n})$. This distribution is known as the posterior distribution and can be defined by the measurement noise, m_n, and measurement model in (3.2). At time $n=0$, this probability is expressed as follows:

$$p\left(V_{CE,ON,pre,0}\middle|V_{CE,ON,act,0}\right) = p\left(V_{CE,ON,pre,0}\right) \tag{3.3}$$

If there is no prior knowledge available in (3.3), it may be chosen as a constant probability distribution. Then, distribution in (3.3) can be updated whenever a new measurement is available. Over time, this distribution will closely approximate actual $p(V_{CE,ON,pre,n}|V_{CE,ON,act,n})$ as shown in Figure 3.4. This approximation is known as importance density function, $q(V_{CE,ON,pre,n}|V_{CE,ON,act,n})$.

In the prediction step, $V_{CE,ON,pre,n}$ is predicted based on the previous measurement using the Chapman-Kolmogorov equation as follows:

$$\begin{aligned} &p\left(V_{CE,ON,pre,n}\,|V_{CE,ON,act,n-1}\right) = \\ &\int p\left(V_{CE,ON,pre,n}\middle|V_{CE,ON,pre,n-1}\right) p\left(V_{CE,ON,pre,n-1}\middle|V_{CE,ON,act,n-1}\right) dV_{CE,ON,pre,n-1} \end{aligned} \tag{3.4}$$

where $p(V_{CE,ON,pre,n}|V_{CE,ON,pre,n-1})$ is the transition probability distribution function (PDF) and $p(V_{CE,ON,pre,n-1}|V_{CE,ON,act,n-1})$ is the posterior PDF at time $n-1$. Transition PDF is defined by (3.1). In update step, $p(V_{CE,ON,pre,n}|V_{CE,ON,act,n})$ can be written using Bayes rule as follows:

$$\begin{aligned} &p\left(V_{CE,ON,pre,n}\,|V_{CE,ON,act,n}\right) \\ &= \frac{p\left(V_{CE,ON,act,n}\,|V_{CE,ON,pre,n}\right) p\left(V_{CE,ON,pre,n}\,|V_{CE,ON,act,n-1}\right)}{p\left(V_{CE,ON,act,n}\,|V_{CE,ON,act,n-1}\right)} \end{aligned} \tag{3.5}$$

where $p(V_{CE,ON,act,n}|V_{CE,ON,pre,n})$ is likelihood function and $p(V_{CE,ON,act,n}|V_{CE,ON,act,n-1})$ is normalizing constant. The normalizing constant is defined as follows:

$$\begin{aligned} &p\left(V_{CE,ON,act,n}\,|V_{CE,ON,act,n-1}\right) \\ &=\int p\left(V_{CE,ON,act,n}\,|V_{CE,ON,pre,n}\right)p\left(V_{CE,ON,pre,n}\,|V_{CE,ON,act,n-1}\right)dV_{CE,ON,pre,n} \end{aligned} \tag{3.6}$$

The following is found by putting (3.4) into (3.5),

$$\begin{aligned} &p\left(V_{CE,ON,pre,n}\,|V_{CE,ON,act,n}\right)= \\ &\frac{p\left(V_{CE,ON,act,n}\,|V_{CE,ON,pre,n}\right)}{p\left(V_{CE,ON,act,n}\,|V_{CE,ON,act,n-1}\right)}\times\int p\left(V_{CE,ON,pre,n}\,|V_{CE,ON,pre,n-1}\right)p\left(V_{CE,ON,pre,n-1}\,|V_{CE,ON,act,n-1}\right)dV_{CE,ON,pre,n-1} \end{aligned} \tag{3.7}$$

If (3.1) and (3.2) are linear and associated noises are Gaussian, posterior PDF, state transition PDF, and likelihood PDF are Gaussian. In this case, the integral in (3.7) can be computed analytically. Then, KF can trace the fault precursor's trajectory precisely [42], [48]-[50]. If the system is slightly nonlinear and underlying noises are Gaussian, the EKF method approximates the system as linear using the Taylor series expansion. Then, KF can be applied to trace the trajectory of the fault precursor. However, EKF results in a more significant RUL estimation variation due to approximation for highly nonlinear systems [47]-[48]. For a highly nonlinear system or non-Gaussian noise, the integral in (3.7) cannot be computed analytically. In this case, the PF method can be applied to compute analytically intractable integral using the numerical method.

1.1.11 The particle filtering

In PF, the posterior PDF is represented by the random samples, and associated weights, known as the importance of weight, are calculated as follows:

$$p\left(V_{CE,ON,pre,n} \mid V_{CE,ON,act,n}\right) \approx \sum_{i=1}^{N} w_n^i \delta\left(V_{CE,ON,pre,n} - V_{CE,ON,pre,n}^i\right) \tag{3.8}$$

where $\delta(\cdot)$ is Dirac-Delta function, w^i_n is importance weight of i^{th} sample at time n, and i is the index of i^{th} sample drawn from posterior PDF. These random samples are known as particles. The importance weight of particles is computed using the importance sampling principle [48].

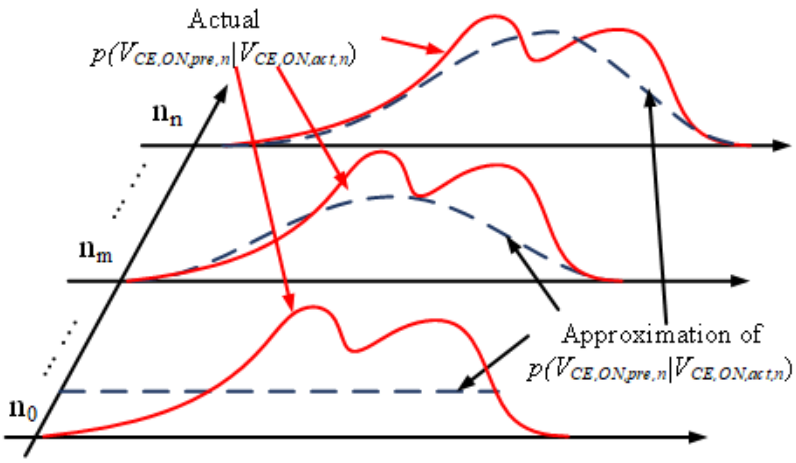

Figure 3.4 Evolution of $p(V_{CE,ON,pre,n}|V_{CE,ON,act,n})$ over time.

1.1.11.1 Computation of importance weights

The importance weight of the i^{th} particle is defined as follows:

$$w_n^i \propto \frac{p\left(V_{CE,ON,pre,n}^i \mid V_{CE,ON,act,n}\right)}{q\left(V_{CE,ON,pre,n}^i \mid V_{CE,ON,act,n}\right)} \tag{3.9}$$

where $\Sigma_i w_n{}^i=1$. In Figure 3.5, importance weight is the ratio of posterior probability and importance probability at that point. The importance PDF is the Gaussian approximation of non-Gaussian PDF. The importance PDF can be analyzed as follows:

$$\begin{aligned} &q\left(V^i{}_{CE,ON,pre,n} \mid V_{CE,ON,act,n}\right) = \\ &q\left(V^i{}_{CE,ON,pre,n} \mid V^i{}_{CE,ON,pre,n-1}, V_{CE,ON,act,n}\right) q\left(V^i{}_{CE,ON,pre,n-1} \mid V_{CE,ON,act,n-1}\right) \end{aligned} \tag{3.10}$$

The numerator in (3.9) can be analyzed as follows:

$$\begin{aligned} &p\left(V^i{}_{CE,ON,pre,n} \mid V_{CE,ON,act,n}\right) = \\ &p\left(V^i{}_{CE,ON,act,n} \mid V^i{}_{CE,ON,pre,n}\right) p\left(V_{CE,ON,pre,n} \middle| V_{CE,ON,pre,n-1}\right) p\left(V^i{}_{CE,ON,pre,n-1} \mid V_{CE,ON,act,n-1}\right) \end{aligned} \tag{3.11}$$

Putting (3.10) and (3.11) into (3.9), the importance weight can be expressed as follows:

$$\begin{aligned} w_n \alpha & \frac{p\left(V_{CE,ON,pre,n-1} \mid V_{CE,ON,act,n-1}\right)}{q\left(V_{CE,ON,pre,n-1} \mid V_{CE,ON,act,n-1}\right)} \frac{p\left(V_{CE,ON,act,n} \mid V_{CE,ON,pre,n}\right) p\left(V_{CE,ON,pre,n} \mid V_{CE,ON,pre,n-1}\right)}{q\left(V_{CE,ON,pre,n} \mid V_{CE,ON,pre,n-1}, V_{CE,ON,act,n-1}\right)} \\ = w_{n-1} & \frac{p\left(V_{CE,ON,act,n} \mid V_{CE,ON,pre,n}\right) p\left(V_{CE,ON,pre,n} \mid V_{CE,ON,pre,n-1}\right)}{q\left(V_{CE,ON,pre,n} \mid V_{CE,ON,pre,n-1}, V_{CE,ON,act,n-1}\right)} \\ = w_{n-1} & \tilde{w}_n \end{aligned} \tag{3.12}$$

where

$$\tilde{w}_n = \frac{p\left(V_{CE,ON,act,n} \mid V_{CE,ON,pre,n}\right) p\left(V_{CE,ON,pre,n} \mid V_{CE,ON,pre,n-1}\right)}{q\left(V_{CE,ON,pre,n} \mid V_{CE,ON,pre,n-1}, V_{CE,ON,act,n-1}\right)} \tag{3.13}$$

where $\tilde{w}$ is incremental importance weight. This incremental importance weight is computed at each step. In (3.12), importance weight is estimated using a recursive method. This PF method is known as SIS PF. SIS's advantage is reducing the computational burden by evaluating incremental importance weight instead of evaluating the importance weight's whole expression.

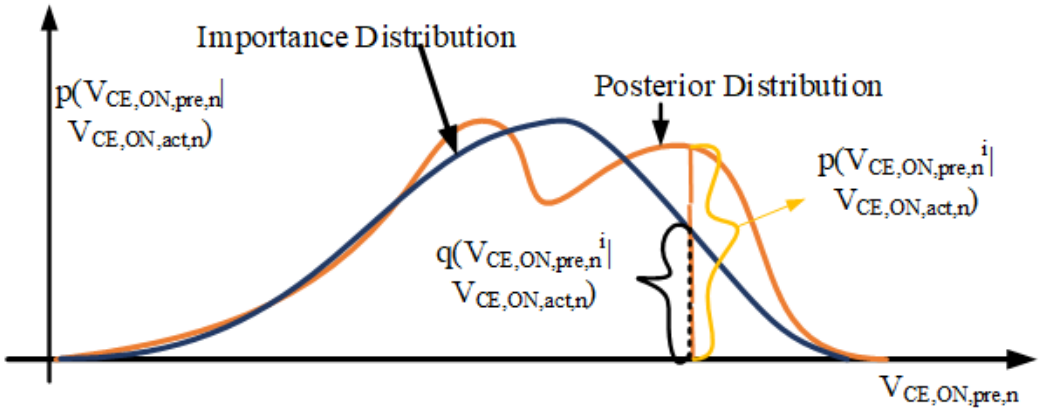

Figure 3.5 Weight calculation from posterior PDF and the importance PDF.

However, variance increases along with the number of iterations in this method because of weight degeneracy. This variance increase eventually results in the process of power wastage.

1.1.12 Resampling

The resampling step is introduced in the SIS algorithm to overcome weight degeneracy. The resampling step's basic principle is duplicating particles with higher weights and eliminating particles with lower weights so that every particle's weight becomes the same, as shown in Figure 3.6. Based on this principle, (3.8) can be written as follows:

$$p\left(V_{CE,ON,pre,n} \mid V_{CE,ON,act,n}\right) \approx \frac{1}{N}\sum_{i=1}^{N}\delta\left(V_{CE,ON,pre,n} - V_{CE,ON,pre,n}^{i}\right) \tag{3.14}$$

This method is called Sampling Importance Resampling (SIR). As the resampling step is computationally costly, this step is conducted when the number of high-density region particles is less than the effective number of particles, N_{eff}. In the resampling step, high-weighted particles are duplicated, and low-weighted particles are discarded. Most of the particles are originated from high weighted particles after some resampling steps. This phenomenon is known as sample impoverishment. The sample impoverishment is attributable to a lack of diversity in particles, resulting in a significant estimation variation.

1.2 Proposed condition-based auxiliary particle filtering for precise *RUL* estimation

Particle filter has been the emerging methodology to improve tracing and prediction of trajectory. PF method faces sample-degeneracy and sample-impoverishment results in a significant variation in *RUL* estimation. Those problems can be sufficiently mitigated by an auxiliary particle filter (APF). In this study, APF is proposed for the *RUL* estimation of IGBT.

1.2.1 Auxiliary particle filtering

In APF, the index of the sampled particles has been introduced as an auxiliary variable. This auxiliary variable increases the dimensionality of the particle, which helps to reduce variation in estimation. APF method takes samples to show that particles that show better compatibility with the next measurement have a better chance of survival [47]. For this, APF takes the samples in pairs $\{V_{CE,ON,pre,n}{}^{i}, j^{i}\}$ instead of $V_{CE,ON,pre,n}$ where, j is the i^{th} particle's index at *n-1*.

The joint probability of pair $\{V_{CE,ON,pre,n}{}^{i}, j^{i}\}$ which is proportional to the product of state transition PDF, $p(V_{CE,ON,act,n}|V_{CE,ON,pre,n})$ and importance weight of these particles. Such a relationship can be expressed as follows:

$$p\left(V_{CE,ON,pre,n}, j \,|\, V_{CE,ON,act,n}\right) \propto p\left(V_{CE,ON,act,n} \,|\, V_{CE,ON,pre,n}\right) p\left(V_{CE,ON,pre,n} \,|\, V^{i}_{CE,ON,pre,n-1}\right) w^{j}_{n-1} \tag{3.15}$$

In APF, first, the particles are drawn from this joint probability, and then, the index is discarded to sample from marginal PDF, $p(V_{CE,ON,pre,n}|V_{CE,ON,act,n})$. The particles are drawn from the importance PDF due to the non-Gaussian nature of this marginal PDF. The importance PDF, $q(V_{CE,ON,pre,n}, j^{i}|V_{CE,ON,act,n})$ can be expressed as follows:

$$q\left(V_{CE,ON,pre,n}, j \,|\, V_{CE,ON,act,n}\right) \propto q\left(V_{CE,ON,act,n} \,|\, \mu^{i}_{n}\right) q\left(V_{CE,ON,pre,n} \,|\, V^{i}_{CE,ON,pre,n-1}\right) w^{j}_{n-1} \tag{3.16}$$

where μ_n is mean of $q(V_{CE,ON,pre,n}|V_{CE,ON,act,n})$ which is defined as follows:

$$\mu_n = E\left[\, q\left(V_{CE,ON,pre,n} \,|\, V_{CE,ON,act,n}\right)\right] \tag{3.17}$$

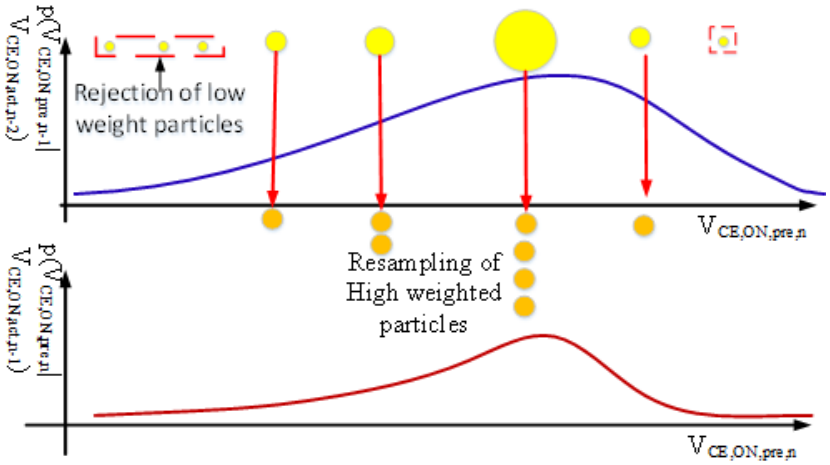

Figure 3.6 Resampling step in the particle filter.

Putting (3.15) and (3.16) in (3.9), the i^{th} particle's importance weight can be computed as follows:

$$w_n \propto \frac{p\left(V_{CE,ON,act,n} \mid V^{i}_{CE,ON,pre,n}\right)}{q\left(V_{CE,ON,act,n} \mid \mu_n\right)} \tag{3.18}$$

1.2.2 Remaining useful life estimation

The algorithm of APF-based *RUL* estimation is shown in Figure 3.7. The models (3.1) and (3.2) are built from IGBT experimental data, and a suitable importance PDF is chosen. According to these models and importance PDF, $V_{CE,ON}$ is predicted. These predicted values are compared with $V_{CE,ON,act,}$ and models are adjusted according to such measurement. *N* number trajectories of $V_{CE,ON}$ are simulated according to these adjusted models. *RUL* is estimated by calculating the time taken to reach to critical value from these trajectories. *RUL* at time *n* is calculated as follows:

$$RUL_n = n_f - n \tag{3.19}$$

where RUL_n is RUL estimated at time n, n_f is the time to reach the critical $V_{CE,ON}$ of fault precursor from the present time n. In Figure 3.8, RUL estimation is depicted at time n. For each particle, a trajectory of a fault precursor can be simulated. For 1st particle, RUL is $RUL_n^1 = n_1 - n$; for N^{th} particle, RUL is $RUL_n^N = n_N - n$; and for actual RUL is $RUL_r = n_r - n$; where n_r is the time when IGBT under test failed.

The state transition model and the measurement model can be updated using the sampling instance's AR method. The projection of the trajectory is modified according to these updated models. It is observed that when IGBT enters a new region, the resampling step takes place frequently. After that, APF continues tracking trajectory with almost all the particles in the high-density region. During this period, particles have practically equal weight. Thus, the weights of particles are considered equal for simplification in (3.20).

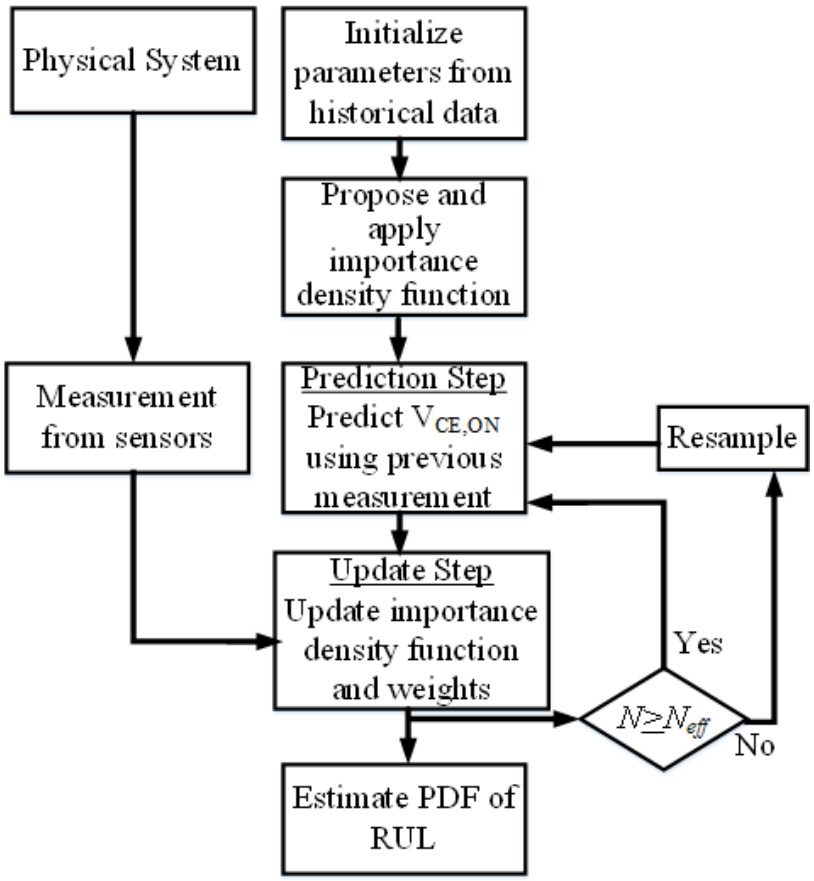

Figure 3.7 The Auxiliary Particle Filtering based *RUL* estimation algorithm.

The error in *RUL* estimation is the yardstick for performance comparison. Usually, Mean Absolute Error (MAE) is used when the error is constantly distributed, where RMSE is used when the error distribution is not constant. Moreover, RMSE takes the effect of outliers into account where MAE nullifies the effect of outliers. Because of these advantages, RMSE is more applicable to this study. The error in *RUL* estimation is calculated as follows:

$$Error = \sqrt{\frac{1}{N}\sum_{N=1}^{N}\left(RUL_r - RUL^i\right)^2} \tag{3.20}$$

where RUL_r is the actual RUL, RUL^i is the RUL estimated for i^{th} particle drawn from the importance density function.

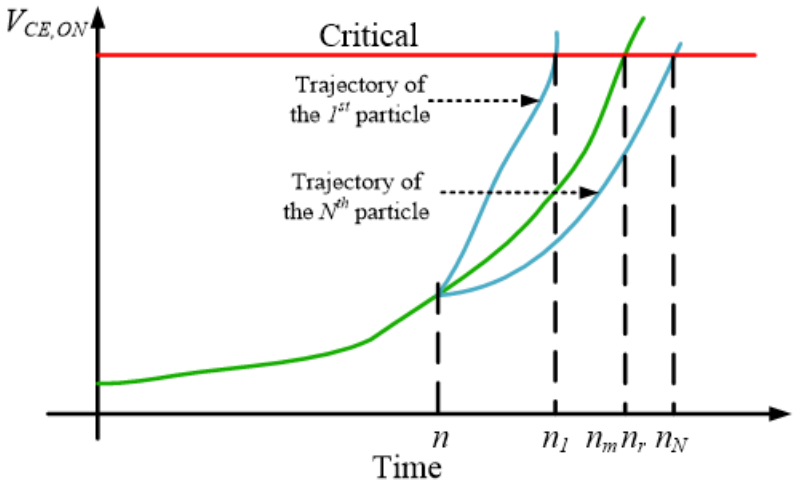

Figure 3.8 RUL estimation at time n.

1.2.3 Condition-based application of APF

To further improve the accuracy in APF based RUL estimation, APF is applied based on the approximated condition of IGBT. The degradation and condition of IGBT and resultant change of $V_{CE,ON}$ is categorized into three regions- healthy region, constant increase region, and exponential increase region, described as follows:

1) *Region 1* (*Healthy region*): When a new IGBT starts operation, change in $V_{CE,ON}$ is very insignificant. The slope of the trend line of $V_{CE,ON}$ in this region is almost zero. The state transition equation in this region can be expressed as follows:

$$V_{CE,ON,pre,n} = V_{CE,ON,pre,n-1} + v_{n-1} \tag{3.21}$$

The initial PDF of $V_{CE,ON,pre,0}$ is $p(V_{CE,ON,pre,0}) \sim N(1.95,0.12)$ where the $p(v_0) \sim N(0,0.12)$. The mean value of $p(V_{CE,ON,pre,0})$ is on-state voltage of IGBT from data sheet.

2) Region 2 (Constant change region): $V_{CE,ON}$ increases linearly in this region. This region indicates degradation in IGBT. The slope of the trend line in this region is positive, but the slope change is zero or insignificant. The state transition equation in this region can be expressed as follows:

$$V_{CE,ON,pre,n} = V_{CE,ON,pre,n-1} + a\Delta n + v_{n-1} \tag{3.22}$$

where a is the slope of the trend line. The coefficients of the most appropriate trend-line are estimated using the previous 20 points. The initial PDF of process noise in region 2 is $N(0,0.14)$.

3) *Region 3* (*Exponential change region*): $V_{CE,ON}$ increases exponentially in this region and reaches a critical value which indicates switch failure. The slope of the trend line is rapidly changing in this region. The state transition equation can be expressed as follows:

$$V_{CE,ON,pre,n} = \frac{1}{l}\sum_{l=1}^{p} V_{CE,ON,pre,n-l}\, exp\left[\left(b^{p}+c\right)\Delta n\right] + v_{n-1} \tag{3.23}$$

where b and c are the coefficients of the AR model and l is the backward data. According to Markov's assumption, l is set at 1. For l=1, p=1 and c=0. The value of b is estimated using the minimum Akaike Information Criterion (AIC). The initial PDF of process noise in region 3 is $N(0,0.15)$. The measurement model for IGBT is as follows:

$$V_{CE,ON,act,n} = \left(l - d^{l}\right)V_{CE,ON,pre,n} + m_n \tag{3.24}$$

where d is the constant, which is dependent on the AR model. The one-step prediction model is used, which gives l=1 and d=0. The PDF of the initial measurement noise is $N(0,0.34)$. IGBT remains in region1 until $V_{CE,ON}$ increases 2% of the initial value. It shows a constant rise in $V_{CE,ON}$ up to 5% of the initial value, and then it enters region three, where $V_{CE,ON}$ increases exponentially. In this study, APF is applied based on this segmentation of $V_{CE,ON}$ trajectory.

The noise distribution is assumed Gaussian under the central limit theorem. The central limit theorem suggests noise can be modeled as Gaussian noise when the number of particles is greater than 30. This assumption improves computation time and provides equivalent performance in *RUL* estimation.

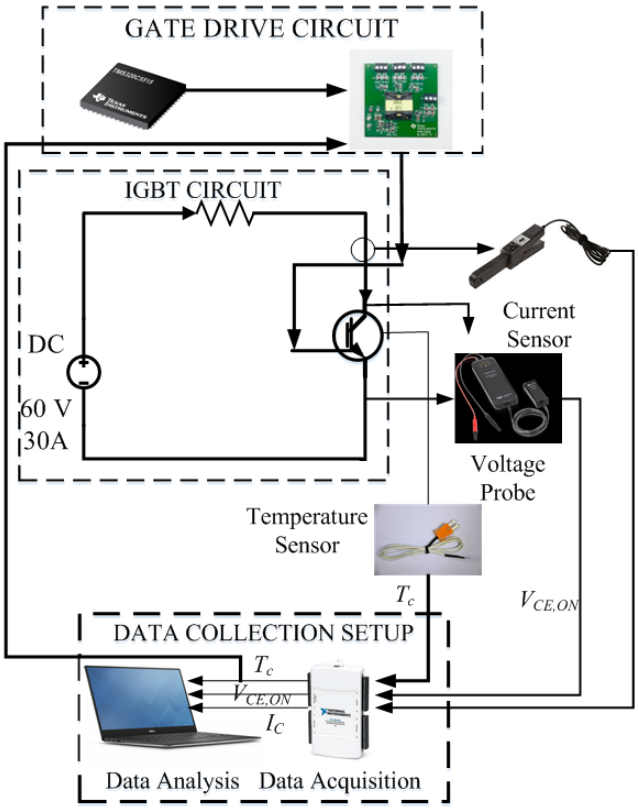

Figure 3.9 Schematic diagram of the experimental setup.

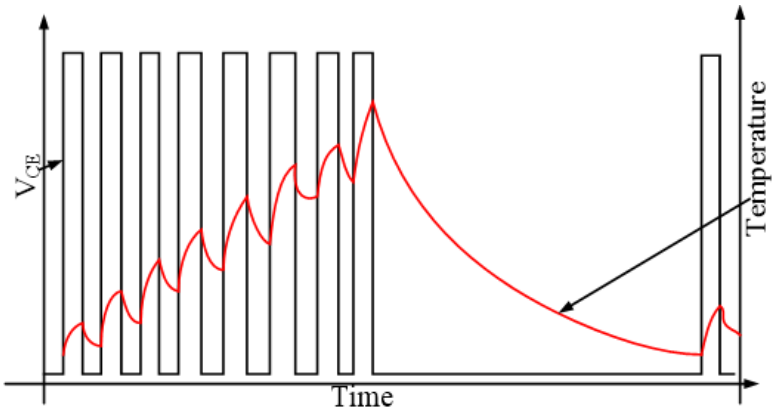

Figure 3.10 Temperature swing during the power cycling test.

3.4 Experimental test

1.2.4 Experimental environment

The experimental test is performed to verify the performance of the proposed APF-based *RUL* estimation. Power cycling tests are performed on IGBT to identify WBLO and solder fatigue mechanisms. The block diagram of the test setup is shown in Figure 3.9. The testbed includes a DC power supply, driver circuit, and resistive load. The switching of IGBT is controlled by a gate driver circuit that utilizes TI-DSPF28335. T_C is acquired using *k* type of thermocouple and $V_{CE,ON}$ is monitored using a differential voltage probe. IGBT is subject to temperature cycling during the power cycling test that emulates IGBT's stress in industrial applications, as shown in Figure 3.10. When T_C reaches 150^{o}C, switching is stopped so that IGBT is cooled down to 25^{o}C. This temperature-dependent process is automated using the TI DSP. $V_{CE,ON}$, $I_{C,}$ and T_C are acquired using NI DAQ USB 9001. These tests are carried out on IGBT (model number: FS30R06W1E3) from Infineon Technologies. The break-down voltage of these IGBTs is 600 V, and the maximum current is 20 A. The experiments are conducted at voltage level 60 V and current 30 A.

The test is conducted with seven sets of IGBTs under similar operating conditions. Each of these sets comprises 6 IGBTs. 35 IGBTs are used for formulating the empirical model and PDF. The remaining 7 IGBTs are used for validation of the proposed *RUL* method. 100 iteration of the Monte Carlo (MC) simulations are conducted. In this study, only the median trajectories are shown. The number of effective particles is set at 80% of the total number of particles so that acceptable performance in *RUL* estimation is achieved with reasonable computation time.

1.2.5 Experimental results

1.2.5.1 Scanning electronic microscopic (SEM) imaging of the IGBT under degradation

Figure 3.11 shows the SEM image of IGBT1 before and after the power cycling test under the conditions. The wire-bond status before and after the power cycling test is shown in Figure 3.11 (a) and (b), respectively. Figure 3.11 (c) shows that the lift-off area's zoomed picture in Figure 3.11 (b).

Under the testing conditions, the estimated *RUL* using the SIR PF method is 73 hours for 30 particles. IGBT failed after 60 hours of operation. This method shows a variation of up to 21.6 % in *RUL* estimation. In the following sections, the proposed APF method is applied for the *RUL* estimation, which will clearly show the improvement in *RUL* estimation for IGBT.

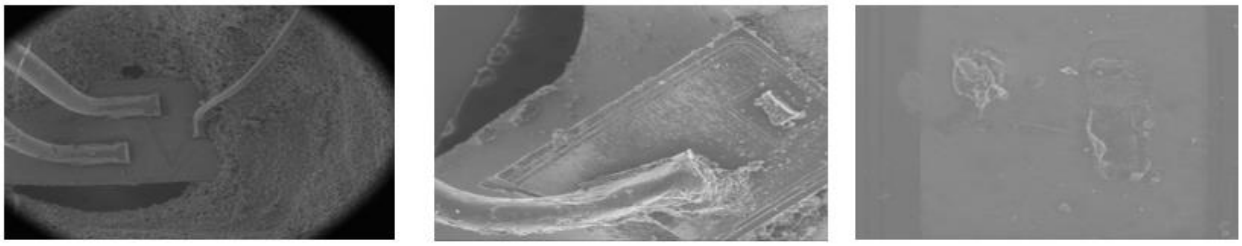

Figure 3.11 (a) Before the test, (b) After the test, and (c) Zoom of WBLO area.

1.2.5.2 Change of $V_{CE,ON}$ under degradation

$V_{CE,ON}$ trajectories for seven IGBTs is shown in Figure 3.12. The critical $V_{CE,ON}$ is 2.5 V which is a 20% increase from a mean of initial $V_{CE,ON}$. The slope of the trend line for IGBT1 is calculated for every 20 data points and plotted as shown in Figure 3.13. It is observed that the

slope of the 20th trend line is near zero. A positive slope can be observed between the 21st to 40th trend lines with an insignificant slope change. From 41st to 60th trend line, the slope is positive and changes faster in region 3. The segmentation of the whole trajectory into three regions is shown in Figure 3.13. It is observed that region 1 extends up to $V_{CE,ON}$ increasing by 2.5-3%, IGBT remains in region two until $V_{CE,ON}$ increases by 5-6% from the initial value, and then, it enters region 3.

1.2.5.3 RUL estimation using APF method

30-particle SIR PF and APF methods are applied to $V_{CE,ON}$ from IGBT1 shown in Figure 3.14. RMS error is 22% and 17.8% for 30- particle SIR PF and APF, respectively. Simulated trajectories for the different numbers of particles are shown for APF and SIR PF in Figure 3.15 (a) and (b), respectively. For a 100-particle APF, the simulated trajectory is sufficiently close to the actual trajectory with low variance.

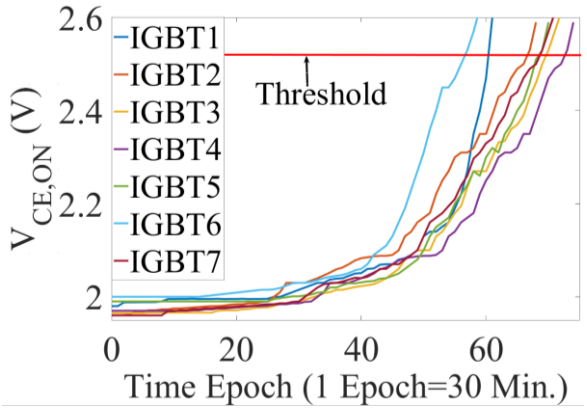

Figure 3.12 $V_{CE,ON}$ with time for seven IGBTs.

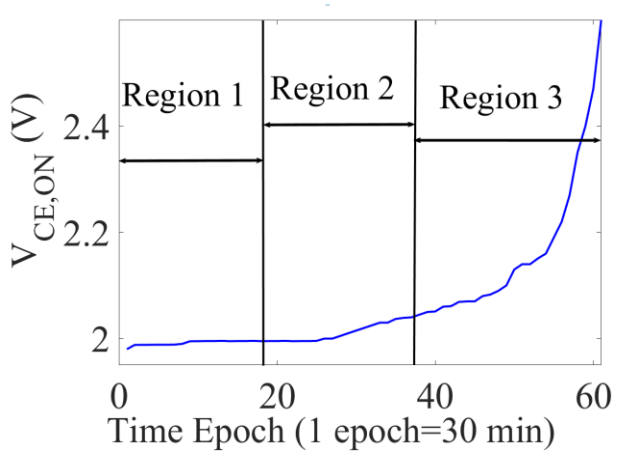

Figure 3.13 The slope of the trend line of the $V_{CE,ON}$.

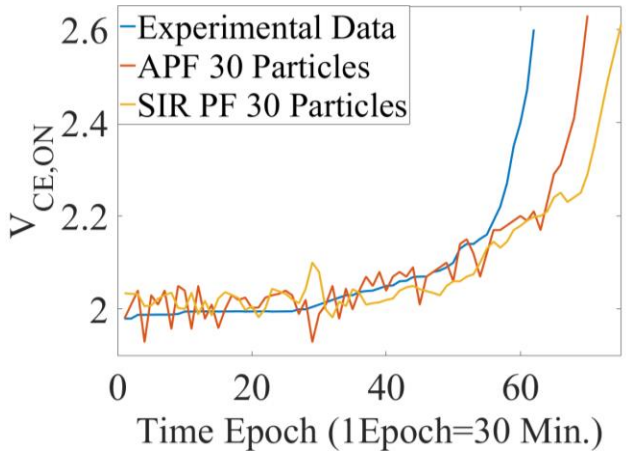

Figure 3.14 APF filter and SIR PF trajectory of $V_{CE,ON}$ for IGBT1.

RMS error decreases in line with the increase in the number of particles for both APF and SIR PF. However, APF shows a better performance than SIR PF. RMS error for APF and SIR PF is shown

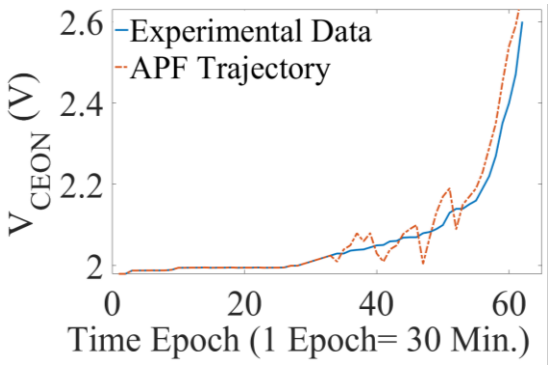

Figure 3.15 APF Trajectory when $V_{CE,ON}$ is in region 3.

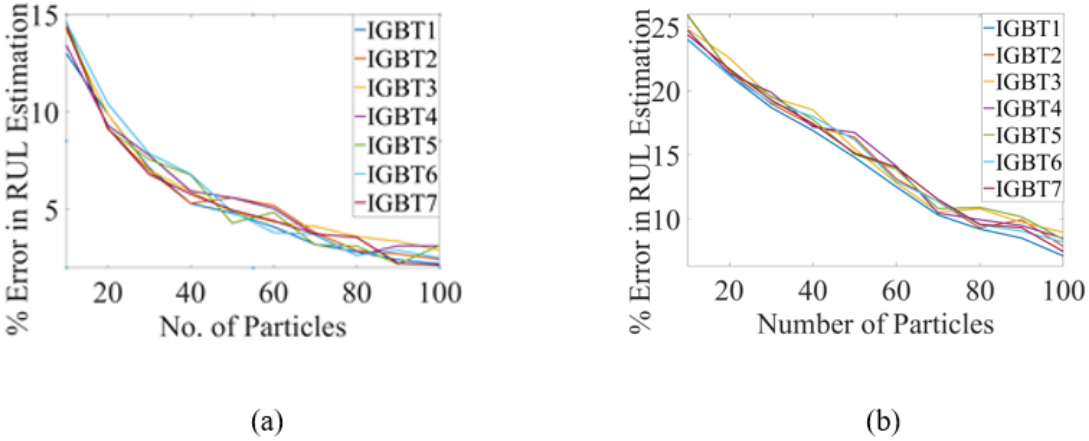

Figure 3.16 Error in *RUL* estimation for (a) APF and (b) SIR PF when estimation process starts in region 3.

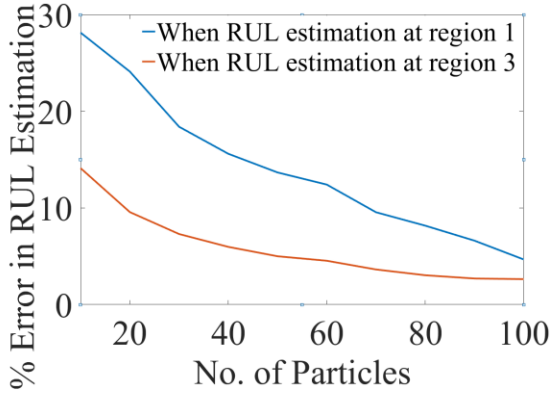

Figure 3.17 Comparison of % error in *RUL* estimation.

in Figure 3.15 (a) and (b), respectively, when applied in region 1. The average RMS error drops from 29% to 7% for APF when the number of particles is increased from 10 to 100. However, the variance is further reduced when APF is applied while $V_{CE,ON}$ reaches 5% of the initial value (in region3).

When the APF method is applied in region 3, the initial value $p(v_0)$ is $N(0,0.15)$. RMS error in *RUL* estimation drops almost 80% for a 10-particle APF. In Figure 3.15, the median APF simulated trajectory of $V_{CE,ON}$ for $IGBT_1$ is shown. RMS error for APF and SIR PF is shown in Figure 3.16 (a) and (b), respectively, when applied in region 3. In Figure 3.17, it is shown that the average RMS error is reduced significantly when APF is used in region three instead of region 1.

1.2.5.4 Effect of noise on APF-based RUL estimation

Particle filtering needs both process noise and measurement noise for its operation. Both the state transition equation and measurement equation lose their stochastic nature without process noise and measurement noise. For measurement noise, the percentage error in *RUL* estimation decreases with increasing process noise and increases as process noise increases. For process noise, the % error in *RUL* estimation always increases with the rise in measurement noise. The APF and SIR PF performance are shown in Figure 3.18 (a) and (b), respectively, under different process noise and measurement noise for 100 particles. It is observed from Figure 3.18 (a) that at a very low level of process noise, *RUL* estimation error is high, irrespective of the level of measurement noise. The percentage error in *RUL* estimation is around 8% when the standard deviation (SD) of measurement noise and process noise is less than 0.8 V and within 0.05 V to 0.25 V, respectively. Figure 3.18 (b) shows that *RUL* estimation error can go as low as 13% for SIR PF. Thus, APF performs better than SIR PF under process and

measurement noise. Comparing performance in % error in *RUL* estimation and computation time for Gaussian and exponential PDF family modeling of existing measurement noise is shown in Figure 3.19 (a) and (b), respectively. It is observed from Figure 3.19 (a) and (b) that when the number of samples is greater than 30, the percentage error in *RUL* estimation is comparable. RMS error decreases in line with the increase in the number of particles for both APF and SIR PF. However, APF shows a better performance than SIR PF. RMS error for APF and SIR PF is shown in Figure 3.15 (a) and (b), respectively, when applied in region 1. Thus, the average RMS error for APF drops from 29% to 7% when the number of particles is increased from 10 to 100. However, the variance is further reduced when APF is applied while $V_{CE,ON}$ reaches 5% of the initial value (in region3).

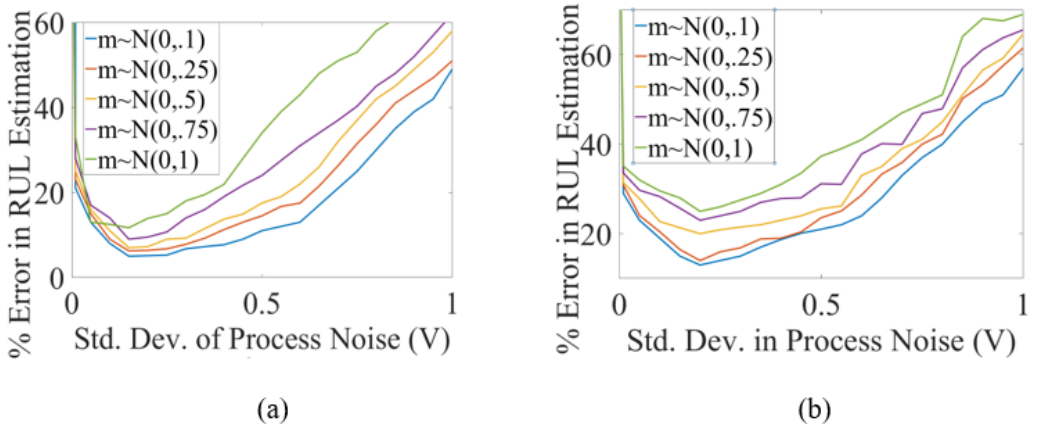

Figure 3.18 (a) Performance of the APF and (b) Performance of SIR under the different process and measurement noise for 100 particles.

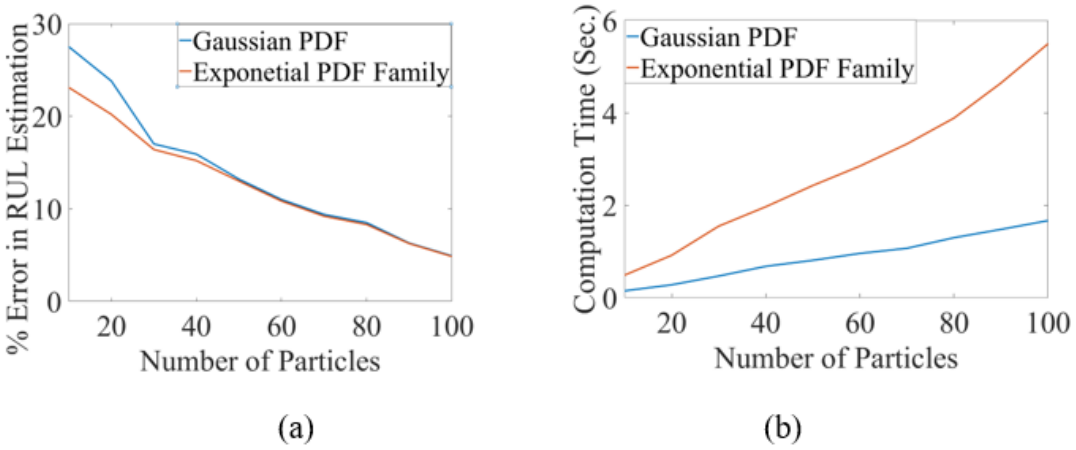

Figure 3.19 Comparison of (a) % error in *RUL* estimation and (b) computation time for Gaussian and non-Gaussian noise in APF based *RUL* estimation.

3.5 Conclusion

This study introduces a high accuracy *RUL* estimation method of IGBT based on APF. It shows that the proposed APF method demonstrates superior performance compared to SIR PF in *RUL* estimation. It indicates that RMS error in *RUL* estimation decreases from 22% to 17.8% when APF is applied. Based on the application of APF, it shows that the trajectory of $V_{CE,ON}$ can be segmented into three regions. Region 1 shows a constant tendency, while region 2 shows a linear increasing tendency. Region 3 depicts the exponential increase of $V_{CE,ON}$. It indicates that *RUL* estimation using the APF method can be significantly improved by applying APF when $V_{CE,ON}$ enters region 3. It also shows that the APF method's performance can be improved up to 80% in *RUL* estimation when applying to region three compared to region 1. With its capability to reduce particles and increase diversity in samples with low computation time, the proposed method can be applicable for accurate *RUL* estimation of other power switches in the industry.

CHAPTER IV

SPARSE KERNEL RIDGE REGRESSION ASSISTED PARTICLE FILTER BASED REMAINING USEFUL LIFE ESTIMATION OF CASCODE GAN FET

The content of this chapter is based on M. Haque and S. Choi, "Sparse Kernel Ridge Regression Assisted Particle Filter based Remaining Useful Life Estimation of Cascode GaN FET," in *IEEE Transactions on Industrial Electronics*, doi: 10.1109/TIE.2020.3000126.

4.1 Introduction

Wide bandgap devices such as cascode GaN FETs are a promising solution for high power, high frequency harsh industrial applications [51]-[53]. However, its reliability has not been thoroughly tested in a modern power electronics system. Power switches in emerging applications are increasingly subjected to dynamic and harsh operations, leading to fast changes in a device's health condition [54]-[55]. The harsh noise environment in the emerging application makes it challenging to accurately identify the condition and make a precise RUL estimation. Existing studies on health monitoring and RUL estimation have addressed these issues in a limited scope. State-of-the-art requires an exhaustive number of samples and system memory to overcome these issues. They also suffer sample impoverishment and particle degeneracy [57]-[59].

Various recursive Bayesian filtering methods (e.g., Kalman Filter (KF), particle filtering (PF)) have been applied for the RUL estimation [59]-[62]. The performance of KF is dependent on the nature of the system and the noises. KF shows a significant variance when the trajectory is nonlinear or the noise is non-Gaussian [59]. Although generic PF offers better performance than

KF methods, it suffers large significant RUL estimation error due to particle-degeneracy and sample impoverishment. APF method introduces the particle index as a new variable to reduce the adversity of sample impoverishment. The APF based RUL estimation method experiences reduced efficiency when the sample size is small, and the process noise is large. The APF method is also highly computationally intensive [63]-[67]. Support vector regression (SVR) PF method utilizes SVR for the sample re-weighting to achieve high robustness against process noise [64]. The prediction speed of SVR is not significant during the updating stage of PF as many samples are required in the prediction step. Also, these PF methods model the trajectory and its change-point locations are based on historical life-testing data. The accuracy of these methods under harsh noise environments depends on the number of samples. Even though those conventional approaches significantly improved RUL estimation, it must be further investigated to be applied under a dynamic change in health conditions. Since a sudden shift in the health condition is critical in industrial applications, change-point location identification is essential for accurate trajectory tracing.

When the operating condition of a system, including ambient temperature, frequency, voltage, current, cooling conditions, etc., changes abruptly, the junction temperature in the FET could experience a significant variation. This junction temperature variation will lead to a substantial change in the switch degradation rate and lifetime. These substantial changes in degradation rate result in new change-point locations different from the change-point location under steady operating conditions. Thus, current RUL estimation methods cannot trace the fault precursor's changed trajectory and result in a significant RUL estimation variation. This sudden change in trajectory is common in industrial applications and results in substantial RUL estimation errors if not addressed. Sparse kernel ridge regression (SKRR) maps the particles into the higher

dimensional feature space to bring significant samples' significant sparsity. The number of kernels in SKRR is not limited by Mercer's condition [66]-[68]. This SKRR method is an effective tool to detect a shift in the change-point locations and trace the changed trajectory with a minimum time lag. As the degradation rate is higher at the end of the lifetime, a higher prediction speed is required to predict accurate RUL and generate the warning signal before the switch fails. The SKRR could increase the prediction speed and accuracy and address the sudden change in the $R_{DS,ON}$ trajectory.

In this study, an improved PF, SKRR-PF, is proposed for the accurate hybrid trajectory tracing and RUL estimation of cascode GaN FET. The proposed method provides robustness to the process and measurement noise, even when the sample size is small under a steady-state or dynamic (abrupt) change in the health condition of the GaN FET. This chapter is logically organized as follows: Section 4.2 discusses the structure and failure mechanisms in cascode GaN FET. Section 1.3 discusses SKRR-PF based RUL estimation. Section 4.3 provides experimental verifications, followed by the conclusion.

4.2 Structure and failure mechanisms of cascode GaN FET

$R_{DS,ON}$ trajectory of cascode GaN FET changes with aging and harsh operation, leading to degradation. The change in the $R_{DS,ON}$ trajectory, is due to unique degradation characteristics of cascode GaN FET which is different from other types of semiconductor power switches. $R_{DS,ON}$ measurement, is challenging due to these unique degradation characteristics of cascode Gan FET, harsh noise, and dynamic operation in real-world applications. A brief discussion on the cascode GaN FET structure is presented in this section to understand its unique degradation mechanisms and RUL estimation challenges.

1.2.6 Structure of cascode GaN FET

Cascode GaN FET combines a simple fabrication process and a higher breakdown voltage of the D-GaN FET with the simple switching circuitry of low voltage Si MOSFET [57]-[58]. The cascaded structure of GaN FET is shown in Figure 4.1 (a) and (b). The internal structure of the GaN high electron mobility transistor (HEMT) is shown in Figure 4.1 (c). A GaN layer is fabricated on a Si substrate with a very thin AiN isolation layer in-between [69]-[71]. When the AlGaN layer is stacked on the GaN layer, the difference in their bandgap results in two infinitely charge-sheets due to spontaneous and piezoelectric polarization effects. These polarization charge sheets create an induced electric field that attracts the electron in the GaN layer and forms a two-dimensional electron gas (2DEG). The velocity of the electrons is dependent on the operating condition of the system, especially voltage and temperature. The abrupt change in operating conditions results in a dynamic change in the velocity of these electrons. Under normal operating conditions, these high-velocity electrons in 2DEG collide with the atoms at the junction surface and create cracks at the junction. 2DEG electrons are trapped in these cracks, which causes the change in on-state resistance [72]-[75]. A sudden unexpected shift in operating conditions causes a change in these electrons' velocity, resulting in an unexpected and abrupt change in the $R_{DS,ON}$ trajectory. If these tendencies are not addressed in the RUL estimation method, it will result in a significant RUL estimation error.

$R_{DS,ON}$ measurement of the cascode GaN FET, is challenging due to the harsh noise and unique $R_{DS,ON}$ characteristics of GaN FET. As there are a few studies on the cascode GaN FET's reliability, their challenges are not addressed from the RUL estimation point. $R_{DS,ON}$ of GaN HEMT is modeled as bias independent series contact resistance and channel resistance, as follows:

$$R_{DS,ON} = R_{se} + \left[\left(L_{SG} + L_G + L_{GD} \right) / \ W_G \right] R_{ch} \tag{4.1}$$

where R_{se} is the series contact resistance, R_{ch} is the contactless channel resistance, L_{SG}, L_G, L_{GD} are the source-gate, gate, and gate-drain length, respectively, and W_G is the gate width. The series contact resistance comprises source contact resistance (R_s) and drain-contact resistance (R_d). Contact resistance does not show significant sensitivity to material degradation. For this reason, (4.1) is written as follows:

$$R_{DS,ON} = R_{se} + \left[\left(L_{SG} + L_G + L_{GD} \right) / \ W_G \right] R_{ch} \tag{4.2}$$

Channel resistance is a function of the current through the channel and depth of the cracks. The electron trapping effect mainly dominates change in this resistance in cascode GaN FET. These trapped electrons result in dynamic $R_{DS,ON}$ during switching of GaN HEMT, as shown in Figure 4.2. $R_{DS,ON}$ is also dependent on the number and depth of cracks formed at the boundary GaN and AlGaN. More electrons are trapped in these cracks at the beginning of on-state, and $R_{DS,ON}$ increases. Then it decreases and converges to its static value. The convergence time depends on the electron de-trapping time constant. Si MOSFET's $R_{DS,ON}$ does not show dynamic characteristics and converges to its static value immediately after switching on [64]. Therefore, dynamic $R_{DS,ON}$ of the cascode GaN FET is due to the structure of GaN HEMT.

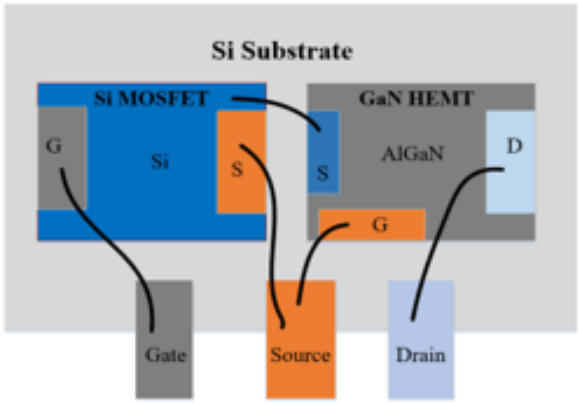

(a)

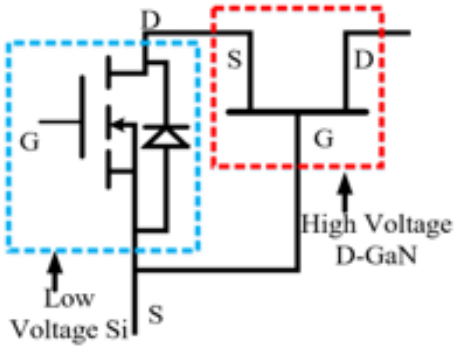

(b)

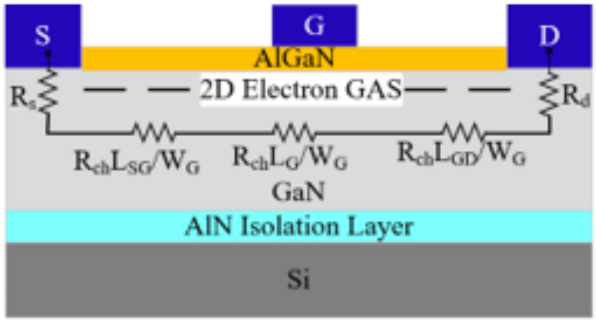

(c)

Figure 4.1 (a) Cascode GaN FET, (b) the symbol of cascode GaN FET and (c) internal structure of GaN HEMT.

If the dynamic nature of the GaN HEMT's dynamic $R_{DS,ON}$ is not addressed, it would result in erroneous RUL estimation. $R_{DS,ON}$ of the cascode GaN FET is measured when dynamic $R_{DS,ON}$ sufficiently converges to its static value to address this challenge.

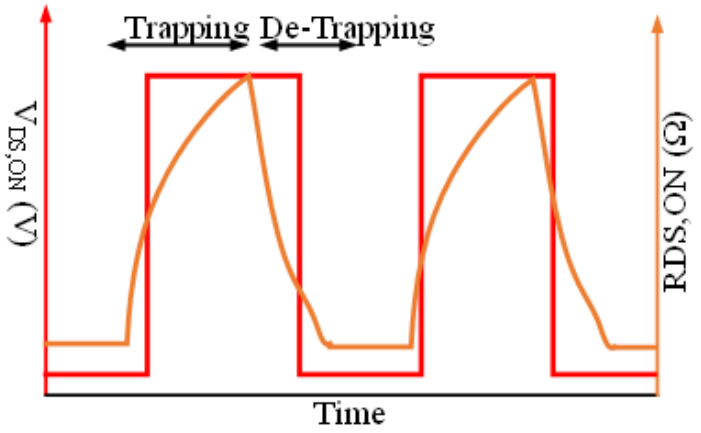

Figure 4.2 On-state resistance of GaN FET.

1.2.7 Failure mechanisms in cascode GaN FET

This study focuses on precisely estimating the RUL of the cascode GaN FET based on the degradation of sensitive $R_{DS,ON}$ trajectory under dynamic system operation. $R_{DS,ON}$ of cascode GaN FET primarily increases with the cracks at the junction of GaN and AlGaN layer, wire-bond connection degradation, and solder fatigue.

During operations, cascode GaN FETs experience thermo-mechanical stresses due to crystal mismatch between Si and GaN FET [74]. This mechanical stress results in solder fatigue, crack propagation, wire-bond cracks, leading to the wire-bond lift-off. Each layer junction and the connection between wire-bond and soldering experience mechanical stress due to the mismatch of

the coefficient of thermal expansion (CTE) between layers. This stress results in cracks and breakdown of the junction and wire bonds. Hot electron and inverse piezoelectric effects are dominant mechanisms as these are highly dependent on the operating condition. When a system's condition changes suddenly, these effects result in a higher rate of degradation, resulting in an abrupt change in the $R_{DS,ON}$ trajectory.

When the operating condition is stable, the degradation path follows the modeled trajectory with a predictable change-point. However, if the operating condition changes unexpectedly, the trajectory of the $R_{DS,ON}$ experiences sudden change from its modeled trajectory. State-of-the-art RUL estimation methods for traditional semiconductor switches do not address this unique characteristic of the cascode GaN FET and sudden changes in the operating condition. Thus, they are not effective for the RUL estimation of the cascode GaN FET. The proposed SKRR-PF method utilizes the customized $R_{DS,ON}$ measurement technique and hybridizes SKRR and PF's benefits to detect the unknown change-points when the operating condition changes fast for efficient RUL estimation.

1.3 Sparse kernel ridge regression assisted particle filter based remaining useful life estimation

State-of-the-art RUL estimation methods have statistically modeled the $R_{DS,ON}$ trajectories based on the historical accelerated life testing data of the cascode GaN FET. Although these methods can trace the nonlinear trajectory, their ability to trace a trajectory under the dynamic operating condition is limited. The proposed SKRR PF-based RUL method shows the ability to trace the nonlinear fault precursor trajectory under steady and dynamic conditions. $R_{DS,ON}$ trajectory of cascode GaN FET, shows a nonlinear trajectory over its life. The proposed RUL estimation

method introduces an improved variation of PF for trajectory tracking and projection. This PF method utilizes a fast and low computational SKRR based resampling method to overcome the sample impoverishment and particle-degeneracy problems of the generic PF method. In this section, SKRR-PF based RUL estimation of cascode GaN FET is described as follows:

1.3.1 State-space model

The degradation of cascode GaN FET increases $R_{DS,ON}$. The evolution of $R_{DS,ON}$ to time is modeled as follows:

$$R_{ds,on}(t) = R_0 \exp(bt^2 + ct + d) \tag{4.3}$$

The discrete form of (4.3) is as follows:

$$R_{ds,on}(k) = R_{ds,on}(k-1) + [a(k)\exp(\Delta k^2 b(k) + kc(k) + d)]\Delta k + w_1(k) \tag{4.4}$$

where

$$a(k) = [b(k)\Delta k + c(k)]R(k-1) + w_2(k) \tag{4.5}$$

$$b(k) = b(k-1) + w_3(k) \tag{4.6}$$

$$c(k) = c(k-1) + w_4(k) \tag{4.7}$$

(4.4)-(4.7) are the state transition equations of the system. $R_{DS,ON}(k)$, $a(k)$,$b(k)$, and $c(k)$ are the state variables, Δk is the acquisition time difference between two samples and $w_1(k)$, $w_2(k)$, $w_3(k)$ and $w_4(k)$ are the process noises of (4.4)-(4.7), respectively. $w_1(k)$, $w_2(k)$, $w_3(k)$ and $w_4(k)$ are defined as $N(0,\sigma_1^2)$, $N(0,\sigma_2^2)$, $N(0,\sigma_3^2)$, and $N(0,\sigma_4^2)$, respectively where σ_i is the standard deviation of the i^{th} process noise. The measurement equation is as follows:

$$y(k) = R_{ds,on}(k) + m(k) \tag{4.8}$$

where $y(k)$ is the measured $R_{DS,ON,}$ and $m(k)$ is the associated measurement noise. The state and measurement equations are stochastic processes due to the presence of noises. The recursive Bayesian estimation methods, such as Kalman filter, PF methods, are widely used to estimate stochastic systems. Kalman filter is suitable for the linear system and Gaussian noise. PF methods show better performance for non-linear systems and Gaussian/non-Gaussian noises. In the following section, the fundamental of Generic PF method is explained.

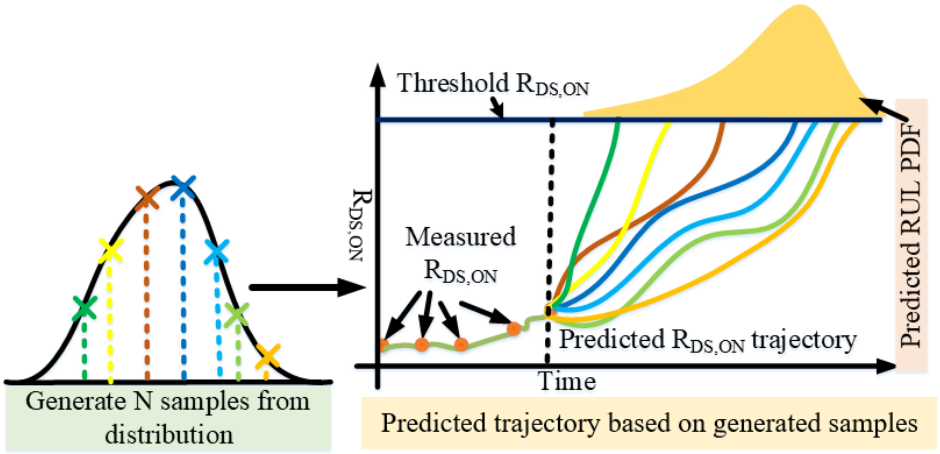

Figure 4.3 Fundamental of Monte Carlo Simulation in RUL estimation.

1.3.2 Generic particle filtering method

Generic PFs utilize the Bayesian recursive filtering (BRF) framework based on the Monte Carlo simulation. The principle of Monte Carlo Simulation is shown in Figure 4.3. PF RUL estimation works in two steps: prediction and update [62]-[63]. In the prediction step, $R_{DS,ON}(k)$ is estimated using state equations. In the update step, this $R_{DS,ON}(k)$ are corrected and updated based on measured $y(k)$. The objective of the PF method is to find out the posterior PDF, $p(R_{DS,ON}(k)|y(1{:}k))$ based on state transition PDF $p(R_{DS,ON}(k)|\ R_{DS,ON}(k\text{-}1))$ and prior PDF, $p(R_{DS,ON}(k)|y(1{:}k\text{-}1))$. At k=0, the posterior distribution is as follows:

$$p\left(R_{DS,ON}(0)\,|\,y(0)\right) = p(R_{DS,ON}(0)) \tag{4.9}$$

where $p(R_{DS,ON}(0))$ is the $R_{DS,ON}$ PDF before accelerated testing. $R_{DS,ON}(k)$ is predicted based on the previous measurement using the Chapman-Kolmogorov equation as follows:

$$p\left(R_{DS,ON}(k)\,|\,y(1:k-1)\right)= \int[\,p\left(R_{DS,ON}(k)\middle|R_{DS,ON}(k-1)\right)\mathrm{p}\left(R_{DS,ON}(k-1)\middle|y(1:k-1)\right)dR_{DS,ON}(k-1)] \tag{4.10}$$

According to Bayes rule, posterior PDF is updated as follows:

$$p\left(R_{DS,ON}(k)\,|\,y(1:k)\right)=\frac{p\left(y(k)\,|\,R_{DS,ON}(k)\right)p\left(R_{DS,ON}(k)\,|\,y(1:k-1)\right)}{p\left(y(k)\,|\,y(k-1)\right)} \tag{4.11}$$

where $p(y(k)|R_{DS,ON}(k))$ is the likelihood function and $p(y(k)|y(k\text{-}1))$ is the normalizing constant. For a linear system and Gaussian white noise, KF traces the system if it has an analytical form (4.11). KF shows large variance when the system is nonlinear with noise, as in this case, (4.11) does not have an analytical form. Particle filters utilize the Monte Carlo-based numerical integration method for the solution of (4.11) to trace non-linear trajectories with non-Gaussian noise. In generic PF, posterior PDF is modeled as the product of random samples and associated weights as follows:

$$p\left(R_{DS,ON}(k)\,|\,y(1:k)\right)\approx\sum_{i=1}^{N}w^{i}(k)\delta\left(R_{DS,ON}(k)-R^{i}_{DS,ON}(k)\right) \tag{4.12}$$

where $\delta(\cdot)$ is the Dirac-Delta Function, $w^i(k)$ is the ith sample's weight. In generic PF, the weight of a particle is estimated using importance sampling as follows:

$$w^{i}_{n}\propto\frac{p\left(R^{i}_{DS,ON}(k)\,|\,y(k)\right)}{q\left(R^{i}_{DS,ON}(k)\,|\,y(k)\right)} \tag{4.13}$$

where $q(R_{DS,ON}^{i}(k)|y(k))$ is the importance PDF. The importance sampling draws random samples from the high-density region of the PDF. These weights are estimated recursively as follows:

$$w(k) \propto [w(k-1)\frac{p(y(k)\,|\,R_{DS,ON}(k))\,p(R_{DS,ON}(k)\,|\,R_{DS,ON}(k-1))}{q(R_{DS,ON}(k)\,|\,R_{DS,ON}(k-1))}] \tag{4.14}$$

The generic PF method suffers from significant sample degeneracy due to a significant mismatch of the shape of $p(\cdot)$ and $q(\cdot)$ in (4.14). This mismatch results in low-weight samples and wasted computational power. Moreover, this generic PF method shows a significant variation in RUL estimation. Also, it shows a prolonged response to the abrupt change in operating conditions as generic PF cannot detect the change-point inherently when there is a sudden change in trajectory. The resampling is introduced in the PF method to overcome the sample degeneracy problem. The resampling step is conducted to reduce the computational burden when the number of particles reduces below the effective number of particles (N_{eff}). The particles with higher weights are duplicated, and the particles with lower weights are discarded in this step. As a result, all the particles are originated from the high-density region and create a sample impoverishment problem. The particle's index is used as an additional variable to address the drawbacks of PF. This additional variable increases the particles' dimensionality and avoids sample impoverishment [65]-[68]. This additional information on the sample increases the tracing accuracy of the particle under stable operating conditions. However, their performance has not been validated under dynamic operating conditions. In this study, a PF method is proposed using SKRR based prior PDF construction for RUL estimation of cascode GaN FET. SKRR provides an analytical form of the posterior PDF and improves the speed and efficiency of the RUL estimation method compared to standard PF methods. Moreover, the inherent change-point detection property of SKRR enables

this system to address the abrupt change in operating conditions and the associated change in trajectory.

1.3.3 Sparse kernel ridge regression-based resampling

Multi-collinearity causes a significant variation in RUL estimation in the Generic PF. KRR method reduces the variance by trading off bias [76]-[29]. It also utilizes the geometric method for the modeling of the PDF. The posterior PDF is modeled as the linear mixture of the kernel functions as follows:

$$f\left(R_{DS,ON}(k)\right) = p\left(R_{DS,ON}(k) \mid y(k)\right) \approx \sum_{i=1}^{N} \alpha^{i}(k) K^{i}\left(y_i, R_{DS,ON}^{i}(k)\right) \tag{4.15}$$

where $K(\cdot)$ is the kernel function, and α is the i^{th} kernel's weight. The estimation of weights is subject to the cost function, L as follows:

$$L = \boldsymbol{\alpha}^{\mathbf{T}}(\mathbf{K}^{\mathbf{T}}\mathbf{K}+\lambda\mathbf{I})\boldsymbol{\alpha}-2\boldsymbol{\alpha}^{\mathbf{T}}\mathbf{K}^{\mathbf{T}}\mathbf{y} \tag{4.16}$$

$$\hat{\boldsymbol{\alpha}} = \arg\min \mathrm{L} \tag{4.17}$$

where $\boldsymbol{\alpha}$ is the estimated weight and λ is the Lagrange multiplier,

$$\begin{aligned} \mathbf{K} &= \begin{bmatrix} K_1 & K_2 & . & . & . & K_N \end{bmatrix}^T, \\ \boldsymbol{\alpha} &= \begin{bmatrix} \alpha^1 & \alpha^2 & . & . & . & \alpha^N \end{bmatrix}^T \\ \mathbf{y} &= \begin{bmatrix} y_1 & y_2 & . & . & . & y_N \end{bmatrix}^T \end{aligned} \tag{4.18}$$

Based on (4.16) and (4.17), weights are estimated as follows:

$$\hat{\boldsymbol{\alpha}}=[\mathbf{K}^{\mathbf{T}}\mathbf{K}+\lambda\mathbf{I}]^{-1}\mathbf{K}^{\mathbf{T}}\mathbf{y} \tag{4.19}$$

In the KRR method, all the data points are used in the posterior PDF construction, requiring large storage and processing power [78]-[79]. The fitting speed is improved by introducing sparseness in KRR using the backward deletion method used in [76]-[80]. In the backward deletion (BD) SKRR method, sparseness in posterior PDF is created by considering only significant leave-one-out-scored measured $R_{DS,ON}$. This algorithm reduces **K, α,** and **I** after each iteration meeting the required constraint. If the size of the data set is *Px1* and m^{th} sample is deleted at j^{th} iteration, (4.15) is written as follows:

$$f_{j,m} = -(\mathbf{K}_{\mathbf{j,\{P\}-m}}{}^{\mathbf{T}}\mathbf{y}_{\mathbf{j,\{P\}-m}})^{\mathbf{T}}(\mathbf{K}_{\mathbf{j,\{P\}-m}}{}^{\mathbf{T}}\mathbf{K}_{\mathbf{j,\{P\}-m}}+\boldsymbol{\lambda}\mathbf{I}_{\mathbf{j,\{P\}-m}})^{-1}(\mathbf{K}_{\mathbf{j,\{P\}-m}}{}^{\mathbf{T}}\mathbf{y}_{\mathbf{j,\{P\}-m}}) \tag{4.20}$$

where $f_{j,m}$ is the value of (4.15) at j^{th} iteration when m^{th} sample is taken out. The leave-one-out (LOO) score of m^{th} sample out, $\Delta f_{j,m}$ is estimated as follows:

$$\Delta f_{j,m} = f_{j,m} - f_j \tag{4.21}$$

where f_j is evaluated with all the remaining $R_{DS,ON}$ points dataset after $(j\text{-}1)^{\text{th}}$ iteration. The lowest LOO-scored $R_{DS,ON}$ is removed from the dataset after the j^{th} iteration. This BD process terminates when the following condition is met as follows:

$$\Delta f_j \geq \varepsilon \,|\, L_{\min,j} \,|$$ (4.22)

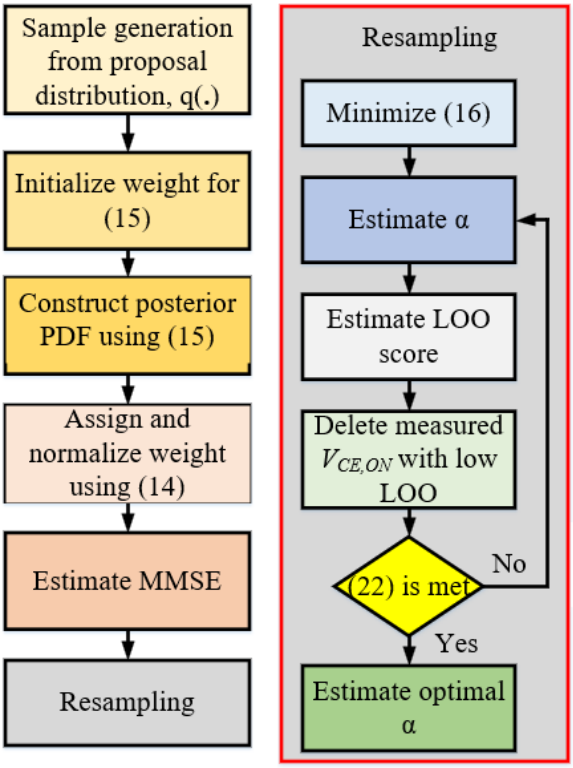

Figure 4.4 The working principle of SKRR particle filter.

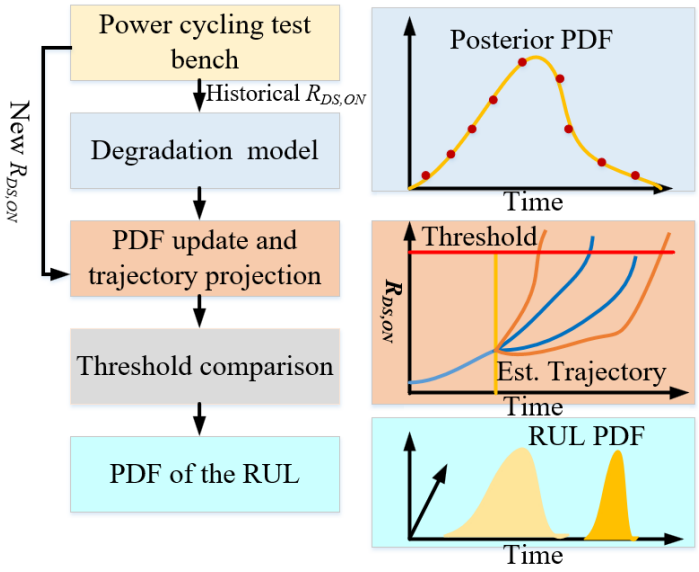

Figure 4.5 SKRR-PF based RUL estimation process.

This process results in an optimum size of **K, α,** and **I** for posterior PDF construction. For these optimized **K, α,** and **I**, Equation (4.18) is written as follows:

$$\hat{\boldsymbol{\alpha}}_{\mathbf{opt}}=[\mathbf{K}_{\mathbf{opt}}{}^{\mathbf{T}}\mathbf{K}_{\mathbf{opt}}+\lambda\mathbf{I}_{\mathbf{opt}}]^{-1}\mathbf{K}_{\mathbf{opt}}{}^{\mathbf{T}}\mathbf{y}_{\mathbf{opt}} \tag{4.23}$$

where $\boldsymbol{\alpha}_{\mathbf{opt}}$, $\mathbf{K}_{\mathbf{opt}}$, $\mathbf{I}_{\mathbf{opt}}$ are the optimized size of **K, α** and **I** subject the constraint (4.21). The posterior PDF is written as follows:

$$p(R_{DS,ON}(k)\,|\,y(k))=\sum_{i=1}^{p}w^{i}(k)\alpha_{i}K(R_{DS,ON},R_{DS,ON}^{i}) \tag{4.24}$$

The working principle of SKRR is shown in Figure 4.4.

1.3.4 Abrupt change-point detection

When the system's operating condition abruptly changes, the change-point locations in $R_{DS,ON}$ trajectory shifted from their estimated positions. However, SKRR-PF has the inherent ability to identify this abrupt change in change-point location [72]. In SKRR, the kernel function maps time series $R_{DS,ON}$ to the Hilbert space as follows:

$$\left\langle \phi\left(R_{DS,ON}(k)\right), \phi\left(R^{i}_{DS,ON}(k)\right)\right\rangle = K^{i}\left(R_{DS,ON}(k), R^{i}_{DS,ON}(k)\right) \tag{4.25}$$

where $\varphi(\cdot)$ is the canonical feature map defined as $\varphi: R_{DS,ON} \rightarrow H$ where H is the Hilbert space. In the time series, the change-point detection requires the whole distribution statics, wherein Hilbert space, the change-point is detected only using the mean of the Hilbert elements. In Hilbert space, an element is defined as follows:

$$\phi\left(R^{i}{}_{DS,ON}(k)\right) = \mu_i + e_t \tag{4.26}$$

where μ_i is the mean of the distribution in Hilbert space and e is the transformation noise. If there is a sudden change in trajectory, the Hilbert mean of $R_{DS,ON}$ changes as follows:

$$\mu_i \neq \mu_j \tag{4.27}$$

This property is helpful for the detection of the known change-points and the identification of the unknown change-points. Thus, the proposed hybrid RUL estimation method detects any sudden change in the trajectory of $R_{DS,ON,}$ which is crucial for accurate RUL estimation under dynamic operating conditions.

1.3.5 Remaining useful life estimation

SKRR-PF method traces the trajectory of $R_{DS,ON}$-based on (4.8) and projected the trajectory as shown in Figure 4.5. The cascode GaN FET is assumed faulty when the $R_{DS,ON}$ trajectory reaches the threshold value. In this study, the threshold is chosen as the 10% increase of $R_{DS,ON}$ from its initial value. There is no guideline on the wideband gap device's remaining useful life estimation. Thus, common semiconductor device RUL estimation guideline is followed for threshold based on IEC 60747-9-2007. RUL is estimated as follows:

$$RUL_n = n_f - n \tag{4.28}$$

where RUL_n is the RUL estimated at time n, n_f is the time to reach the critical value of the fault precursor from the present time n. RUL is estimated for each sample of state variable PDF, and the PDF of RUL is estimated.

4.3 Experimental validation

The objective of the experimental verification for this proposed RUL estimation method is to validate its robustness and accuracy under the steady operating condition and dynamic operating conditions. Aging and degradation mechanisms of cascode GaN FET are the result of junction temperature variation induced thermo-mechanical stress. Thus, constant current power cycling tests are implemented in this study for inducing accelerated aging in cascode GaN FET under steady and dynamic operating conditions. This accelerated test aims to emulate the thermal stress

experienced by the cascode GaN FET during its operation. A description of the experimental set-up is provided in the following sections, followed by verifying the proposed algorithms based on the accelerated aging data from experimental results.

1.3.6 Experimental set-up

Constant current-temperature variation power-cycling testing set up is shown in Figure 4.6. The device under test (DUT) is an N-Channel 900V/9A TO-220-3 GaN FET. The tests are conducted at 50 V 5 A. The case temperature (T_C) of the FET can vary from 25^{o}C to 100^{o}C for the steady operating condition. As the junction temperature variation remained constant under steady operating conditions, the $R_{DS,ON}$ trajectory follows the modeled trajectory.

T_C is measured with a K-type thermocouple, and the output of the thermocouple is conditioned with MAX31855. TI DSP F28335 controls this power cycling test based on variation in T_C. The temperature cycling is controlled using hysteresis control which controls the turn-on and turn-off of the cascode GaN FET between 25^{o}C and 100^{o}C. Thus, the switching frequency of the DUT is the same as the frequency of its temperature variation. Due to dynamic $R_{DS,ON}$ of cascode GaN FET, proper care should be taken during the data acquisition stage. Thus, RUL estimation's challenge using an accelerated life testing platform is high-precision fault precursor data acquisition.

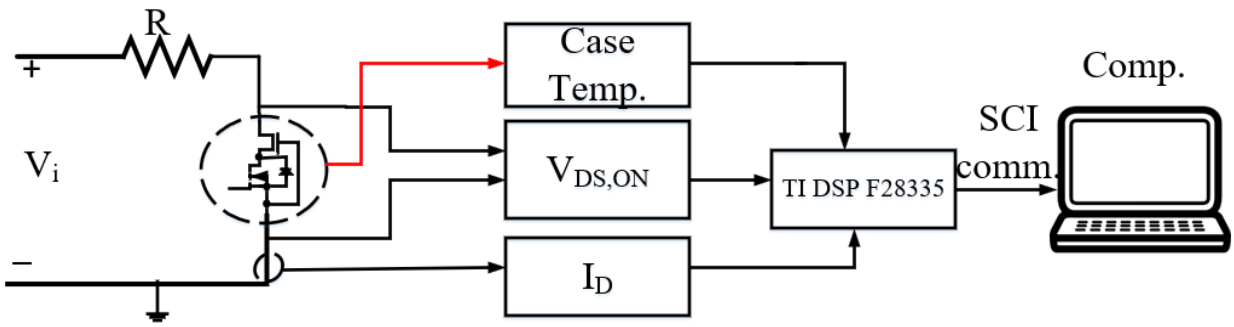

Figure 4.6 Block diagram of power cycling test.

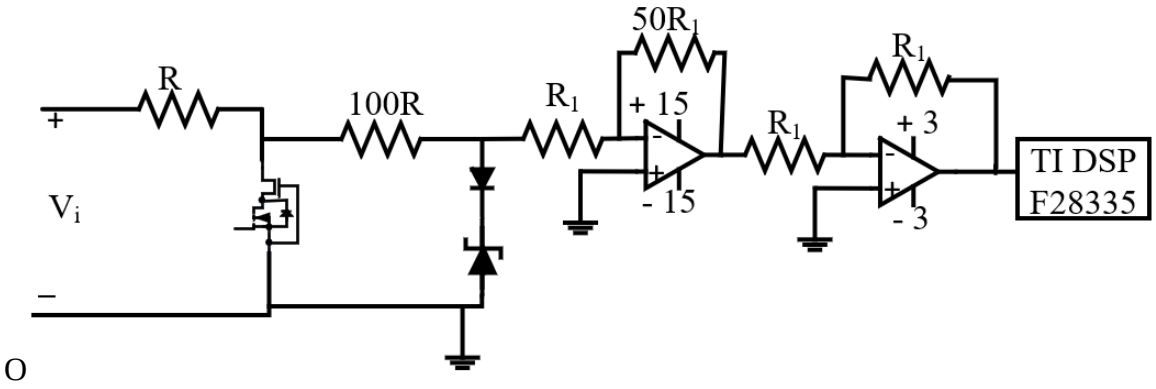

Figure 4.7 $V_{DS,ON}$ sensing circuit.

4.3.1.2 $R_{DS,ON}$ measurement set-up

A $V_{DS,ON}$ measurement, and conditioning setup is shown in Figure 4.7. This setup's objective is to acquire $R_{DS,ON}$ with proper resolution while ensuring safety. The TI DSP F28335 has a 12-bit ADC, which has a resolution of 0.7mV/bit. When the GaN FET is turned off, the drain to source voltage ($V_{DS,OFF}$) across DUT reaches 50 V, damaging the ADCs. During on-state, $V_{DS,ON}$ is in the millivolt range, which is very insignificant compared to $V_{DS,OFF}$. For this reason, $V_{DS,OFF}$ should be scaled while amplifying $V_{DS,ON}$ at the same time. A signal-condition circuit is used to

address these issues, as shown in Figure 4.7, where R is the load resistance and R_1 is the scaling resistance. When the DUT is off, $V_{DS,OFF}$ is limited by the voltage drop across the diode (D_1) and Zener diode (D_{Z1}). When DUT is on, D_1 and D_{Z1} will be open, and $V_{DS,\ ON}$ appears across these switches. These voltages are amplified and limited by two amplifier stages. The ADC's maximum voltage is limited to 3 V. Drain current is sensed by a shunt resistor and transmitted to the computer using the serial communication interface for data processing and storage.

If proper care is not taken, $R_{DS,ON}$ includes both dynamic $R_{DS,ON,}$ and the effect of aging. Data acquisition starts after 100μs after the DUT is turned on to allow the FET to converge to its static value. Moreover, $R_{DS,ON}$ is measured at the same temperature to nullify the effect of temperature on $R_{DS,ON}$.

1.3.7 Experimental results

A power cycling test has been conducted on 30 GaN FETs until the switches failed. Twenty-four of the tested GaN FETs have been used for training, and 6 GaN FETs have been used for the verification. $V_{DS,ON,}$ and I_D are acquired in 10 minutes intervals, and $R_{DS,ON}$ is measured. These data acquisition points are called epoch (1 epoch= 10 min.). The GaN FET is considered faulty when $R_{DS,ON}$-change reaches 10% of its initial value. To have consistency, datasheet value

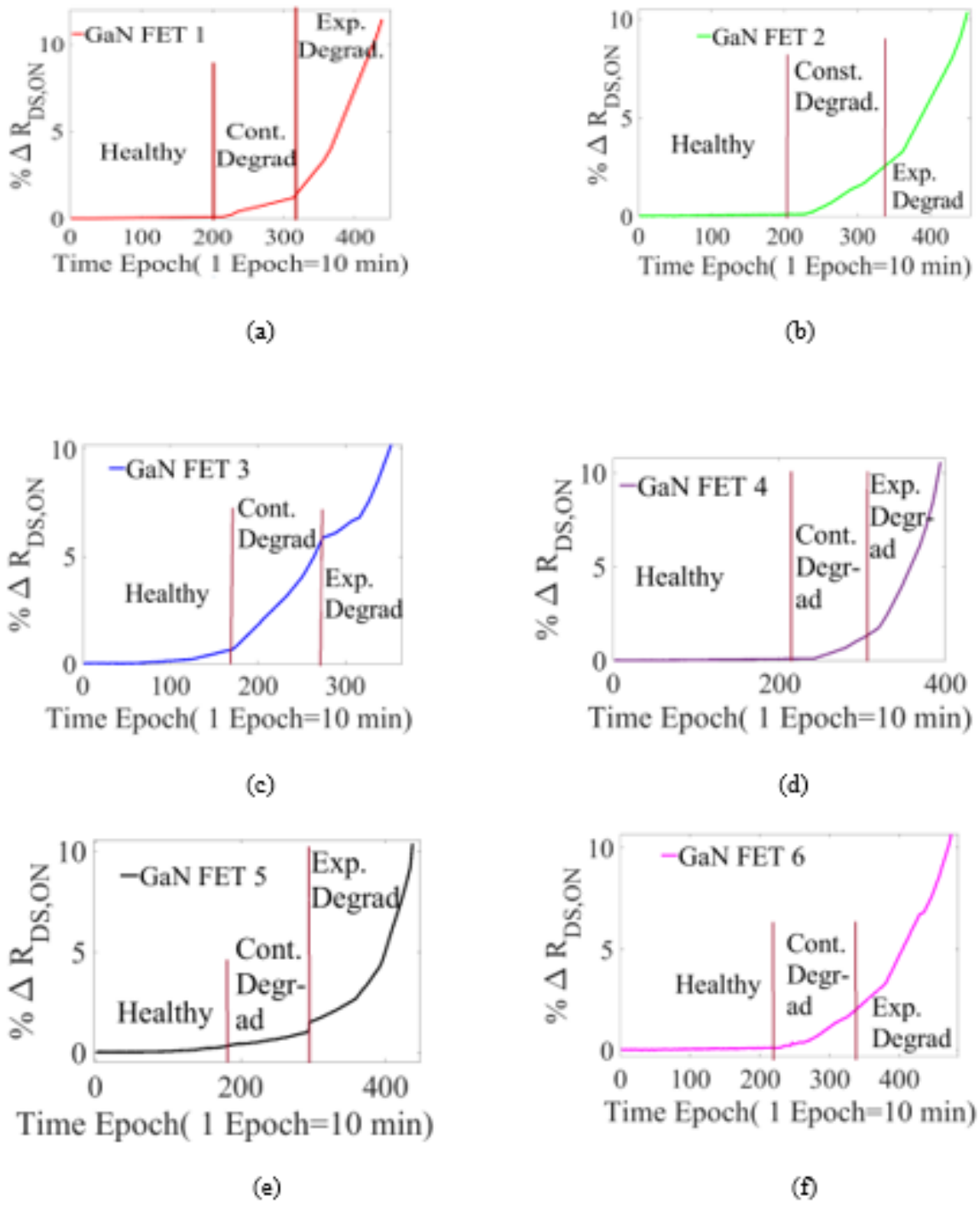

Figure 4.8 Actual trajectory of $R_{DS,ON}$ (a) GaN FET1;(b) GaN FET2; (c) GaN FET3; (d) GaN FET4; (e) GaN FET5; (6) GaN FET6.

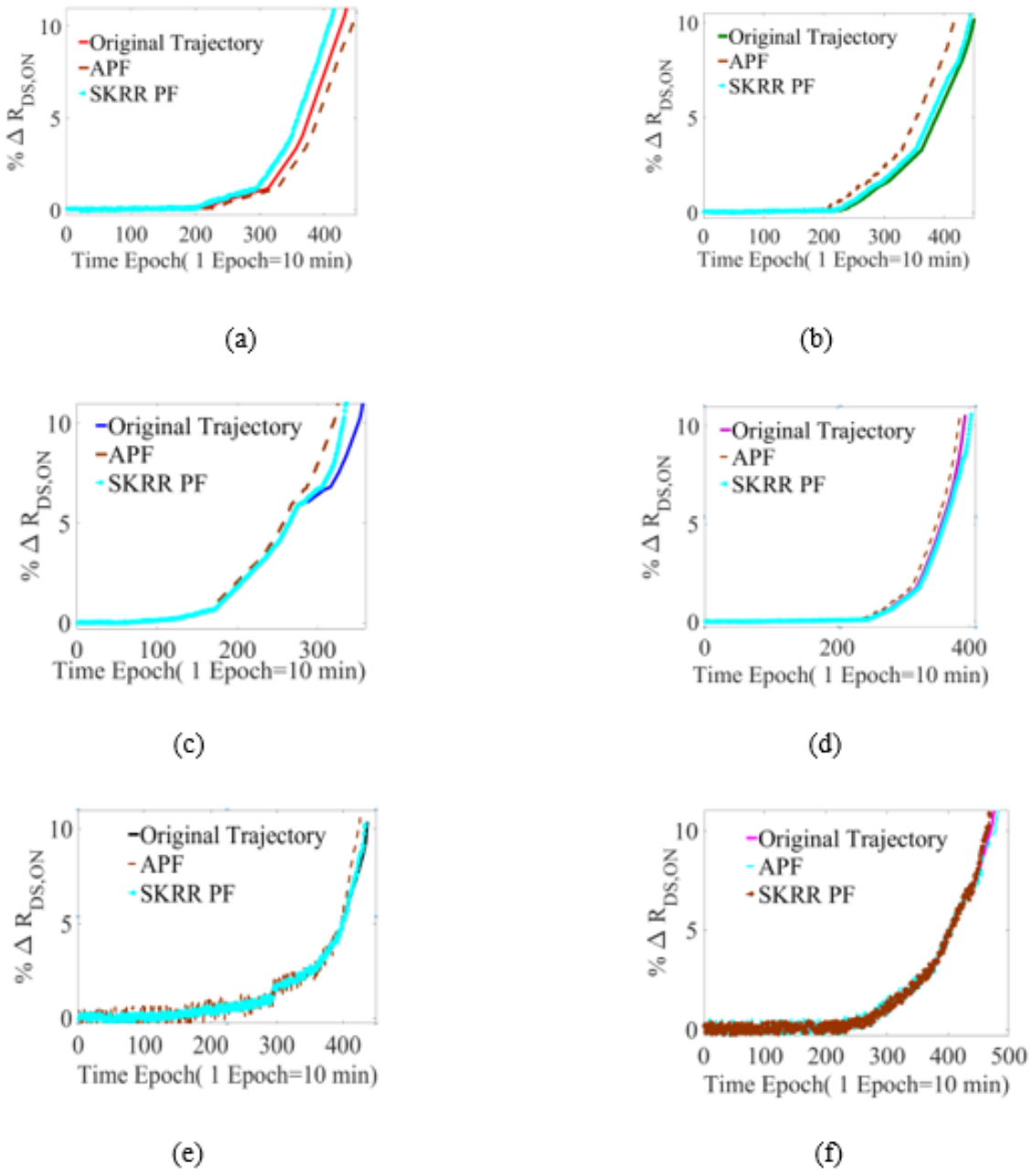

Figure 4.9 The actual trajectory of $R_{DS,ON,}$ and estimated trajectory using APF and SKRR-PF of (a) GaN FET1;(b) GaN FET2; (c) GaN FET3; (d) GaN FET4; (e) GaN FET5; (6) GaN FET6.

Table 1.1 The RUL estimation performance comparison between SKRR-PF and APF

Cascode GaN FET #	SKRR	APF
1	7.7%	8.9%
2	6.3%	7.1%
3	8.1%	15.7%
4	6.3%	9.8%
5	7.9%	13.6%
6	5.8%	7.9%

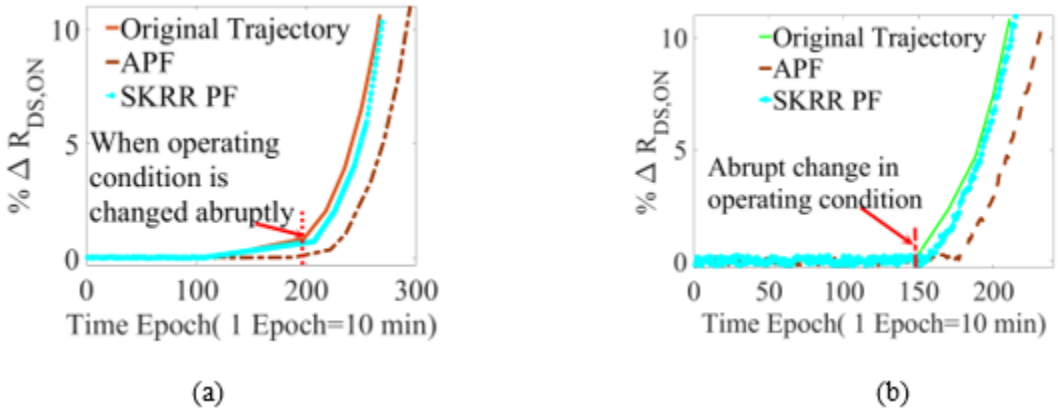

Figure 4.10 Original Trajectory, the estimated trajectory of APF and SKRR PF when (a)ΔT_j is increased by 5°C; (b) ΔT_j is increased by 10°C.

of $R_{DS,ON}$ is considered as an initial value for all the DUTs. $R_{DS,ON}$ trajectories of six cascode GaN FETs are shown in Figure 4.8. under the afore-mentioned operating condition. These trajectories

show three stages of degradation during the life of cascode GaN FET. In the healthy state, $R_{DS,ON}$ remains almost constant (almost till 200 epochs). After that, GaN FET shows the first sign of degradation, and $R_{DS,ON}$ changes constantly. This tendency is observed around 200 to 300 epochs in general. This stage is called the continuous degradation stage. At the end of its lifetime, $R_{DS,ON}$ changes exponentially, and thus, this stage is called the exponential degradation stage. In the experiments, the exponential trajectory is observed after 300 epochs.

The SKRR-PF estimated $R_{DS,ON}$ trajectories, APF estimated trajectories, and original trajectories are shown in Figure 4.9. In this case, the operating condition remained the same as the operating condition of the training set. A comparison of the estimation performance of the proposed SKRR-PF and APF methods is shown in Table 1. The SKRR-PF and APF trajectories are compared with the original trajectory of the DUTs. The estimation error is between 6% to 8% for SKRR-PF, and for APF, it is between 7%-15%. The incorporation of the SKRR in the PF framework improves the accuracy of the RUL estimation.

A 5^{o}C increases junction temperature variation to verify the proposed RUL estimation method's traceability under the unexpected change in operating conditions, as shown in Figure 4.10 (a) at 200 epochs. As a result, the trajectory has experienced a sudden change-point. The proposed method shows the capability to trace the trajectory despite this sudden change. The estimation error is 6% for SKRR-PF and 15% for APF based RUL estimation method. A more harsh condition is applied where the junction temperature variation is increased by 10^{o}C, as

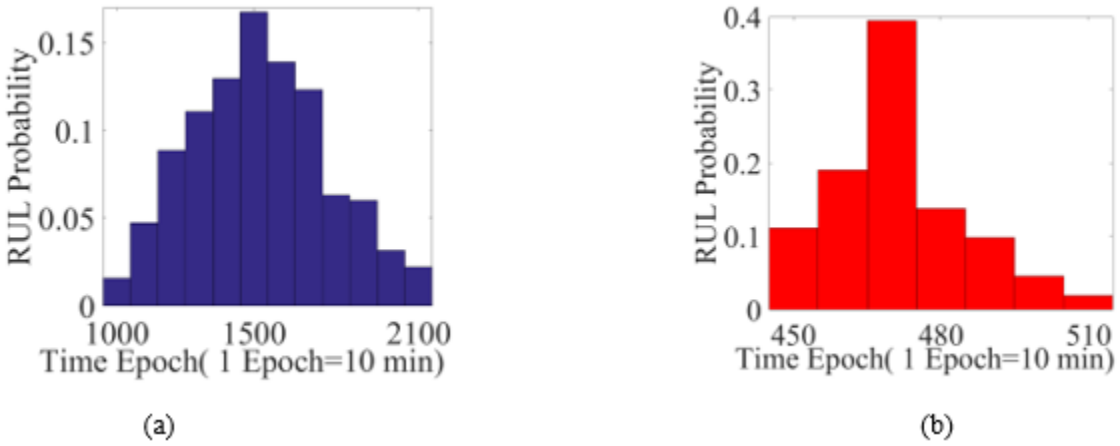

Figure 4.11 SKRR PF estimated RUL PDFs when (a) DUT is in the second stage (b) DUT is in the third stage of its life

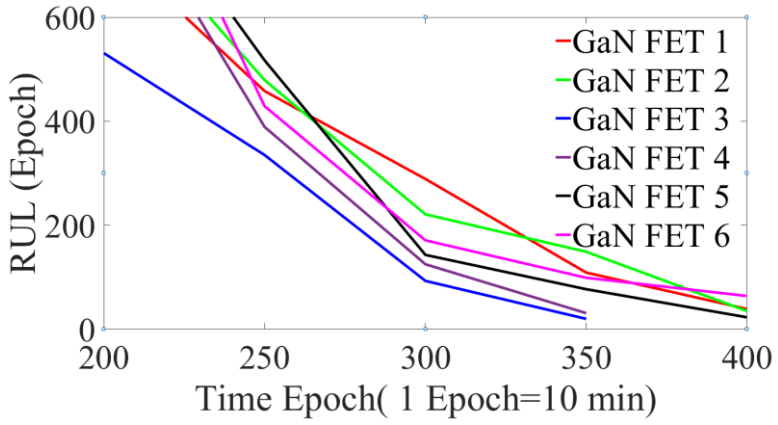

Figure 4.12 Estimated RUL of GaN FET using SKRR-PF.

shown in Figure 4.10 (b). In this case, the RUL estimation errors are 8% and 17% for SKRR-PF and APF based RUL estimation methods, respectively. The percentage error is reduced by more than 112.5% using SKRR-PF over APF in RUL estimation under dynamic operating conditions.

The SKRR-PF estimated RUL PDFs are shown in Figure 4.11. Figure 4.11 (a) shows that the RUL PDF is estimated when the DUT is in its life's continuous degradation stage. The estimated RUL PDF in Figure 4.11(b) is estimated when the DUT is in the exponential degradation stage. It is evident from Figure 4.11 is that the standard deviation of the RUL estimation is significantly reduced in the later stage of its life. The evaluation of the RUL estimation over time is shown in Figure 4.12. In the healthy stage, the estimated RUL is high as $R_{DS,ON}$ changes very slowly. Thus, RUL is plotted after 200 epochs to emphasize the effect of the switch's lifetime degradation.

4.4 Conclusion

This study presented an SKRR-PF based RUL estimation method for cascode GaN FET. It has been shown that high accuracy can be achieved in the RUL estimation under dynamic and harsh operating conditions, even when the health status of the cascode GaN FET changes abruptly. It is also theoretically shown that the proposed method includes the unique characteristic of cascode GaN FET in measurement, improves speed and accuracy of the RUL estimation, and reduces the effect of harsh system noise by include in the SKRR PF framework. In the experimental result, the proposed SKRR-PF shows significantly reduced error down to 6%-8%. In contrast, APF shows a 7%-15% tracing error under steady operating conditions. SKRR-PF and APF show 6%-8% and 15%-17% error estimation, respectively, under the dynamic operating condition with high accuracy under dynamic and harsh industrial conditions. The proposed method could be a promising solution for the system-level RUL estimation for cascode GaN FET in the emerging power electronics system.

CHAPTER V

DATA-SHEET BASED LOSS MODELING AND REALTIME DEGRADATION-AWARE CONTROL OF SOLID-STATE TRANSFORMER

The content of this chapter is based on the following articles:

1. M. S. Haque and S. Choi, "Realtime Degradation-Aware Adaptive Control of Solid State Transformer," *2020 IEEE Applied Power Electronics Conference and Exposition (APEC)*, New Orleans, LA, USA, 2020, pp. 2376-2383, doi: 10.1109/APEC39645.2020.9124174.
2. M. S. Haque and S. Choi, "Data-sheet based loss modeling and Realtime Degradation-Aware Control of Solid State Transformer," Submitted in *IEEE Transactions on Industrial Electronics.*

5.1 Introduction

The solid-state transformer will replace the traditional passive transformers in the modern industry, including electric-vehicle charging and smart-grid applications with low cost, high efficiency (> 99%), and compact features. However, the power switches in the SST commonly experience high frequency (HF) electro-thermal stresses during dynamic operations. These semiconductor switches are among the most vulnerable components in a power electronic system (PES) 0. Thus, the SST's reliability due to the aging and degradation of power switches and proactive degradation-aware control strategy must be further studied for real-world applications [82]-[83].

The SST commonly consists of the cascaded elements, including low-frequency rectifier, HF dual active bridge (DAB), and non-isolated converters, as shown in Figure 5.1. The DAB switches especially experience HF electro-thermal stress and thus, become susceptible to degradation and failures. State-of-the-art performs a fault-tolerant operation after a switch has failed because of the switch degradation's limited understanding. Therefore, costly hardware redundancies are adopted with additional system complexity [84]-[87]. Such redundancies commonly increase the size and weight [86]-[87]. For example, redundancy-based network-level power-routing is not feasible in EV charging applications, where SST is used as a standalone system. In [88]-[92], topology transformation methods are adopted to mitigate the effect of a switch failure. These fault-tolerant methods double the current through the switch, resulting in higher switch stress and accelerated aging. Also, topology transformations need computationally exhaustive fault detection and isolation procedures. In [93]-[94], an adaptive but complicated, costly cooling method for junction temperature control to achieve life extension has been proposed.

Recently, new control strategies such as (i) single-phase shift (SPS), (ii) double phase-shift (DPS), (iii) extended phase-shift (EPS), and (iv) triple phase-shift (TPS) have been suggested to minimize inductor current in the DAB to achieve zero voltage switching (ZVS) [90]-[93]. These methods are promising but have performed adaptive controls without evaluating a switch degradation [85]. Until now, the SST control strategy by understanding the switch degradation has been limitedly studied. If successful, it could offer a new and effective solution without costly redundancies [93]. A system could integrate the switch’s degradation status into a controller to intelligently identify its optimal operating point.

To achieve effective degradation-aware control, fast and accurate switch-loss estimation and health monitoring are essential. Traditional cascode GaN FET loss models are computationally intensive and challenging to implement in a real-time system [92],[94]. These models also require proprietary switch information, which is commonly unavailable in public.

In this dissertation, a new degradation-aware controller is proposed for a cascode GaN FET SST. The proposed controller - 1) ensures the safe and robust operation over SST's lifetime, and 2) operates at optimal power, based on the switch-health status. The degraded switch consumes lifetime accelerated if the SST continues operating at the rated conditions. To address this issue, the proposed controller estimates the optimal derated operating point based on switch-health status. This intelligent derating allows the SST to reach its target lifetime and avoid an unexpected shutdown. Also, to ensure the system's stability and robustness to system disturbance, the proposed controller estimates an optimal phase shift. A data-sheet- and double pulse test-based behavioral switch-loss model is used to identify switch degradation instantaneously with low complexity, enabling real-time and adaptive operation.

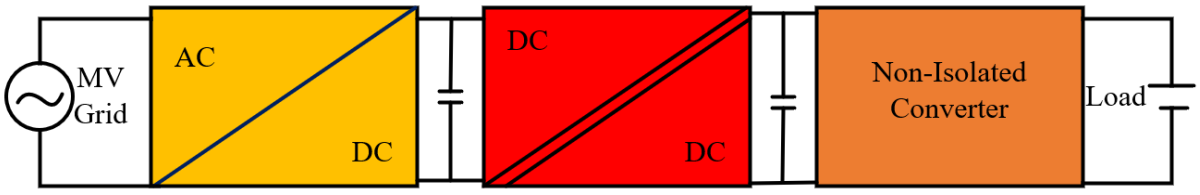

Figure 5.1 Solid-state transformer for EV charging application.

The rest of the chapter is organized as follows: in section 5.2, the proposed controller's fundamentals are explained. The online switch lifetime mapping is discussed in section 5.3,

followed by accelerated aging-based degradation mapping in section 5.4. The proposed controller's design is presented in section 5.5, with the design and performance of the LQR in section 5.6 and the experimental testing and validation in section 5.7. The contribution and future research direction are shown in the conclusion in section 5.8.

5.2 Principle of the proposed controller

Coffin-Manson-based lifetime estimation method estimates lifetime online based on the operating condition. But this model addresses the effect of only the instantaneous operating condition on the lifetime [95]-[96]. Developing a degradation-aware controller based on this model requires large memory and exhaustive processing. The accelerated life testing-based degradation mapping provides a switch degradation trajectory which allows off-line degradation-aware-control planning. However, it does not have adaptive capabilities based on the dynamic operating condition [97]. Another essential feature of the degradation-aware controller is to identify sudden abrupt change. The proposed controller intelligently integrates online lifetime mapping features, accelerated life testing-based degradation mapping, and unexpected degradation identification. The principle of the proposed degradation-aware `controller is shown in Figure 5.2.

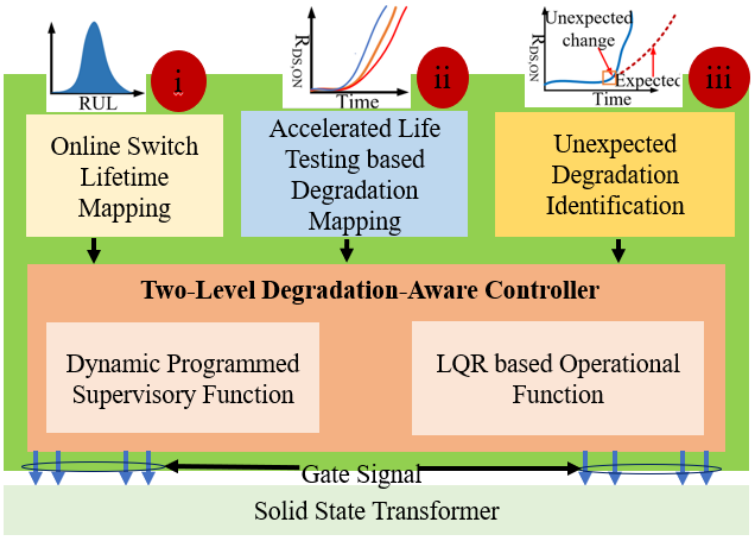

Figure 5.2 Proposed degradation-aware controller of SST.

The proposed controllers operate based on the feedback from three blocks as follows:

i. Online switch lifetime mapping,

ii. Accelerated life testing (ALT)-based degradation mapping, and

iii. Unexpected degradation identification.

In **block i**, the number of cycles to failure (N_f) is estimated online based on the proposed behavioral switch-loss model. In **block ii**, switch degradation is mapped based on the switch's fault precursor trajectory under the ALT. In cascode GaN FET, on-state resistance ($R_{DS,ON}$) shows highest sensitivity to switch degradation [11]-[12]. This $R_{DS,ON}$ trajectory from the accelerated test is statistically analyzed, and a degradation probability is mapped. In **block iii**, $R_{DS,ON}$ is measured online and regularly evaluated to identify any sudden drastic change in switch-health.

Based on these three blocks' inputs, the proposed controller intelligently derates the SST to achieve the target lifetime. The proposed controller has two functions- i) supervisory function and ii) operational function, as shown in Figure 5.2. In a supervisory function, dynamic

programming identifies the switch-health status and estimates degradation-aware optimal operating conditions. In the operational function, an LQR calculates the optimal phase-shift angle for the set degradation-aware operating point.

5.3 Block i: Online switch lifetime mapping

Block ***i*** estimates N_f based on the junction temperature, which is estimated using a switch-loss model. The procedure is shown in Figure 5.3. This block's three main components are- Switch loss model, R-C foster network-based junction temperature estimation, and lifetime estimation. The switching loss causes mean junction temperature ($T_{J,m}$) and Junction temperature variation (ΔT_J), which cause degradation and aging. Cascode GaN FETs experience HF thermo-mechanical stress as different layers in the switch has a mismatched coefficient of thermal expansion (CTE) [90]. This stress causes solder fatigue at the junction of AlGaN and GaN, resulting in wire-bond cracks, solder degradation, or eventual lift-off, which are dominant open-circuit failure mechanisms [98]. In the following subsections, these three components are discussed.

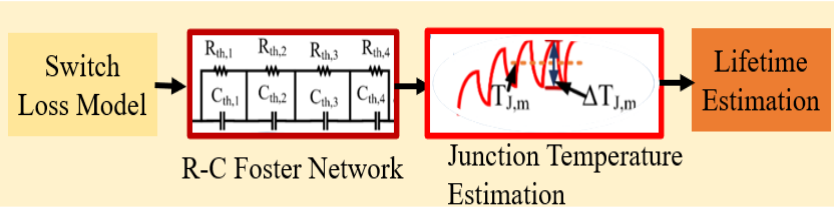

Figure 5.3 Online switch lifetime mapping.

5.3.2 Switch-loss model of cascode GaN FET

A fast and accurate behavioral loss model is proposed. In the cascode structure, a low voltage (LV) Si-MOSFET is cascoded with a normally-on GaN HEMT. Cascode GaN FET is different from IGBT and MOSFET. The turn-off loss is different, especially from IGBT, due to the absence of tailing current in cascode GaN FET. Thus, a switch-loss model for this cascode GaN FET is required. An analytical loss model for the cascode GaN FET is developed in [94], [97]. An equivalent circuit model of the switch-loss is developed based on the complex cascode structure-induced parasitic capacitances and inductances. Thus, this analytical model requires computationally exhaustive processes and proprietary information.

Moreover, this model is developed for DC-DC buck converter and does not address its applicability in a half-bridge configuration [98]. Also, this model requires expensive testing for parameter extraction. Although Piece-wise linear models are fast but are less accurate in high-frequency operations, parasitics' effect is not considered [98]-[99]. The proposed model is developed by analyzing the switching-transition behavior of drain-source voltage (V_{DS}) and drain current (I_d) in the half-bridge configuration to overcome these challenges. Thus, this model does not require solving equivalent circuit models and thus, fast.

Moreover, this behavioral model uses parameters, easily extractable from datasheet and double pulse test (DPT). The effect of parasitic capacitances and commutation inductors will be addressed using the switching transition behavior. Thus, the proposed model is applicable for high-frequency applications.

The switch-loss has two components: the switching loss (P_{sw}) and conduction loss (P_{cond}) as follows:

$$P_{Loss} = P_{cond} + P_{sw} \tag{5.1}$$

The conduction loss can be estimated as follows:

$$P_{cond} = I_L^2 R_{DS,ON} \tag{5.2}$$

where I_L is the RMS load current or inductor current.

This $R_{DS,ON}$ is the function of the temperature and switch-health status. P_{sw} is the summation of the turn-on and turn-off losses.

5.3.2.1 Turn-on loss of cascode GaN FET

Commonly, cascode GaN FET's turn-on is modeled by the LV Si MOSFET and normally-on GaN HEMT's complex physics-based interaction. In this proposed model, the computational complexity is minimized by data-based modeling. This model inherently addresses the effect caused by the parasitic capacitors and commutation inductors and, thus, accurate. As this model does not require solving complex high-degree polynomials and differential equations, this model is fast. The turn-on switching transition of V_{DS} and I_d during turn-on is shown in Figure 5.4(a) that are divided into four regions as follows:

Region I: LV Si gate charging

The cascode GaN FET is comprised of an LV Si MOSFET and a normally-on GaN HEMT. The LV Si-MOSFET controls the switching transitions of the cascode GaN FET. When the gate voltage (Vg) is applied to LV Si MOSFET, the LV Si MOSFET’s gate capacitances

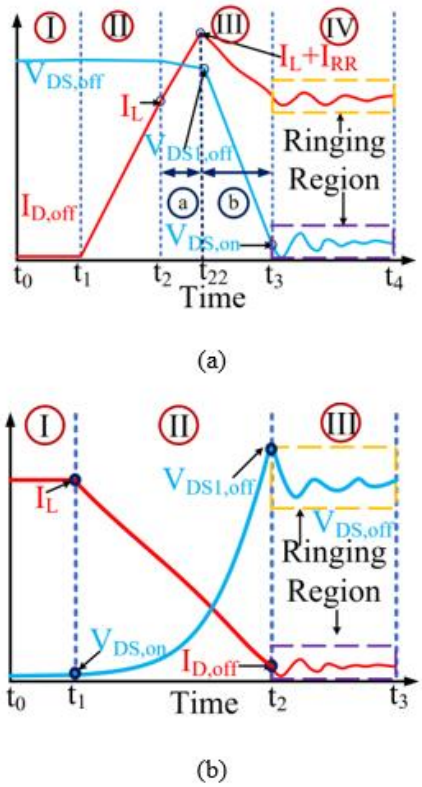

Figure 5.4 V_{DS} and I_d of cascode GaN FET (a) during turn-on transition; (b) during turn-off transition.

(C_{GS} and C_{GD}) are charged. Then, the turn-on process starts when the LV Si MOSFET's gate voltage reaches the threshold, and a conducting channel is established in LV Si MOSFET. The gate-drive loss (P_{dri}) can be expressed as follows:

$$P_{dri}(t) = Q_G V_G F_s \tag{5.3}$$

where Q_G is the gate charge, V_G is the gate voltage, and F_s is the switching frequency. I_d starts rising when the gate-source voltage (V_{GS}) of GaN HEMT reaches its threshold and causes turn-on loss in cascode GaN FET due to V-I overlapping. This V-I overlapping starts at t_1, as shown in Figure 5.4(a).

Region II: Increasing drain current

In this region, the GaN HEMT is fully turned on. Thus, I_d increases linearly and reaches load current (I_L) at the end of this region. In the analytical model, I_d is expressed as a complex relationship between internal parasitics. The interaction of the complicated relationship results in a rise in I_d at a constant rate. Thus, I_d can be modeled in the proposed model as follows:

$$I_d(t) = t\frac{d}{dt}I_{rise} \tag{5.4}$$

where $0 \le I_d < I_L$, $t_1 \le t < t_2$, and dI_{rise}/dt is the rising rate of I_d, which is a constant. This dI_{rise}/dt is dependent on the commutation inductances. The value is estimated from the DPT. During this period, the V_{DS} is assumed constant at $V_{DS,OFF}$. The energy loss during this period is expressed as follows:

$$E_{turn-on-II} = \int_{t_0}^{t_1} V_{DS}(t) I_d(t) dt = \frac{1}{2}(t_1 - t_o)^2 V_{DS,OFF}\left(\frac{d}{dt}I_{rise}\right) \tag{5.5}$$

Region III: Decreasing drain-source voltage

In the half-bridge, two switches in one leg are switching complimentarily. In region III, IL supplies Id to the top switch and reverse-conducting current (I_{RR}) to the bottom switch. Id rises at dI_{rise}/dt till it reaches I_L+I_{RR}. There are two sub-regions in region III. In the sub-region a, I_d increases due to the commutation inductances and internal parasitics. Rather than solving complex differential equations to model this behavior of I_d, it is modeled as follows:

$$I_d(t) = t\frac{d}{dt}I_{rise} + I_L \tag{5.6}$$

where $I_L \le I_d < I_L + I_{RR}$ and $t_2 \le t < t_{22}$. In this sub-region, dI_{rise}/dt remains the same as region II. V_{DS} linearly drops to off-state V_{DS} ($V_{DS1,Off}$)during this time. This drop is due to the increase of I_d over I_L. The behavioral model of V_{DS} can be expressed as follows:

$$V_{ds}(t) = V_{ds,off} + t\frac{d}{dt}V_{DS,1} \tag{5.7}$$

where d$V_{DS,1}$/dt is the falling rate of V_{DS}. This behavioral modeling makes this proposed loss model fast and accurate to use for online lifetime mapping. The energy loss in this sub-region is as follows:

$$\begin{aligned} E_{turn-on-III} &= \int_{t_2}^{t_{22}} V_{DS}(t) I_d(t) dt \\ &= \frac{1}{3}(t_{22}-t_2)^3 \left(\frac{d}{dt}V_{DS,1}\right)\left(\frac{d}{dt}I_{rise}\right) + \frac{1}{2}(t_{22}-t_2)^2 V_{DS,off} \\ &\left(\frac{d}{dt}I_{rise}\right) + \frac{1}{2}(t_{22}-t_2)^2 I_L \left(\frac{d}{dt}V_{DS,1}\right) + (t_{22}-t_2)V_{DS,off} I_L \end{aligned} \tag{5.8}$$

In subregion b, the reverse recovery charge needs to be removed from the bottom switch. The rate of change of I_d is defined by the reverse recovery current of the bottom switch. In this sub-region, I_d falls from the I_L+I_{RR} to I_L when V_{DS} falls from $V_{DS,OFF,1}$ to $V_{DS,ON}$. The internal parasitics of the cascode structure cause these transitions. The analytical model requires internal parasitics information, which is not available. In the proposed model, these behaviors of I_d and V_{DS} can be modeled as follows:

$$I_d(t) = (I_L + I_{RR}) - t\frac{d}{dt}I_{fall} \tag{5.9}$$

$$V_{DS}(t) = V_{DS,Off,1} - t\frac{d}{dt}V_{DS,fall} \tag{5.10}$$

This model inherently addresses the effect of parasitics which affect the rate of change of V_{DS} and I_d. Thus, the modeling approach ensures speed and accuracy.

The energy loss is as follows:

$$E_{turn-on-III,fall} = \int_{t_{22}}^{t_3} V_{DS}(t)I_d(t)dt = (I_L + I_{RR})V_{DS,Off,1}(t_3 - t_{22}) - \frac{1}{2}(t_3 - t_{22})^2 \left(\frac{d}{dt}I_{fall}\right)V_{DS,Off,1} - \frac{1}{2}(I_L + I_{RR})(t_3 - t_{22})^2\left(\frac{d}{dt}V_{DS,fall}\right) + \frac{1}{3}(t_3 - t_{22})^3\left(\frac{d}{dt}I_{fall}\right)\left(\frac{d}{dt}V_{DS,fall}\right) \tag{5.11}$$

Region IV: Ringing region

In this region, I_d and V_{DS} behave like a damping system and reaches their steady states at I_L and $V_{DS,ON}$, respectively. These tendencies can be modeled as follows:

$$I_d(t) = A_1 \exp(-\alpha_1 t)\sin(\omega_{01}t + \theta) + I_L \tag{5.12}$$

$$V_{DS}(t) = A_2 \exp(-\alpha_1 t)\sin(\omega_{01}t + \psi) + V_{DS,ON} \tag{5.13}$$

where A_1 and A_2 are the amplitude of I_d and V_{DS}, respectively, α_1 is the decay rate of I_d and V_{DS}, and ω_{01} is the frequency of I_d and V_{DS}, respectively. At the start of this region, I_d is I_L, V_{DS} is $V_{DS,ON}$, and θ and ψ are zero. The loss in this region is as follows:

$$E_{turn-on-IV} = \int_{t_3}^{t_4} V_{DS}(t) I_d(t) dt \tag{5.14}$$

This $E_{turn\text{-}on\text{-}IV}$ is a function of ω_{01}, α_{01}, A_1, and A_2. These parameters are estimated from the double pulse test.

The total turn-on loss is the summation of the losses in the region I, II, and III:

$$E_{on} = E_{Turn-on,II} + E_{Turn-on,III} + E_{Turn-on,IV} \tag{5.15}$$

1.3.7.2 Turn-off loss of cascode GaN FET

Like turn-on loss, turn-off loss is modeled by analyzing the switching transition behavior. This model is fast and easily implementable without any proprietary information and costly testing. The turn-off transition of V_{DS} and I_d during the turn-off process is shown in Figure 5.4(b), where the turn-off region is divided into three regions.

Region-I: Gate capacitor discharging

The turn-off process starts when Vg is zero and initiates the discharging process of the gate-source capacitor of the LV Si MOSFET. At the end of this stage, cascode GaN FET enters the saturation region. In this region, there are insignificant changes in V_{DS} and I_d. Thus, there is only an insignificant gate-drive loss like (5.3).

Region II: Decreasing drain current

During region II, GaN HEMT is shut down as the interaction of gate capacitance of the LV MOSFET and GaN HEMT. Thus, I_d decreases from I_L to zero. V_{DS} increase from $V_{DS,ON}$ to $V_{ds2,off}$

which is greater than the input voltage (V_{in}). These behaviors of I_d and V_{DS} can be modeled as follows:

$$I_d(t) = I_L + t\frac{d}{dt}I_{fall} \tag{5.16}$$

where at $t=t_1$, $I_d(t_1)=I_L$ and $t=t_2$, $I_d(t_2)=0$.

$$V_{DS}(t) = V_{DS,on} + t\frac{d}{dt}V_{DS,rise} \tag{5.17}$$

here at $t=t_1$, $V_{DS}(t_1)=V_{DS,ON}$ and $t=t_2$,$V_{DS}(t_2)=V_{DS,off}$. These behavioral models address the effects of the parasitic components on the switching transition while avoiding complex modeling and exhaustive calculations. The energy loss in this region is as follows:

$$\begin{aligned} E_{turn-off-II} &= \int_{t_1}^{t_o} V_{DS}(t) I_d(t)dt = I_L V_{DS,on}(t_1 - t_o) - \frac{1}{2}(t_1 - t_o)^2\left(\frac{d}{dt}I_{fall}\right) \\ &-\frac{1}{2}I_L(t_1 - t_o)^2\left(\frac{dV_{DS,rise}}{dt}\right) + \frac{1}{3}(t_1 - t_o)^3\left(\frac{dV_{DS,rise}}{dt}\right)\left(\frac{d}{dt}I_{fall}\right) \end{aligned} \tag{5.18}$$

Region III: Ringing region

In region III, I_d and V_{DS} reach steady-state condition at zero and $V_{DS,OFF}$, respectively. During this period, I_d and V_{DS} behave like an underdamped system. This behavior is modeled as follows:

$$I_d(t) = A_3 \exp(-\alpha_2 t)\sin(\omega_{02} t) \tag{5.19}$$

$$V_{DS}(t) = \Delta V_{DS} \exp(-\alpha_2 t)\cos(\omega_{o2} t) \tag{5.20}$$

where at $t=t_3$, $I_d=0$ and $V_{DS}=V_{DS,OFF}$, A_3 is the amplitude of the overdamped system, α_2 is the decaying rate, ω_{o2} is the decaying frequency. The turn-off loss is as follows:

$$E_{turn-off-III} = \int_{t_2}^{t_3} V_{DS}(t) I_d(t) dt \tag{5.21}$$

This $E_{turn\text{-}on\text{-}III}$ is a function of ω_{02}, α_{02}, A_3, and ΔV_{DS}. These parameters are estimated from the DPT. The total turn-off loss is the summation of the losses as follows:

$$E_{off} = E_{Turn-off,II} + E_{Turn-off,III} \tag{5.22}$$

This behavioral model is a fast and efficient alternative to the complex analytical loss models. Addressing the parasitic capacitances and commutation inductances using the time series behavioral-model, result in fast and accurate switch-loss estimation.

1.3.8 R-C foster model-based junction temperature estimation

T_J is dependent on the switching loss; Thus, this R-C Foster model is the second component in block i, as shown in Figure 5.3. Switch-loss is translated into T_J using the R-C Foster model as follows:

$$T_J = P_{loss} Z_{th} + T_c \tag{5.23}$$

where T_J is the switch's junction temperature, Z_{th} is the thermal impedance, and T_C is the case temperature. Z_{th} is estimated as follows:

$$Z_{th} = \sum_{i=1}^{n} r_i (1 - e^{-t/\tau_i}) \tag{5.24}$$

where r_i is the thermal resistance of the switch, and τ_i is the thermal time constants. Thermal time constraints are expressed as $\tau_i = r_i C_{th,i}$, where $C_{th,i}$ is the thermal capacitance. These thermal parameters are estimated from the switch's transient thermal impedance curve provided in the datasheet.

1.3.9 Lifetime estimation

The Coffin-Manson life estimation model is used that relates N_f to $T_{J,m}$, and ΔT_J experienced by the cascode GaN FET. This model estimates the instantaneous variation in N_f due to change in operating conditions. This model can be expressed as follows:

$$N_f = \mathrm{A}\left(\Delta T_J^{-b_1}\right) exp\left(\frac{b_2}{T_{j,\min} + 273}\right) \tag{5.25}$$

where $T_{J,min}$ is the minimum junction temperature, and A, b_1, b_2, b_3 are the empirical coefficients. These empirical coefficients and estimated T_J include estimation error uncertainties. The switch life consumption accelerates due to change in ΔT_J and $T_{J,m}$ as follows:

$$D.A.F = \left(\frac{\Delta T_{j,1}}{\Delta T_{j,2}}\right)^{-b1} exp\left(\frac{b_2}{T_{j_1,\min} + 273} - \frac{b_2}{T_{j_2,\min} + 273}\right) \tag{5.26}$$

where DAF is the degradation acceleration factor when the operation point changes to (ΔT_{J2}, $T_{J2,m}$) from (ΔT_{J1}, $T_{J1,m}$) due to degradations. The damage to the switch is estimated based on the Miner's linear damage rule as follows:

$$C = \sum \frac{n_i}{N_f} \tag{5.27}$$

where C is the switch's consumed lifetime, n_i is the number of cycles consumed by the switch. This instantaneous N_f is used with the ALT-based switch degradation mapping in block ii to address deviation from the mapped degradation due to a change in operating condition.

5.4 Block ii: Accelerated life testing-based degradation mapping

The regular life of the power semiconductor switches is 10-12 years [2]. The accelerated life testing (ALT) maps the trajectory to a logical timeframe. The accelerated life testing of the cascode GaN FET provides essential insight into $R_{DS,ON}$ trajectory dynamics, and life consumption patterns. The probability density function (PDF) of the lifetime is estimated based on the statistical distribution of the $R_{DS,ON}$ trajectories. In this chapter, a power cycling ALT is used for mapping $R_{DS,ON}$ trajectory. The $R_{DS,ON}$ trajectories of the cascode GaN FET shows that there are three distinct regions over the lifetime of the cascode GaN FET- i) healthy region ii) slow degradation (SD) or constant degradation (CD) region, iii) exponential degradation (ED) region. These tendencies in $R_{DS,ON}$ trajectory, are shown in Figure 5.5(a). Also, there is $R_{DS,ON}$ trajectories which are outliers to the general $R_{DS,ON}$ trajectories as shown in Figure 5.5(b). These outlier trajectories biased the mean $R_{DS,ON}$ trajectory. It is logical to model the degradation trajectory using the median $R_{DS,ON}$ trajectory, insignificantly affected by the outliers. This median trajectory is modeled as follows:

$$P_t(R_{DS,ON} \le R_{DS,ON,med}) = \frac{1}{2} \tag{5.28}$$

where $R_{DS,ON,med}$ is the median of the $R_{DS,ON}$ trajectories. This mapping of the degradation using (28) is shown in Figure 5.5 (b).

5.5 Degradation-aware controller for SST

The proposed controller operates using two functions- i) supervisory function and ii) operational function, as shown in Figure 5.2. If the SST operates at rated power when the switch is degraded, the switches' lifetime is consumed at an accelerated rate and causes unexpected failure. Thus, the

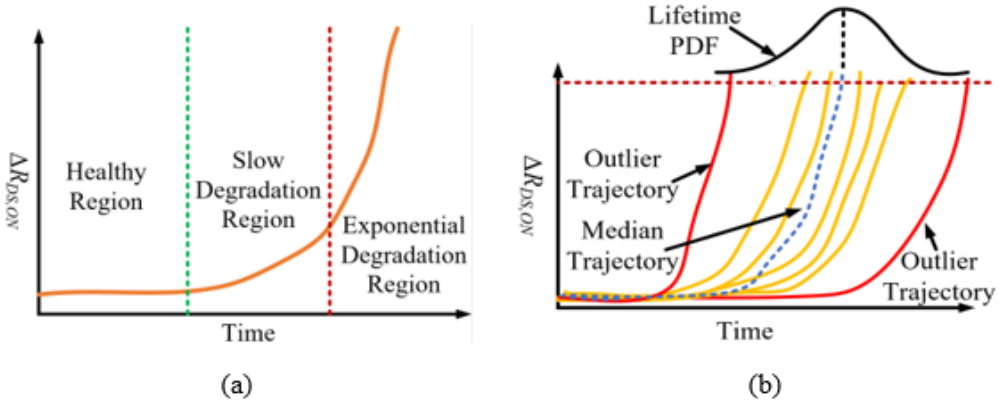

Figure 5.5 $R_{DS,ON}$ trajectory of the cascode GaN FET; (b)median $R_{DS,ON}$ trajectory of cascode GaN FET.

dynamic programmed supervisory function determines the switch-health condition-aware operating point. Based on this operating point, the LQR process estimates the optimal phase shift in the proposed method.

1.3.10 Dynamically programmed supervisory function

Dynamic programming uses the switch degradation mapping to estimate the operating condition to achieve a target lifetime of the SST. To achieve the target lifetime, in the proposed method, the SST operates for the optimal derating trajectory based on the cost function as follows:

$$J = \min\left(C_{rated} - \sum_{i=1}^{3} C_{\deg raded,i} \right) \tag{5.29}$$

where C_{rated} is the rated lifetime under constant junction temperature variation, and $C_{degraded,i}$ is the consumed lifetime. This cost function is minimal when the rated value becomes equal to a switch's lifetime. The dynamic programmed supervisory function's objective is to maximize J by adaptively selecting operating conditions based on its health status. This strategy is graphically shown in Figure 5.6. This strategy ensures a constant junction temperature variation and uniform lifetime consumption. The controller is designed as follows:

Minimize: $Arg_{\max} C_{\deg raded} = \left(C_1 + C_2 + C_3\right)$

Subject to:

Constraint 1: $C_1 > 0,\ C_2 > 0,\ C_3 > 0$

Constraint 2: $0.8\,\mathrm{P}_{\mathrm{r}\,ated} \le P \le \mathrm{P}_{\mathrm{r}\,ated}$

Constraint 3: $C_{\deg radate} \le C_{rated}$

Constraint 4: $P_{II} > P_{III}$

where C_1, C_2, and C_3 are the consumed lifetime in a region I, II, and III. The derating algorithm is shown in Figure 5.6. As the switch will be more degraded in the exponentially degraded (ED)

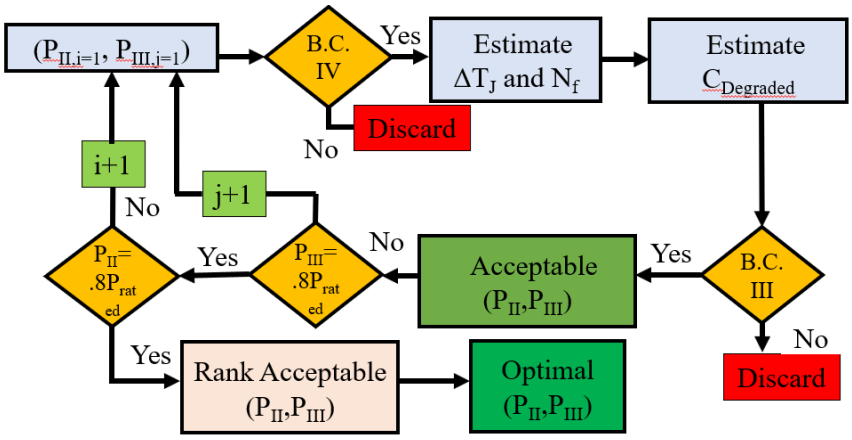

Figure 5.6 Optimal operating condition estimation algorithm.

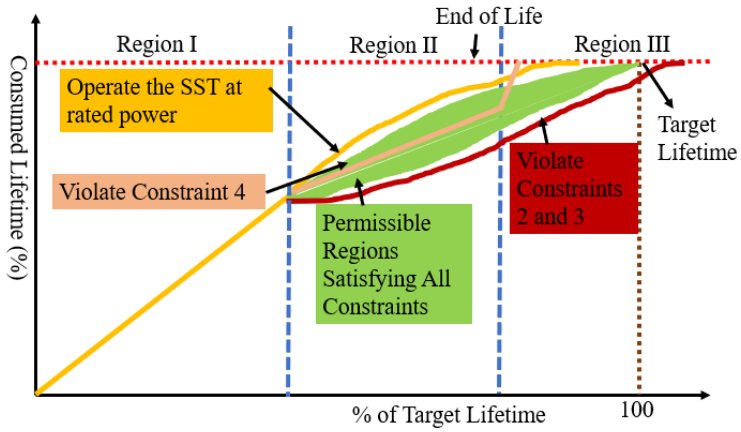

Figure 5.7 Degradation-aware dynamic programmed operating conditions.

region than in the slow degradation (SD) region, it is logical to impose higher derating in the ED region. Based on the constraints, the allowed operating conditions are shown in Figure 5.7. When the switch is healthy, the SST operates at rated condition. However, the SD and ED regions' operating conditions are programmed based on constraints 1-4. If the SST operates at P_{min}, it will have a maximum lifetime, but it will violate constraint 3. If the SST operates at P_{rated}, J will be maximum, but the SST will fail before its target lifetime. Different combination of operating conditions in these two regions leads to different lifetime for the SST. To integrate the dynamic operating conditions, (26) is used to estimate lifetime consumption under different operating conditions. Eon and Eoff are integrated into the proposed controller as a look-up table to reduce the computational burden.

1.3.11 LQR based operational function

The operational function controls the DAB stage in SST to deliver the reference voltage. The disturbance causes system instability. In this sub-section, a linear quadratic regulator (LQR) is designed to operate the DAB stage in SST. LQR ensures optimal phase-shift angle for the

derated operating condition set by the supervisory function. The LQR shows robust performance to system disturbance and estimates optimal phase-angle, which ensures efficiency. This LQR design requires a state-space model of the DAB stage. The equivalent circuit of the DAB is shown in Figure 5.8, where L is the HF transformer's leakage inductance, VAB is the inverter output, and VCD is the rectifier input voltage.

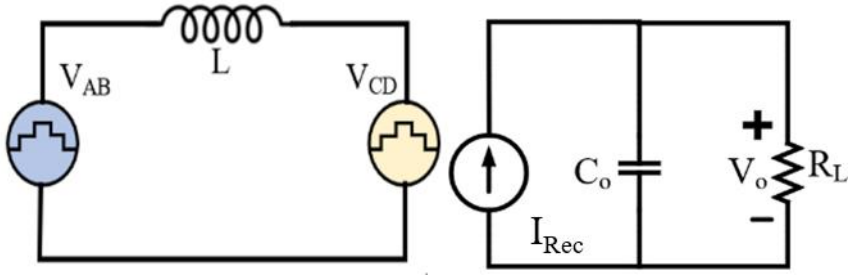

Figure 5.8 Equivalent circuit of DAB stage of SST.

The average model of the output stage of the DAB is shown in Figure 5.8. Using Kirchoff's current law:

$$Co\frac{dVo}{dt}+\frac{Vo}{R_L}-\frac{ViD(1-D)}{2Lf_s}=0 \tag{5.30}$$

where V_i is the input voltage, V_o is the output voltage, R_L is the load, C_o is the output capacitor, and f_s is the switching frequency. The small-signal model of this output average model for small variations in v_o and d is as follows:

$$\frac{dv_o}{dt}=\frac{-vo}{R_LC_o}+\frac{V_i(1+2D)}{2LC_of_s}d \tag{5.31}$$

The state-space model of the DAB is as follows:

$$\dot{x} = Ax + Bu \tag{5.32}$$

where

$$A = \begin{bmatrix} 0 & 1 \\ 0 & -\dfrac{1}{R_L C_o} \end{bmatrix}, \qquad B = \begin{bmatrix} 0 \\ \dfrac{V_i(1+2D)}{2LC_o f_s} \end{bmatrix} \qquad x = \begin{bmatrix} \int v_o dt \\ v_o \end{bmatrix} \qquad \text{and } u = d$$

In this state-space model, a new variable, $\int v_o dt$ is introduced, which results in zero steady-state error. The quadratic cost function of the system is as follows:

$$J_{LQR} = \int \left(x^T Q x + u^T R u \right) dt \tag{5.33}$$

where J_{LQR} is the quadratic cost function, Q is a 2-by-2 positive semi-definite matrix, R is a scalar that should be positive. The closed-loop poles' location depends on the choice of Q and R. In this dissertation, R=1, and Q=[q_1 0; 0 q_2] is used. Thus, q_1 and q_2 will decide the speed and damping of the system. For the state feedback, it is assumed that

$$u = -kx \tag{5.34}$$

where $k = [k_1 \quad k_2]$ is the system's feedback gain.

It is found by putting (5.34) into (5.35)as follows:

$$J_{LQR} = \frac{1}{2}\int [x^T (Q + k^T Rk)x]dt \tag{5.35}$$

The optimal solution for *k* is found as follows:

$$k = R^{-1}B^T P \tag{5.36}$$

where *P* is the solution of the Algebraic Recatti Equation as follows:

$$PA + A^T P - PBR^{-1}B^T + Q = 0 \tag{5.37}$$

5.6 LQR design and its performance analysis

The LQR design requires the operating point information as shown in (5.30). The operating frequency of the SST is 50 kHz, the rated voltage and power are 400 V and 5kW, respectively, the leakage inductance is 53μH, and the output capacitance is 120 μF. Based on this operating condition and system information, The LQR is designed to have sufficient controller speed and zero steady-state error. The root locus of the system is shown in Figure 5.9 (a). The step response of the modeled LQR controller is shown in Figure 5.9(b) with *R*=1, *Q*=[50 0;0 10^(-5.5)] and *K*=[-7.0711 0.0048]. The system's settling time is 0.043 sec. The overshoot is less than 5%. Thus, the LQR is operating with reasonable speed and accuracy.

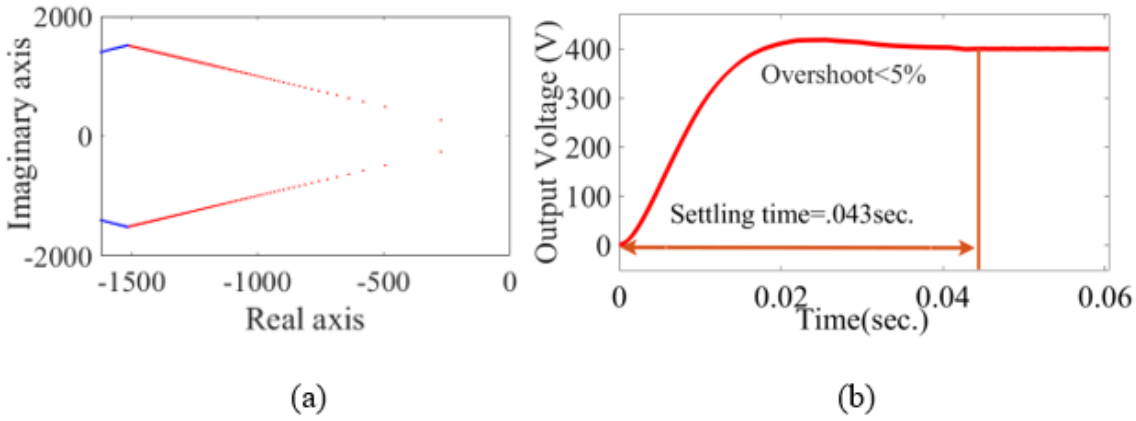

Figure 5.9 (a) Root-locus and (b) the step response of the LQR controller.

5.7 Experimental testing and validation

1.3.12 Validation of behavioral switch loss model

The commutation inductance due to PCB layout plays a vital role in the switching loss estimation. These inductances change with PCB layout, which is application-dependent. Thus, it is essential to conduct a DPT conducted on the same PCB layout as the SST to address these inductances' effect on the switching loss. It is essential to measure V_{DS} and I_d with precision and speed for accurate loss estimation. Thus, V_{DS} and I_d measurement requires high bandwidth probes. Differential voltage probe (TMDP0200) and Coaxial shunt 0.1 Ω SSDN-10 current sensor are used for high precision and fast measurement. The V_{DS} and I_d are shown in Figure 5.10 during turn-on and turn-off transitions. The turn-on and turn-off losses are estimated by calculating the energy loss due to V_{DS} and I_d's cross-over. Moreover, these signals are properly aligned to improve the integrity of the testing. In the datasheet, input transfer capacitance (C_{iss}), output transfer capacitance (C_{oss}), and reverse transfer capacitance (C_{rss}) are available. C_{GD}, C_{GS}, and C_{DS} are extracted from these transfer capacitances as follows:

$$C_{GS} = C_{iss} - C_{rss} \tag{5.38}$$

$$C_{DS} = C_{oss} - C_{rss} \tag{5.39}$$

$$C_{GD} = C_{rss} \tag{5.40}$$

Inductances in the power loop are estimated using the DPT testing and the deskewing method. The turn-on and turn-off ringing region parameters are also estimated from this DPT test. These parameters are used in (5.3)-(5.25) for the switching loss estimation and integrated into the controller as a look-up table.

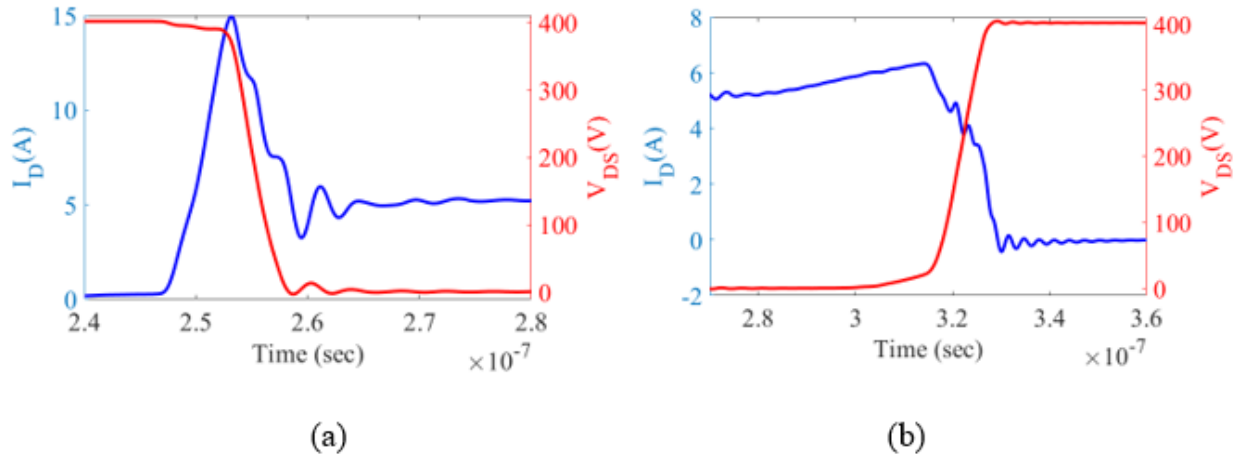

Figure 5.10 Drain-source voltage and drain current (a) during turn-on and (b) during turn-off.

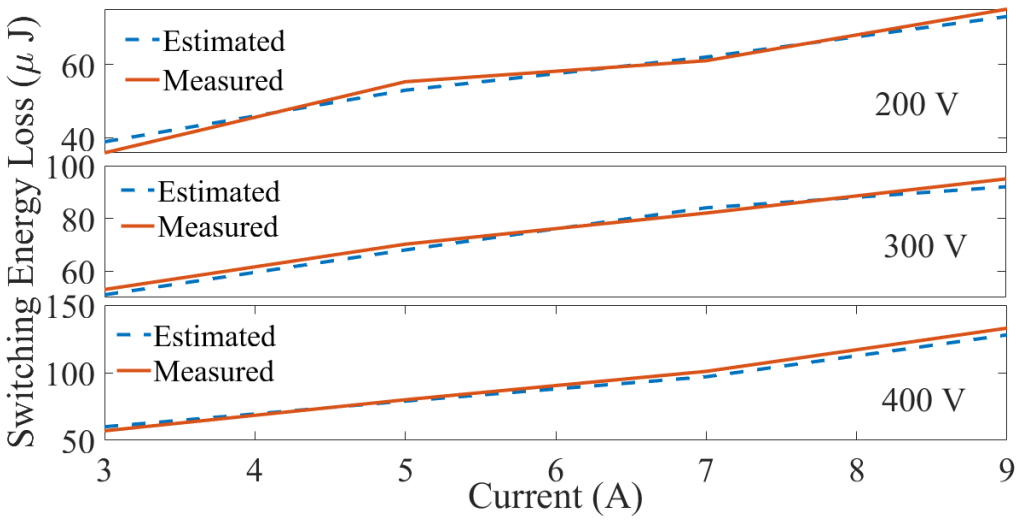

Figure 5.11 Estimated and measured switching energy loss at the different operating conditions.

This estimated switching loss is compared with the measured loss from the DPT at different operating conditions to validate the proposed switching-loss model, as shown in Figure 5.10.

This behavioral switching loss model closely follows the experimental switching loss tendency and has a 2.3% average mean squared error. This model is fast, the parameter extraction is easy, and it follows the experimental model's loss tendency closely.

1.3.13 Validation of proposed degradation-aware controller

An experimental setup for the degradation-aware controller is shown in Figure 5.12 and Figure 5.13. The operating frequency is 50 kHz, the rated input and output voltage is 400 V, the rated power is 5kW, and the leakage inductance is 53µH. The $R_{DS,ON}$ trajectories of the cascode GaN FET under ALT is shown in Figure 5.14. In the power cycling ALT test, the switch's case temperature is varied between 25°C to 100°C using active-switch heating. To monitor $R_{DS,ON}$ real-

time, $V_{DS,ON}$ is measured by the signal conditioning circuit in [14] and I_d is measured by the shunt resistor. This $R_{DS,ON}$ measurement is sampled at steady-state to avoid the effect of switching transients. To reduce the effect of the noise, 50 $R_{DS,ON}$ samples are averaged.

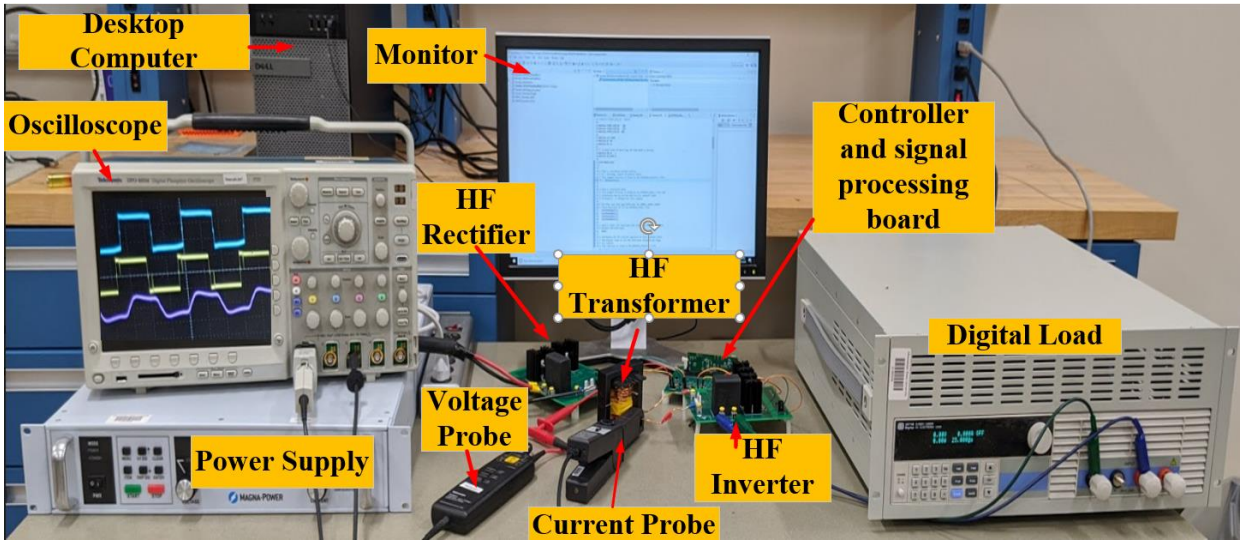

Figure 5.12 Experimental setup of cascode GaN FET-based SST.

These $R_{DS,ON}$ samples are also temperature-scaled. It is observed that till 60% of life, the switches are in the healthy region, and $\Delta R_{DS,ON}$ is between 0%-2%. From 60% to 80%, the switch is in the SD region where $\Delta R_{DS,ON}$ is between 2%-7%. When $\Delta R_{DS,ON}$ is greater than 7%, the switch is in the ED region and about to fail. This tendency in $R_{DS,ON}$ trajectory over its lifetime is mapped using (28). If the $\Delta R_{DS,ON}$ is <2%, the switch is healthy. If 2%<$\Delta R_{DS,ON}$ is <7%, the switch is in the SD region, and otherwise, the switch is in the ED region. The statistically modeled median $R_{DS,ON}$, and the dynamic programmed estimated optimal operating trajectory are shown in Figure 5.15.

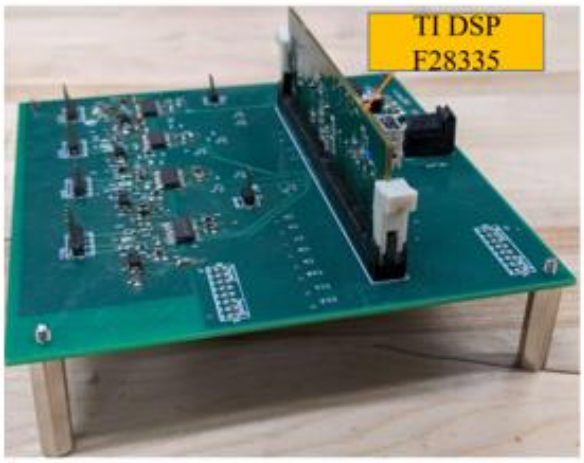

(a)

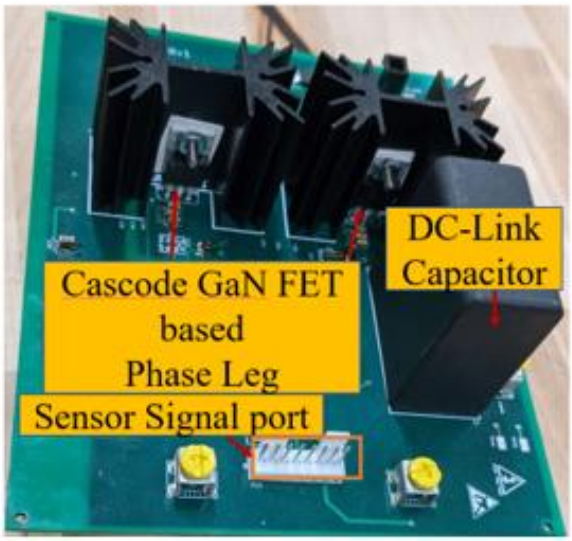

(b)

Figure 5.13 (a) Control Board (b) GaN FET based Inverter/Rectifier.

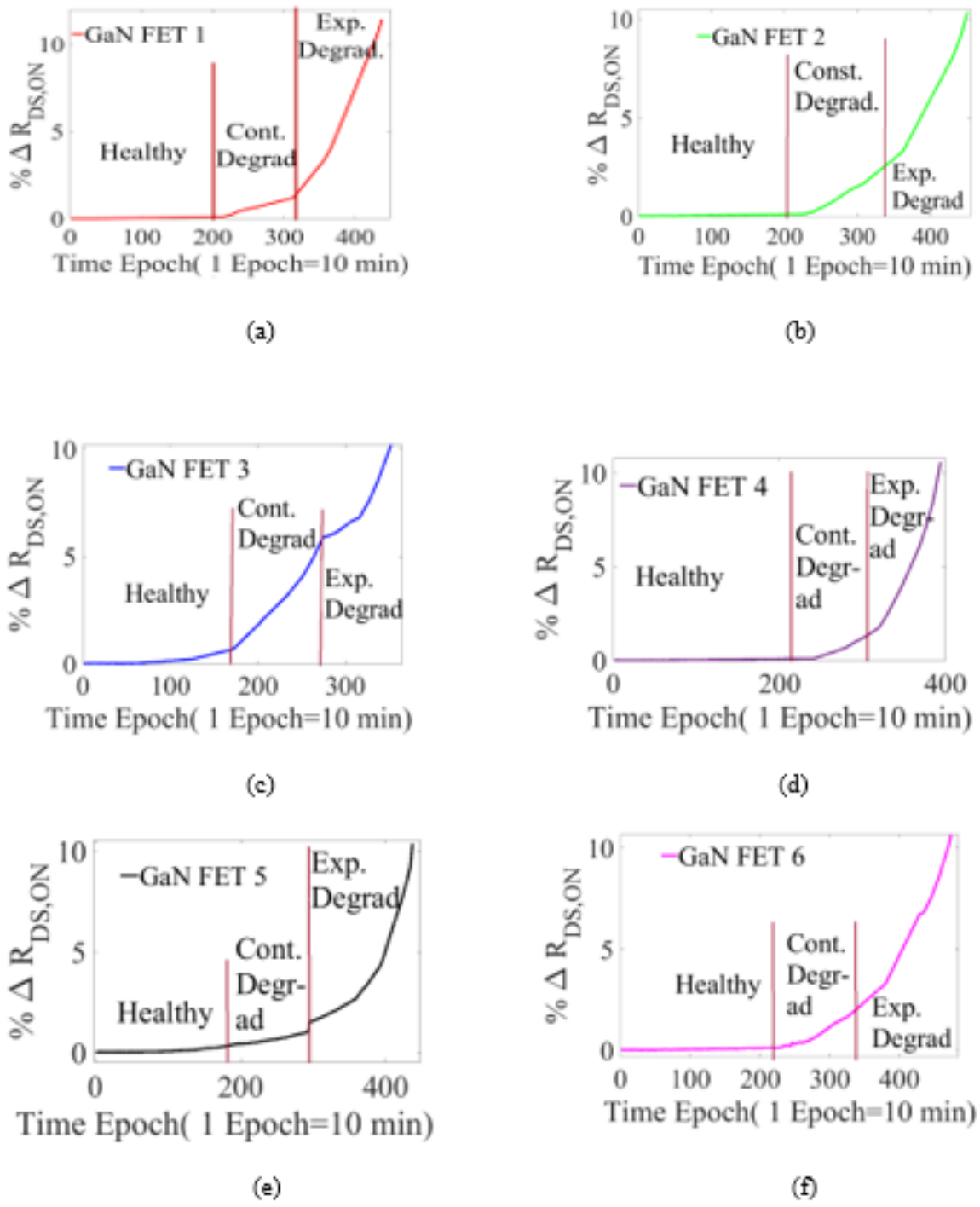

Figure 5.14 Actual trajectory of RDS,ON (a) GaN FET1, (b) GaN FET2, (c) GaN FET3, (d) GaN FET4, (e) GaN FET5, and (6) GaN FET6.

The system is operated with a new switch to validate the proposed control system's applicability, 40% degraded switch, and 80% degraded switch. The system operates at a rated

inductor current at Vo=400V when the switch is healthy, as shown in Figure 5.16. As 40% degraded switch also in the healthy region, the system keeps operating underrated condition. The inductor current is decreased when the degradation-aware degradation controller identifies the switch in the ED region, as shown in Figure 5.16. The optimal operating condition is identified as Vo=360 V.

This derated operating point reduces the junction temperature experienced by the switch. The lifetime profile for different $T_{J,m,}$ and ΔT_J is shown in Figure 5.17. The PDF and cumulative density function (CDF) of N_f at (ΔT_J=10^{o}C, $T_{J,m}$=50^{o}C) and (ΔT_J=11^{o}C, $T_{J,m}$=51^{o}C) are shown in Figure 5.18. When 1^{o}C reduces $T_{J,M}$, *and* ΔT_J, CDF becomes less steep and increases N_f by 4%. This intelligently derated operating condition ensures the switch will operate 4% more than if the operating condition remains the same. This extended life is crucial in scheduling maintenance before the switch fails.

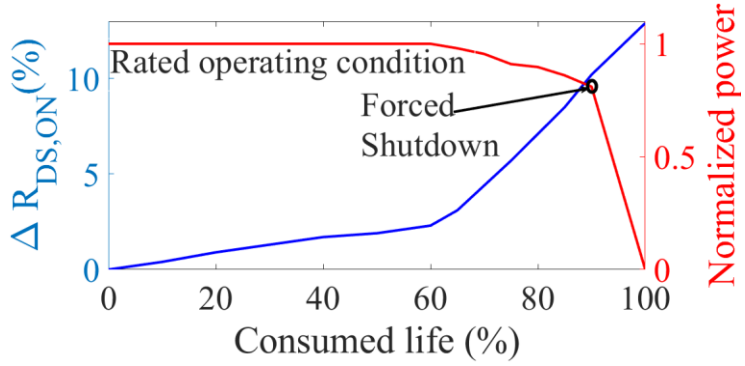

Figure 5.15 $R_{DS,ON}$ trajectory mapping, and dynamic-programmed operating point mapping.

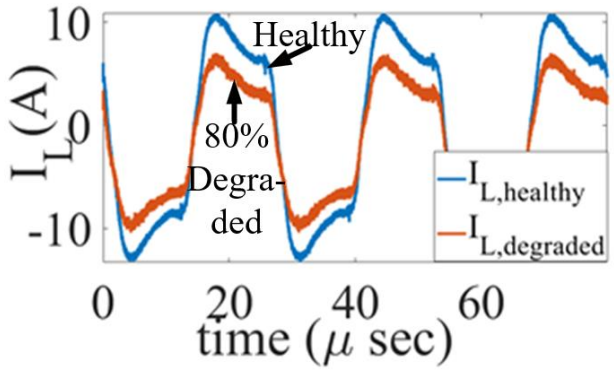

Figure 5.16 Inductor current at the rated condition and degraded condition.

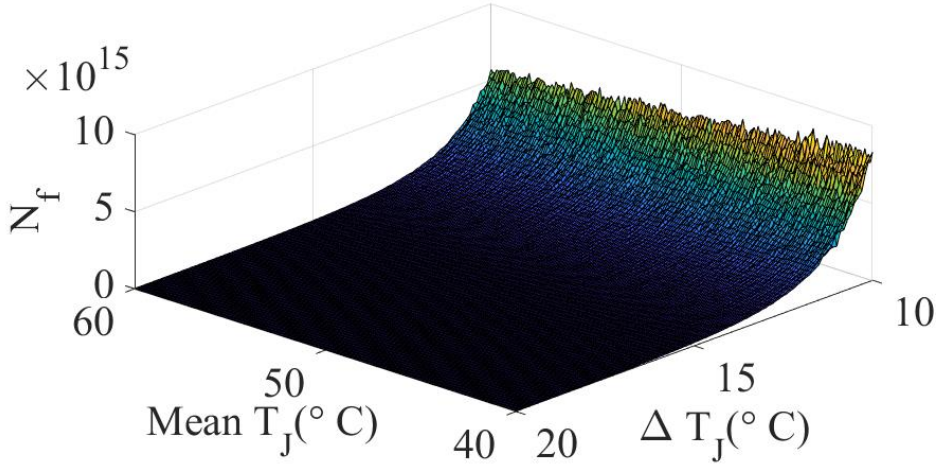

Figure 5.17 Lifetime profile for different ΔT_J and $T_{J,m}$.

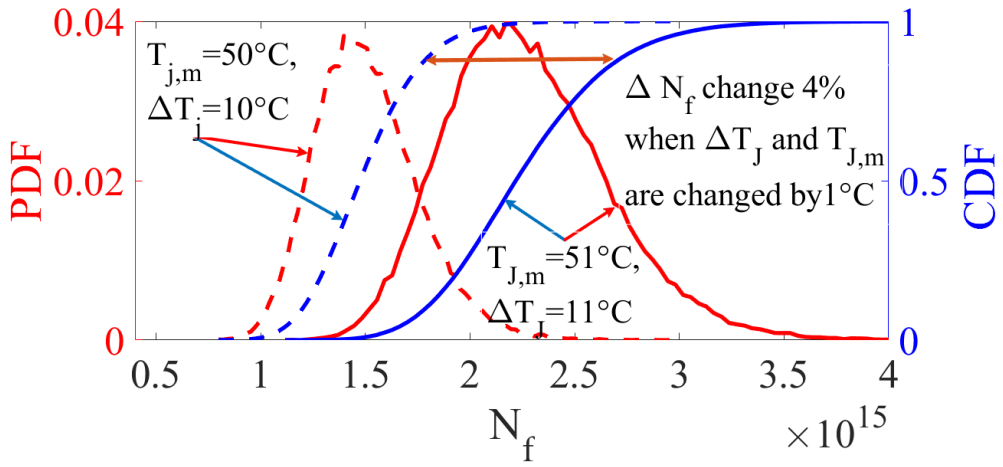

Figure 5.18 The effect of ΔT_J and $T_{J,m}$ on lifetime for switch degradation.

5.8 Conclusion

In this chapter, a degradation-aware controller for SST is proposed to ensure the system's integrity and reliability. The proposed controller intelligently derates the power considering switch-health and avoids system failure before the expected lifetime. This degradation-aware controller provides a 4% increase in life over the traditional controller by derating the SST up to 80% of its rated power. This lifetime extension is achieved by considering $T_{J,m,}$ and ΔT_J increase by 1^{o}C due to switch degradation. Although the proposed controller derates the SST with switch degradation, this extended lifetime is significant for maintenance scheduling and avoid unexpected failure. The proposed data-sheet-based behavioral cascode GaN FET switch-loss model shows a 2.3% average mean squared error. This model does not require proprietary information about the switch.

Moreover, the parameters are easily extractable from the datasheet and DPT. This loss model does not require exhaustive computation. Besides, it is easily integrated into the real-time controller as a look-up table due to its low computational complexity. The proposed controller's

complexity is lowered as it works on the current health status and life consumption and does not require storing data over the switch's life. Integrated into digital twin and cloud computing platforms, these health-monitoring systems and degradation-aware controllers will be useful for industrial and electric-transport maintenance and asset management.

CHAPTER VI

CONCLUSION AND FUTURE SCOPE OF RESEARCH

In this chapter, the Ph.D. research summary and the future research scopes are presented. The PESs' market share is expanding at 5.8% per year [5], and they are increasingly used in innovative mission-critical applications. Wide bandgap switches show immense potential in high-frequency high-power applications, but lack of adequate reliability study delays their wide adaptability. Thus, the PESs' reliability has been increasingly gaining importance for achieving wide acceptability, ensuring robustness, and avoiding unexpected failure. In this dissertation, the component- and system-level prognosis strategies have been analyzed to identify the degradation, estimate the RUL, enhance the system's life, and avoid unexpected failure.

6.1 Summary of research and conclusion

In this research, degradation analysis and RUL estimation of IGBT and cascode GaN FET have been investigated with their system-wide integration. In chapter I, the motivation of the research and research goal is presented. The broader aspects of the reliability study are discussed in this chapter. Modern applications and the state-of-the-art PES reliability research are presented in chapter II. This chapter discusses the PES reliability research's broader scope for its robustness and wide acceptability in mission-critical applications.

Chapter III presents a high accuracy APF-based *RUL* estimation method of IGBT. The performance of the proposed APF method is compared to state-of-the-art SIR PF in *RUL* estimation. The RMS error in *RUL* estimation decreases from 22% to 17.8% when APF

is applied. The trajectory of $V_{CE,ON}$ can be segmented into three regions: Region 1: constant tendency, region 2: linear increasing tendency, and region 3: exponential tendency. It shows that the region-aware application of the proposed method improves its *RUL* estimation performance.

In chapter IV, an SKRR-PF based RUL estimation method for cascode GaN FET is presented. The proposed method includes the unique characteristic of cascode GaN FET in measurement, improves the RUL estimation's speed and accuracy, and reduces harsh system noise effect by including SKRR in the PF framework. High accuracy can be achieved in the proposed RUL estimation under dynamic and extreme operating conditions, even when the health status of the cascode GaN FET changes abruptly. APF shows 7%-15% tracing error under steady-state operating conditions, while the proposed SKRR-PF shows significantly reduced error down to 6%-8%. SKRR-PF and APF show 6%-8% and 15%-17% error estimation, respectively, under the dynamic operating condition with high accuracy.

In chapter V, a degradation-aware controller for SST is proposed to ensure its integrity and reliability. The proposed controller intelligently derates the power considering switch-health and avoids premature PES failure. This degradation-aware controller provides a 4% increase in life over the traditional controller by derating the SST up to 80% of its rated power. This lifetime extension is achieved by considering $T_{J,m}$, and ΔT_J increase by 1^oC due to switch degradation. Although the proposed controller derates the SST with switch degradation, this extended lifetime is significant for maintenance scheduling and avoid unexpected failure. The proposed data-sheet-based behavioral cascode GaN FET switch-loss model shows a 2.3% average mean squared error. This model does not require proprietary information about the switch.

Moreover, the parameters are easily extractable from the datasheet and DPT. This loss model does not require exhaustive computation. Besides, it is easily integrated into the real-time

controller as a look-up table due to its low computational complexity. The proposed controller's complexity is lowered as it works on the current health status and life consumption and does not require storing data over the switch's life.

6.2 Future scope of research

The high-power high-frequency PESs are focusing on the power-density and efficiency. Although they show promise in different emerging applications, PES's reliability and robustness are extremely important for their wide acceptability. The advancement of communication and computation technology widens the scope of reliability research in power electronics. The following areas are very promising in the power electronic reliability research:

i) Artificial intelligence assisted PES reliability.

ii) Reliability integrated switch model development for the simulation study.

iii) Reliability-oriented intelligent power electronics switch fabrication.

iv) System-wide comprehensive power electronics reliability.

6.2.1 Artificial intelligence assisted reliability of the PES

One of the prognosis study's critical aspects is degradation identification, degradation mapping, and degradation-aware control. Artificial intelligence techniques, especially deep learning techniques, show the capability to learn from data and evolve likewise. Although these methods show potential in prognosis, their real-time implementation is challenging. Degradation is a slow process, and historical online degradation analysis requires large memory storage. Moreover, specialized GPU/CPU are required to implement these A.I.-based techniques. The recent development of low-cost computer processing power, IoT, and cloud computing

technologies will be instrumental in employing A.I.-based real-time PES degradation analysis. Degradation-sensitive signals can be acquired and stored in the cloud, which will address the challenge of large memory storage and processing. An outline of A.I.-based degradation identification, lifetime estimation, and PES control strategy is shown in Figure 6.1.

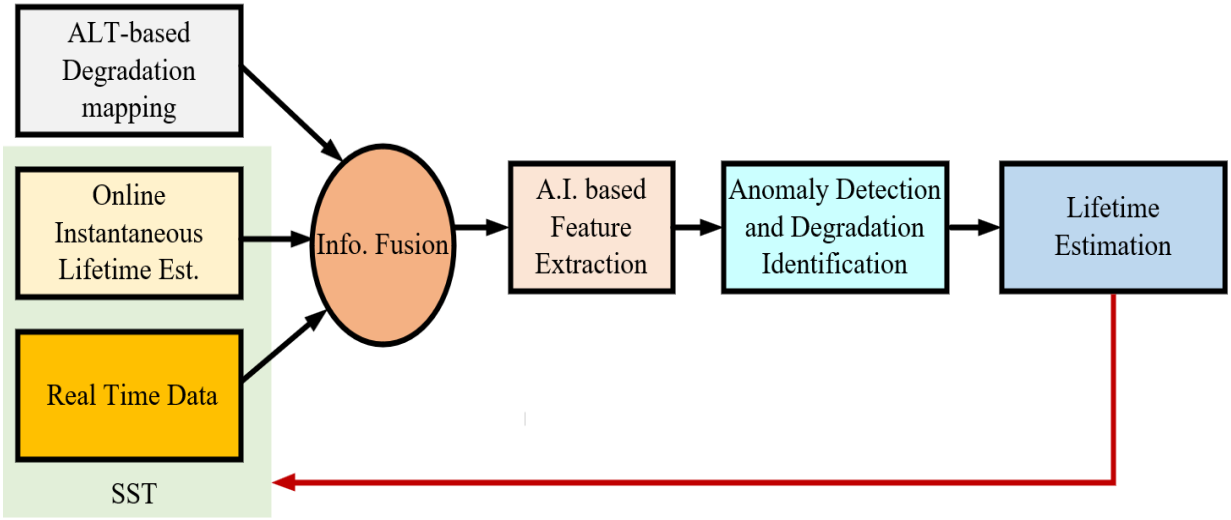

Figure 6.1 A.I. based degradation identification, lifetime estimation, and PES control strategy.

6.2.2 Reliability integrated switch model development for simulation study

The circuit simulation provides insight into the behavior of the PES during operation. Although the non-linear switch behavior is integrated into the Spice model, switch-degradation is still not incorporated. The development of a degradation-aware spice model will help the system designer assess the system's reliability and robustness without expensive and time-consuming testing. A lifetime estimation strategy from the degradation-aware simulation is shown in Figure 6.2.

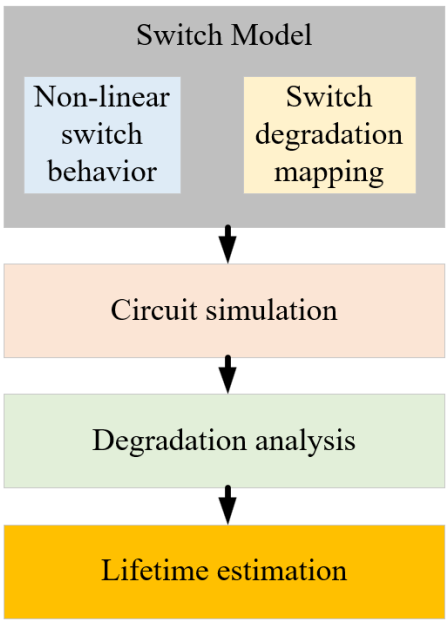

Figure 6.2 Degradation-aware switch model simulation for lifetime simulation.

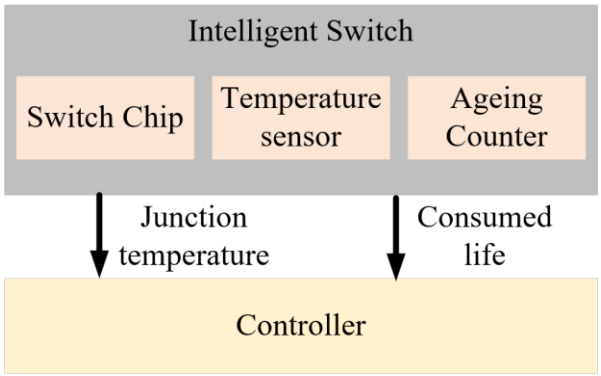

Figure 6.3 Reliability-oriented intelligent power electronics switch fabrication.

6.2.3 Reliability oriented intelligent power electronics switch fabrication

The intelligent switch development is a prospective research area that will use the junction temperature estimated from the integrated temperature sensor for real-time degradation estimation. This intelligent switch will provide the system higher reliability and robustness.

Moreover, it will reduce the dependence on signal conditioning and noise on the degradation data. This switch can be directly interfaced with the controller for system control and lifetime estimation, as shown in Figure 6.3.

6.2.4 System-wide comprehensive power electronics reliability

This dissertation focuses on switch degradation mapping and switches degradation aware controller development for the SST. Other researches have been focused on capacitors, sensors, and batteries, which did not consider the simultaneous degradation of all the components. The degradation of these components affects the integrity of the PES. A comprehensive and real-time PES reliability is another potential research area. This reliability study will combine ALT-based degradation data and real-time component health information, as shown in Figure 6.4.

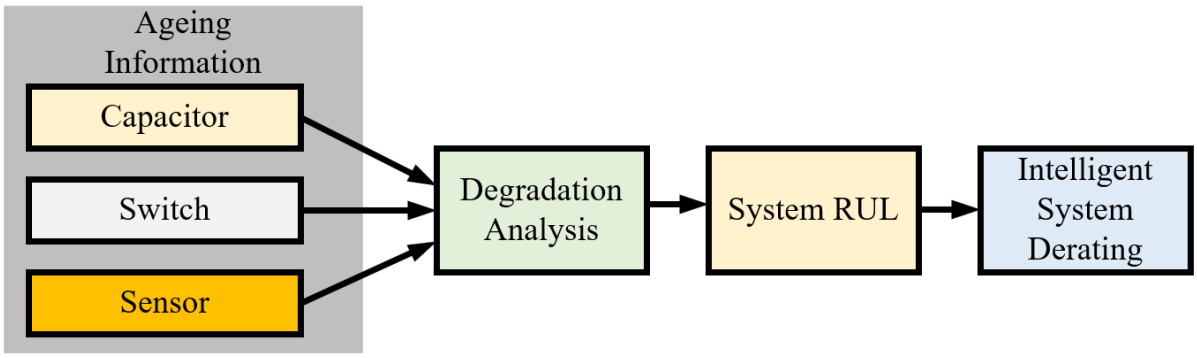

Figure 6.4 System-wide comprehensive PES reliability.

REFERENCES

E. Wolfgang, "Examples for failures in power electronics systems," presented at *ECPE Tutorial 'Rel. Power Electron. Syst.*, Nuremberg, Germany, Apr. 2007.

P. Jacob, M. Held, P. Scacco, and W. Wu, “Reliability testing and analysis of IGBT power semiconductor modules,” in *Proc. IEE Colloquium IGBT Propulsion Drives,* pp. 319–325, 1995.

H. Ye, M. Lin, and C. Basaran, “Failure modes and FEM analysis of power electronic packaging,” *Finite Elements Anal. Design,* vol. 38, pp. 601–612, 2002.

U. Scheuermann, “Power cycling lifetime of advanced power modules for different temperature swings,” in *Proc. Power Conversion Intelligent Motion,* 2002, pp. 59–64.

M. Rodriguez, A. Claudio, D. Theilliol, and L. G. Velan, “A new fault detection technique for IGBT based on gate voltage monitoring,” in *IEEE Power Electron. Spec. Conf.*, 2007, pp. 1001–1005.

B. Farokhzad, “Method for early failure recognition in power semiconductor modules,” *U.S. Patent* 6145107, 2000.

J. Morroni, A. Dolgov, M. Shirazi, R. Zane, and M. Dragan, “Online health monitoring in digitally controlled power converters,” in *IEEE Power Electron. Spec. Conf.*, 2007, pp. 112–118.

A. Bryant, P. Mawby, P. Palmer, E. Santi, and J. Hudgins, “Exploration of power device reliability using compact device models and fast electrothermal simulation,” *IEEE Trans. Ind. Appl.*, vol. 44, no. 3, pp. 894–903, May/Jun. 2008.

S. Mohagheghi, R. G. Harley, T. G. Habetler, and D. Divan, “Condition monitoring of power electronic circuits using artificial neural networks,” *IEEE Trans. Power Electron.,* vol. 24, no. 10, pp. 2363–2367, Oct. 2009.**

H. Oh, B. Han, P. McCluskey, C. Han, and B. D. Youn, “Physics-of- Failure, Condition Monitoring, and Prognostics of Insulated Gate Bipolar Transistor Modules: A Review,” *IEEE Trans. on Power Elec.*, vol. 30, no. 5, pp. 2413-2426, May 2015.

B. Lu and S. K. Sharma, “A Literature Review of IGBT Fault Diagnostic and Protection Methods for Power Inverters,” *IEEE Trans. on Industry Applications,* vol. 45, DOI: 10.1109/TIA.2009.2027535, no. 5, pp. 1770-1777, Sept.-Oct. 2009.

C. Busca, “Modeling Lifetime of High Power IGBTs in Wind Power Applications-an Overview,” *IEEE International Symposium on Ind. Elec.*, pp. 1408-1413, 2011.

S. Yang, A. Bryant, P. Mawby, D. Xiang, L. Ran, and P. Tavner, “An Industry-Based Survey of Reliability in Power Electronic Converters,” *IEEE Trans. on Industry Applications,* vol. 47, no. 3, pp. 1441-1451, May-June 2011.

B. Ji, V. Pickert, W. Cao, and B. Zahawi, “In Situ Diagnostics and Prognostics of Wire Bonding Faults in IGBT Modules for Electric Vehicle Drives,” *IEEE Trans. on Power Elec.*, vol. 28, no. 12, pp. 5568-5577, Dec. 2013.

B. Ji et al., “In Situ Diagnostics and Prognostics of Solder Fatigue in IGBT Modules for Electric Vehicle Drives,” *IEEE Trans. on Power Elec.*, vol. 30, no. 3, pp. 1535-1543, March 2015.

R. Wu, F. Blaabjerg, H. Wang, M. Liserre, and F. Iannuzzo, “Catastrophic Failure and Fault-Tolerant Design of IGBT Power Electronic Converters - An Overview,”*39th Annual Conference of the IEEE Ind. Elec. Society*., pp. 507-513, 2013.

L. Rodriguez-Urrego, E.García, E.Quiles, A.Correcher, F.Morant, and R.Pizá, “Diagnosis of Intermittent Faults in IGBTs Using the Latent Nestling Method with Hybrid Coloured Petri Nets,” *Mathematical Problems in Engineering*, vol. 2015, doi:10.1155/2015/130790, pp.14, 2015.

B. Saha, J. R. Celaya, P. F. Wysocki, and K. F. Goebel, “Towards Prognostics For Electronics Components,” *IEEE Aerospace Conference*, pp. 1-7, 2009.

K. Goebel, B. Saha, and A. Saxena, “A Comparison of Three Data-Driven Techniques For Prognostics,” *Proceedings of the 62nd Meeting of the Society For Machinery Failure Prevention Technology*, vol. 2008., pp. 119–131, May 2008.

Y. Xiong, X. Cheng, Z. J. Shen, C. Mi, H. Wu, and V. K. Garg, “Prognostic and Warning System for Power-Electronic Modules in Electric, Hybrid Electric, and Fuel-Cell Vehicles,” *IEEE Trans. Ind. Electron.*, vol. 55, pp. 2268–2276, Jun. 2008.

M. Musallam, C. M. Johnson, C. Yin, C. Bailey, and M. Mermet-Guyennet, “Real-Time Life Consumption Power Modules Prognosis Using On-Line Rainflow Algorithm in Metro Applications,” *IEEE Energy Conversion Congress and Exposition*, pp. 970-977, 2010.

T. Sreenuch, A. Alghassi, S. Perinpanayagam, and Y. Xie “Probabilistic Monte-Carlo Method for Modelling and Prediction of Electronics Component Life,” *Int. Journal on Adv. Comput. Sci. Applications*, vol. 5, no. 1, pp. 96-104, 2014.

X. Si, W. Wang, C. Hu, and D. Zhou, “Remaining Useful Life Estimation—A Review on The Statistical Data-Driven Approaches,” *Eur. Jour. Oper. Res.*, vol. 213, no. 1, pp. 1-14, 2011.

A. Singh, A. Anurag, and S. Anand, “Evaluation of V_{CE} at Inflection Point for Monitoring Bond Wire Degradation in Discrete Packaged IGBTs,” *IEEE Trans. on Power Elec.*, vol. 32, no. 4, pp. 2481-2484, April 2017.

M. A. Eleffendi and C. M. Johnson, “In-Service Diagnostics for Wire-Bond Lift-off and Solder Fatigue of Power Semiconductor Packages,” *IEEE Trans. on Power Elec.*, vol. 32, no. 9, pp. 7187-7198, Sept. 2017.

D. W. Brown, M. Abbas, A. Ginart, I. N. Ali, P. W. Kalgren, and G. J. Vachtsevanos, “Turn-Off Time as an Early Indicator of Insulated Gate Bipolar Transistor Latch-up,” *IEEE Trans. on Power Elec.*, vol. 27, no. 2, pp. 479-489, Feb. 2012.

D. Brown, M. Abbas, A. Ginart, I. Ali, P. Kalgren, and G. Vachtsevanos. “Turn-off Time as a Precursor for Gate Bipolar Transistor Latch-up Faults in Electric Motor Drives,” *Annual Conference of the Prognostics and Health Management Society*, 2010.

L. Dupont and Y. Avenas, “Preliminary Evaluation of Thermo-Sensitive Electrical Parameters Based on the Forward Voltage for Online Chip Temperature Measurements of IGBT Devices,” *IEEE Trans. on Industry Applications*, vol. 51, no. 6, pp. 4688-4698, Nov.-Dec. 2015.

N. Patil, J. Celaya, D. Das, K. Goebel, and M. Pecht, “Precursor Parameter Identification for Insulated Gate Bipolar Transistor (IGBT) Prognostics,” *IEEE Trans. on Reliability*, vol. 58, DOI: 10.1109/TR.2009. 2020134, no. 2, pp. 271-276, June 2009.

V. Smet, F. Forest, J. J. Huselstein, A. Rashed, and F. Richardeau, “Evaluation of Monitoring as a Real-Time Method to Estimate Aging of Bond Wire-IGBT Modules Stressed by Power Cycling,” *IEEE Trans. on Ind. Elec.*, vol. 60, DOI:10.1109/TIE.2012 .2196894, no. 7, pp. 2760-2770, July 2013.

P. Cova and F. Fantini, “On The Effect of Power Cycling Stress on IGBT Modules,” *Microelectronics Reliability*, vol. 38, no. 6–8, pp. 1347–1352, 1998.

G. Sonnenfeld, K. Goebel, and J. R. Celaya, “An Agile Accelerated Aging, Characterization and Scenario Simulation System for Gate Controlled Power Transistors,” *2008 IEEE AUTOTESTCON*, DOI: 10.1109/ AUTEST.2008.4662613, pp. 208-215, 2008.

J.R. Celaya, P. Wysocki, V. Vashchenko, S. Saha, and K. Goebel. “Accelerated Aging System for Prognostics of Power Semiconductor Devices,” *IEEE AUTOTESTCON.*, 2010.

Z. Wang, B. Tian, W. Qiao, and L. Qu, “Real-Time Aging Monitoring for IGBT Modules Using Case Temperature,” *IEEE Trans. on Ind. Elec.*, vol. 63, pp. 1168-1178, Feb. 2016

M. A. Eleffendi and C. M. Johnson, “Application of Kalman Filter to Estimate Junction Temperature in IGBT Power Modules,” *IEEE Trans. on Power Elec.*, vol. 31, no. 2, pp. 1576-1587, Feb. 2016.

J. R. Celaya, A. Saxena, S. Saha, V. Vashchenko, and K. Goebel, “Prognostics of Power MOSFET,” *2011 IEEE 23rd International Symposium on Power Semiconductor Devices and ICs*, pp. 160-163, 2011.

N.Patil, D. Das, and M.Pecht, “A Prognostic Approach for Non-Punch Through and Field Stop IGBTs,” *Microelectronics Reliability*, vol. 52, issue 3, Pages 482-488, March 2012.

S. Hong, Z. Zhou, C. Lv, and H. Guo, “Prognosis for Insulated Gate Bipolar Transistor Based On Gaussian Process Regression,” *2013 IEEE Conference on Prognostics and Health Management (PHM)*, pp. 1-5, 2013.

A. Alghassi, S. Perinpanayagam, and M. Samie, "Stochastic RUL Calculation Enhanced With TDNN-Based IGBT Failure Modeling," *IEEE Trans. on Reliability*, vol. 65, no. 2, pp. 558-573, June 2016.

Y. Qian and R. Yan, "Remaining Useful Life Prediction of Rolling Bearings Using an Enhanced Particle Filter," *IEEE Trans. on Instru. and Measur.*, vol. 64, no. 10, pp. 2696-2707, Oct. 2015.

M. S. Arulampalam, S. Maskell, N. Gordon, and T. Clapp, "A Tutorial on Particle Filters For Online Nonlinear/Non-Gaussian Bayesian Tracking," *IEEE Trans. on Signal Processing*, vol. 50, no. 2, pp. 174-188, Feb. 2002.

M. Pitt and N. Shephard, "Filtering via Simulation: Auxiliary Particle Filters," *Jour. Amer. Statist. Assoc.*, vol. 94, no. 446, pp. 590–599, 1999.

M. S. Haque, J. Baek, J. Herbert, and S. Choi, "Prognosis of Wire Bond Lift-Off Fault of An IGBT Based On Multisensory Approach," *IEEE Applied Power Electronics Conference and Exposition*, pp. 3004-3011, 2016.

D. Liu, Y. Luo, Y. Peng, X. Peng, and M. Pecht, "Lithium-Ion Battery Remaining Useful Life Estimation Based on Nonlinear AR Model Combined With Degradation Feature," *Proc. Annu. Conf. Prognost. Health Management Soc.*, vol. 3, 2012.

M. E. Orchard and G. J. Vachtsevanos, "A Particle-Filtering Approach for On-Line Fault Diagnosis and Failure Prognosis," *Trans. Inst. Meas. Control*, vol. 31, no. 3–4, pp. 221-246, 2009.

G. Rigatos, "Particle Filtering for State Estimation In Nonlinear Industrial Systems," *IEEE Trans. Inst. Meas.*, vol. 58, no. 11, pp. 3885-3900, Nov. 2009.

M.A.Hossain, Y. Xu, T.J. Peshek, L. Ji, A.R. Abramson, and R. H. French, "Microinverter Thermal Performance in the Real-World: Measurements and Modeling," *PLOS ONE 10,* vol. 7.July 2015.

B. Ristic, S. Arulampalam, and N. J. Gordon, "Beyond the Kalman Filter: Particle Filters for Tracking Applications," *Artech House Publishers*, Norwood, MA, 2004.

G. S. Walia and R. Kapoor, "Particle Filter Based on Cuckoo Search for Non-Linear State Estimation," *3rd IEEE International Advance Computing Conference*, pp. 918-924.

G. S. Walia and R. Kapoor, "Intelligent Video Target Tracking Using An Evolutionary Particle Filter Based Upon Improved Cuckoo Search," *Expert Systems with Applications*, vol. 41, Issue. 14, pp. 6315-6326, Oct. 2014.

G. Meneghesso, G. Verzellesi, A. Tazzoli, M. Meneghini, and E.Zanoni "Reliability of GaN high-electron-mobility transistors: State of the art and perspectives," *IEEE Trans. Device Mater. Rel.*, vol. 8, no. 2, pp. 332–343, Jun. 2008.

M. Meneghini, I. Rossetto, C. Santi, F. Rampazzo, A. Tajalli, A. Barbato, M. Ruzzarin, M. Borga, E. Canato, and E. Zanoni "Reliability and failure analysis in power GaN-HEMTs: An overview," *2017 IEEE International Reliability Physics Symposium (IRPS)*, Monterey, CA, pp. 3B-2.1-3B-2.8, 2017.

S. Yang, D. Xiang, A. Bryant, P. Mawby, L. Ran, and P. Tavner, "Condition Monitoring for Device Reliability in Power Electronic Converters: A Review," *IEEE Trans on Power Electron.*, vol. 25, no. 11, pp. 2734-2752, Nov. 2010.

S. Vitanov V. Palankovski, S. Maroldt, R. Quay, S. Murad, T. Rodle, and S. Selberherr "Physics-Based Modeling of GaN HEMTs," *IEEE Transactions on Electron Devices*, vol. 59, no. 3, pp. 685-693, March 2012.

I. Rossetto, M. Menehghini, O. Hilt, E. Bahat-Treidel, C. Santi, S. Dalcanale, J. Wuerfl, E. Zanoni, and G. Meneghesso "Time-Dependent Failure of GaN-on-Si Power HEMTs With p-GaN Gate," *IEEE Transactions on Electron Devices*, vol. 63, no. 6, pp. 2334-2339, June 2016.

M. Meneghini, D. Bisi, S. Stoffels, M. Van Hove, T. Wu, S. Decoutere, G. Meneghesso, and E. Zanoni., "Trapping and Reliability Assessment in D-Mode GaN-Based MIS-HEMTs for Power Applications," *IEEE Transactions on Power Electronics*, vol. 29, no. 5, pp. 2199-2207, May 2014.

W. Saito, T. Nitta, Y. Kakiuchi, Y. Saito, K. Tsuda, I. Omura, and M. Yamaguchi "On-Resistance Modulation of High Voltage GaN HEMT on Sapphire Substrate Under High Applied Voltage," *IEEE Electron Device Letters*, vol. 28, no. 8, pp. 676-678, Aug. 2007.

N. Badawi, O. Hilt, E. Behat-Treidel, J. Böcker, J. Würfl, and S. Dieckerhoff, "Investigation of The Dynamic On-State Resistance of 600V Normally-Off And Normally-On GaN HEMTs," *IEEE Energy Conversion Congress and Exposition*, pp. 913-919, 2015.

A. K. Sahoo, N. K. Subramani, J. C. Nallatamby, N. Rolland, R. Quere, and F. Medjdoub, "Temperature-dependent Contact and Channel Sheet Resistance Extraction of GaN HEMT," *Integrated Nonlinear Microwave and Millimeter-wave Circuits Workshop*, Taormina, pp. 1-3, 2015.

M. A. Eleffendi and C. M. Johnson, "Application of Kalman filter to estimate junction temperature in IGBT power modules," *IEEE Trans. Power Electron.*, vol. 31, no. 2, pp. 1576-1587, Feb. 2016.

M. S. Arulampalam, S. Maskell, N. Gordon, and T. Clapp, "A Tutorial on Particle Filters For Online Nonlinear/Non-Gaussian Bayesian Tracking," *IEEE Trans. Signal Process.*, vol. 50, no. 2, pp. 174-188, Feb. 2002.

M. Pitt and N. Shephard, "Filtering via simulation: Auxiliary particle filters," *J. Amer. Statist. Assoc.*, vol. 94, no. 446, pp. 590-599, 1999.

B. Saha, J. R. Celaya, P. F. Wysocki, and K. F. Goebel, "Towards prognostics for electronics components," Proc. *IEEE Aerosp. Conf.*, pp. 1-7, 2009.

K. Goebel, B. Saha, and A. Saxena, "A comparison of three data-driven techniques for prognostics," *Proc. 62nd Meeting Soc. Mach. Failure Prevention Technol.*, vol. 2008, pp. 119-131, May 2008.

Y. Qian and R. Yan, "Remaining useful life prediction of rolling bearings using an enhanced particle filter," *IEEE Trans. Instrum. Meas.*, vol. 64, no. 10, pp. 2696-2707, Oct. 2015.

T. Sreenuch, A. Alghassi, S. Perinpanayagam, and Y. Xie, "Probabilistic Monte-Carlo method for modeling and prediction of electronics component life," *Int. J. Adv. Comput. Sci. Appl.*, vol. 5, no. 1, pp. 96-104, 2014.

X. Si, W. Wang, C. Hu, and D. Zhou, "Remaining Useful Life Estimation—A Review on The Statistical Data-Driven Approaches," *Eur. J. Oper. Res.*, vol. 213, no. 1, pp. 1-14, 2011.

M. S. Haque, S. Choi, and J. Baek, "Auxiliary Particle Filtering-Based Estimation of Remaining Useful Life of IGBT," in *IEEE Transactions on Industrial Electronics*, vol. 65, no. 3, pp. 2693-2703, March 2018.

D. Jin and J. A. del Alamo, "Methodology for the Study of Dynamic ON-Resistance in High-Voltage GaN Field-Effect Transistors," *IEEE Transactions on Electron Devices*, vol. 60, no. 10, pp. 3190-3196, Oct. 2013.

A. Lidow, J. Strydom, M. de Rooij, and D. Reusch, "GaN Transistors for Efficient Power Conversion," *2nd Edition, John Wiley, and Sons*, 2015.

O. Hilt, E. Bahat-Tridel, E. Cho, S. Singwald, and J. Wurfl, "Impact of Buffer Composition on the Dynamic On-State Resistance of High-Voltage AlGaN/GaN HFETs," *International Symposium on Power Semiconductor Devices and ICs*, p. 345, 2012.

S. R. Bahl and M. D. Seeman, "New Electrical Overstress and Energy Loss Mechanisms in GaN Cascodes," *Applied Power Electronics Conference* (APEC), session T25, 2015.

S. R. Bahl, J. Joh, L. Fu, A. Sasikumar, T. Chatterjee, and S. Pendharkar, "Application reliability validation of GaN power devices," *2016 IEEE International Electron Devices Meeting* (*IEDM*), San Francisco, CA, pp. 20.5.1-20.5.4, 2016.

J. Würfl, O. Hilt, E. Bahat-Tridel, R. Zhytnytska, P. Kotara, F. Brunner, O.Krueger, and M.Weyers "Techniques towards GaN power transistors with improved high voltage dynamic switching properties," *2013 IEEE International Electron Devices Meeting*, Washington, DC, pp. 6.1.1-6.1.4, 2013.

Guangyu Zhu, Dawei Liang, Yang Liu, Qingming Huang, and Wen Gao, "Improving particle filter with support vector regression for efficient visual tracking," *IEEE International Conference on Image Processing* 2005, Genova, pp. II-422, 2005.

N. Kabaoglu, “Target Tracking Using Particle Filters With Support Vector Regression,” in *IEEE Transactions on Vehicular Technology*, vol. 58, no. 5, pp. 2569-2573, Jun 2009.

R. Ripley “Pattern Recognition and Neural Networks,” Cambridge Univ. Press, Cambridge, 1996.

A. Hoerl and R. Kennard, “Ridge Regression: Biased Estimation for Nonorthogonal Problems,” Technometrics 12, 55–67,1970.

L. Wang, L. Bo, and L. Jiao, “Sparse Kernel Ridge Regression Using Backward Deletion,” PRICAI, 2006.

J. Lutz, H. Schlangenotto, U. Scheuermann, R. De Donker, “Semiconductor Power Devices: Physics, Characteristics, Reliability,” Springer Verlag, 2011.

M. Held, P. Jacob, G. Nicoletti, P. Scacco, and M.H. Poech, “Fast power cycling test of IGBT modules in traction application,” in *Proc. International Conference on Power Electronics and Drive Systems*, pp. 1–6, 1997.

R. Bayerer, T: Herrmann, T. Licht, J. Lutz, and M. Feller, “Model for Power Cycling lifetime of IGBT Modules – various factor influencing lifetime,” in *International Conference on Integrated Power Systems* (CIPS), pp. 1–6, 2008.

X. Wang, A. Castellazzi and P. Zanchetta, “Temperature control for reduced thermal cycling of power devices,” in *European Conference on Power Electronics and Applications* (EPE), pp. 1–10, 2013.

D. A. Murdock, J. E. R. Torres, J. J. Connors, and R. D. Lorenz, “Active Thermal Control of Power Electronic Modules,” *IEEE Transactions on Industry Applications*, vol. 42, no. 2, pp. 552-558, Mar.-Apr. 2006.

J. Lemmens, P. Vanassche and J. Driesen “Optimal Control of Traction Motor Drives Under Electrothermal Constraints,” *IEEE Journal of Emerging and Selected Topics in Power Electronics*, vol. 2, no. 2, pp. 249-263, Jan. 2014.

M. Andresen, K. Ma, G. Buticchi, J. Falck, F. Blaabjerg and M. Liserre, “Junction Temperature Control for More Reliable Power Electronics,” in *IEEE Transactions on Power Electronics*, vol. 33, no. 1, pp. 765-776, Jan. 2018.

M. Weckert and J. Roth-Stielow “Lifetime as a Control Variable in Power Electronic Systems,” in *E-mobility – Electrical Power Train*, pp.1–6, 2010.

M. S. Haque and S. Choi, “Support Vector Regression Assisted Auxiliary Particle Filter based Remaining Useful Life Estimation of GaN FET,” *IECON 2018 - 44th Annual Conference of the IEEE Industrial Electronics Society*, pp. 1525-1530, 2018.

F. Wu, F. Feng, and H. B. Gooi, “Cooperative Triple-Phase-Shift Control for Isolated DAB DC-DC Converter to Improve Current Characteristics,” *IEEE Transactions on Industrial Electronics*, vol. 66, no. 9, pp. 7022-7031, Sept. 2019.

E. Ugur, S. Dusmez and B. Akin, “An Investigation on Diagnosis-Based Power Switch Lifetime Extension Strategies for Three-Phase Inverters,” in *IEEE Transactions on Industry Applications*, vol. 55, no. 2, pp. 2064-2075, March-April 2019.

C. Xu, E. Ugur, F. Yang, S. Pu and B. Akin, “Investigation of Performance Degradation in Enhancement-Mode GaN HEMTs under Accelerated Aging,” *2018 IEEE 6th Workshop on Wide Bandgap Power Devices and Applications* (*WiPDA*), Atlanta, GA, pp. 98-102, 2018.

A. Marquez, J. I. Leon, S. Vazquez, L. G. Franquelo, G. Buticchi, and M. Liserre, “Power Device Lifetime Extension of Dc-Dc Interleaved Converters via Power Routing,” *IECON 2018 - 44th Annual Conference of the IEEE Industrial Electronics Society*, Washington, DC, pp. 5332-5337,2018.

M. Haque and S. Choi, “Sparse Kernel Ridge Regression Assisted Particle Filter based Remaining Useful Life Estimation of Cascode GaN FET,” in *IEEE Transactions on Industrial Electronics*, June 2020.

X. Huang, Q. Li, Z. Liu, and F. C. Lee, “Analytical Loss Model of High Voltage GaN HEMT in Cascode Configuration,” in *IEEE Transactions on Power Electronics*, vol. 29, no. 5, pp. 2208-2219, May 2014.

X. Huang, Z. Liu, F. C. Lee, and Q. Li, “Characterization and Enhancement of High-Voltage Cascode GaN Devices,” in *IEEE Transactions on Electron Devices*, vol. 62, no. 2, pp. 270-277, Feb. 2015.

Q. Li, B. Liu, S. Duan, L. Wang, B. Xu, and C. Luo, “Analytical Switching Loss Model of Cascode GaN HEMTs Based Totem-Pole PFC Converters Considering Stray Inductances,” *2018 1st Workshop on Wide Bandgap Power Devices and Applications in Asia*, Xi’an, China, pp. 118-124, 2018.

L. C. Murillo Carrasco and A. J. Forsyth, “Energy Analysis and Performance Evaluation of GaN Cascode Switches in An Inverter Leg Configuration,” *2015 IEEE Applied Power Electronics Conference and Exposition* (APEC), Charlotte, NC, pp. 2424-2431,2015.

Y. Xin et al., “Analytical Switching Loss Model for GaN-Based Control Switch and Synchronous Rectifier in Low-Voltage Buck Converters,” in *IEEE Journal of Emerging and Selected Topics in Power Electronics*, vol. 7, no. 3, pp. 1485-1495, Sept. 2019.

J. Gareau, R. Hou and A. Emadi, “Review of Loss Distribution, Analysis, and Measurement Techniques for GaN HEMTs,” in *IEEE Transactions on Power Electronics*, vol. 35, no. 7, pp. 7405-7418, July 2020.